FACULTÉ DES ÉTUDES SUPÉRIEURES ET POSTOCTORALES

uOttawa

L'Université canadienne
Canada's university

FACULTY OF GRADUATE AND POSDOCTORAL STUDIES

Eric Lanteigne
AUTEUR DE LA THÈSE / AUTHOR OF THESIS

M.A.Sc. (Mechanical Engineering)
GRADE / DEGREE

Department of Mechanical Engineering
FACULTÉ, ÉCOLE, DÉPARTEMENT / FACULTY, SCHOOL, DEPARTMENT

Design of a Composite SMA Actuator for a Pressurized Hyper-redundant Manipulator

TITRE DE LA THÈSE / TITLE OF THESIS

Dr. A. Jnifene
DIRECTEUR (DIRECTRICE) DE LA THÈSE / THESIS SUPERVISOR

CO-DIRECTEUR (CO-DIRECTRICE) DE LA THÈSE / THESIS CO-SUPERVISOR

EXAMINATEURS (EXAMINATRICES) DE LA THÈSE / THESIS EXAMINERS

Dr. M. Munro

Dr. Robert Langlois

Gary W. Slater
Le Doyen de la Faculté des études supérieures et postdoctorales / Dean of the Faculty of Graduate and Postdoctoral Studies

Design of a Composite SMA Actuator for a Pressurized Hyper-redundant Manipulator

by

Eric Lanteigne

A thesis submitted to the Faculty of Graduate and Postdoctoral Studies in partial fulfillment of the requirements for the degree of

MASTER OF APPLIED SCIENCE

In Mechanical Engineering

Ottawa-Carleton Institute for Mechanical and Aerospace Engineering
University of Ottawa

Library and
Archives Canada

Published Heritage
Branch

395 Wellington Street
Ottawa ON K1A 0N4
Canada

Bibliothèque et
Archives Canada

Direction du
Patrimoine de l'édition

395, rue Wellington
Ottawa ON K1A 0N4
Canada

Your file Votre référence
ISBN: 978-0-494-25796-8
Our file Notre référence
ISBN: 978-0-494-25796-8

NOTICE:
The author has granted a non-exclusive license allowing Library and Archives Canada to reproduce, publish, archive, preserve, conserve, communicate to the public by telecommunication or on the Internet, loan, distribute and sell theses worldwide, for commercial or non-commercial purposes, in microform, paper, electronic and/or any other formats.

The author retains copyright ownership and moral rights in this thesis. Neither the thesis nor substantial extracts from it may be printed or otherwise reproduced without the author's permission.

AVIS:
L'auteur a accordé une licence non exclusive permettant à la Bibliothèque et Archives Canada de reproduire, publier, archiver, sauvegarder, conserver, transmettre au public par télécommunication ou par l'Internet, prêter, distribuer et vendre des thèses partout dans le monde, à des fins commerciales ou autres, sur support microforme, papier, électronique et/ou autres formats.

L'auteur conserve la propriété du droit d'auteur et des droits moraux qui protège cette thèse. Ni la thèse ni des extraits substantiels de celle-ci ne doivent être imprimés ou autrement reproduits sans son autorisation.

In compliance with the Canadian Privacy Act some supporting forms may have been removed from this thesis.

While these forms may be included in the document page count, their removal does not represent any loss of content from the thesis.

Conformément à la loi canadienne sur la protection de la vie privée, quelques formulaires secondaires ont été enlevés de cette thèse.

Bien que ces formulaires aient inclus dans la pagination, il n'y aura aucun contenu manquant.

Canada

Abstract

Hyper-redundant devices are characterized by repeating independently controlled structures connected in series, much like the architecture of a snake or worm. This thesis evaluates the performance of a pressurized hyper-redundant manipulator design driven by high strain shape memory alloy actuators. The proposed design is composed of four identical modules; each providing three degrees of freedom from three symmetrically positioned actuators. The modules have an outer diameter of 31mm and a length of 33mm at full extension. The actuator return force and manipulator stiffness are controlled by an air pump connected at the base. Although connection failures between the actuator tabs and vertebrae prevented the validation of the hyper-redundant manipulator prototype, the unit module element was successfully fabricated and evaluated. The unit module could achieve linear contractions of 40% and rotations of over 50° at a frequency of 0.05Hz. Several limitations remain to be addressed in order to build a reliable device; these include: 1) The high current requirement of the actuators, 2) The inefficient actuation system, and 3) The connectivity issues between the actuators and the modules.

Contents

List of Tables

List of Figures

Acknowledgements

I would first and foremost like to thank my thesis supervisor, Dr. Amor Jnifene, for his unconditional support throughout this project. The prototype construction would not have been possible without the help of senior technical officer John Perrins as well as Leo Denner for the precious "on the spot" technical advice. I would also like to thank Dr. Francois Robitaille, who provided the 10N load cell used in the actuator tensile testing and vacuum pump used in the fabrication of the rubber bellows as well as Mr. Daniel Séguin for providing the sheet metal used in the heat-treatment jig.

Chapter 1: Introduction

Hyper-redundant devices are generally defined as repeating independently controlled structures. In biological terms, their architecture is comparable to that of a snake or worm. The analysis of the crawling motion of these biological beings was the prime motivator in the early development of redundant robotic systems [18]. Early prototypes included snake-like servo-powered robots capable of producing a wave motion to bring about a displacement. However, it was the redundant capabilities of the design that prompted the development of one of the first industrial redundant manipulators, the Toshiba water turbine inspector, in the mid-eighties [18]. It was found that the repeating structure of the robot could adapt its shape to highly complex configurations. This key ability allowed the manipulator to reach targets previously unattainable by conventional robotic devices.

The industry-approved design lead to the research and development of many different types of redundant manipulators. By the end of the century, smart materials would begin to replace conventional electromagnetic and hydraulic actuators [8]. In recent years, significant efforts have been made by the robotics research community to simplify, miniaturize and improve the performance of redundant manipulators. This has lead to the concept of discrete actuation [12]. The principle is founded on the basis that the actuators have only two states: *ON* or *OFF,* and that each state has a single position. This reduces the manipulator's workspace to a set of discrete points but has the advantage of greatly simplifying the hardware. Discrete changes in the actuator state enables the manipulator to operate without the use of sensing equipment and feedback control, and as the hyper-redundancy of the manipulator increases, its performance reaches that of a continuous robot [11].

1.1 MOTIVATION FOR RESEARCH INTO HIGH DOF DEVICES

Studies have shown that many downfalls such as less than accurate positioning, bulky and complex structures and complicated control software are associated with hyper-redundant devices [44]. However, advancements in electronics, smart materials and manufacturing methods as well as a growing demand for manipulation unsuitable to rigid-link robots has led to increased research of the biologically inspired machine.

The goal of this research is to develop a miniature compliant hyper-redundant manipulator, which addresses mechanical limitations of traditional miniature devices. Two major issues involved in the design of such a system include: 1) The design of flexible low-weight unit module (attached in series, they constitute the structure of the manipulator), and 2) The design of a high strain actuator capable of producing large displacements within the unit module.

1.2 THESIS STRUCTURE AND CONTENT

The following chapters describe the design process leading to the fabrication of the prototype manipulator. Figure 1-1 shows the structure of the thesis and the flow of information between the chapters. The design process begins with a review of existing manipulator designs and actuation methods in Chapter 2.

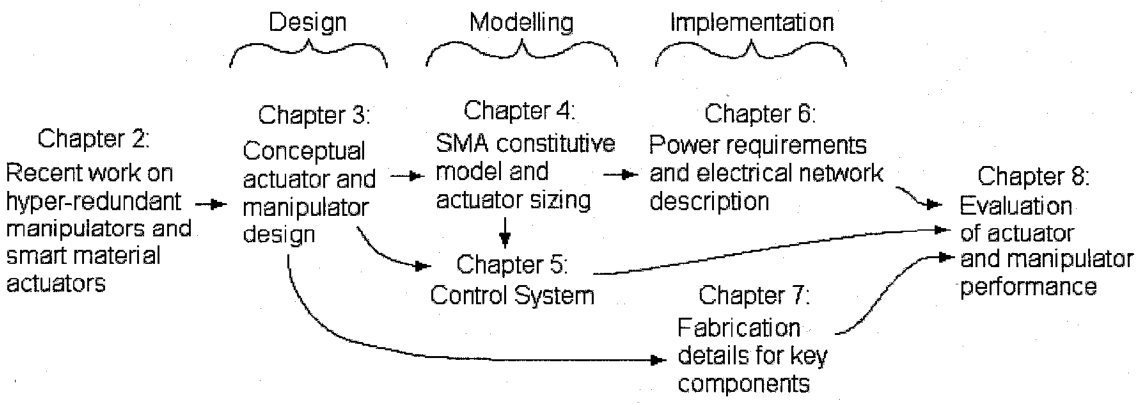

Figure 1-1: Thesis structure

Chapter 3 presents the conceptual design of the actuator and manipulator structure. Although they are presented separately in two sections, both concepts are interdependent. Each section contains a detailed description of the proposed designs as well as a preliminary analysis to determine their compatibility.

Chapter 4 provides the detailed analysis of the modeling of the actuator's mechanical characteristics based on a two-phase constitutive model developed by X. Peng [37]. The actuator dimensions are determined using an exhaustive search based on the force-displacement outputs produced by the model.

Chapter 5 gives an overview of the control system including an analysis of the forward and inverse kinematics as well as the manipulator controller. The control algorithm is based on the principle of binary actuation and uses an iterative process to account for the structure's weight. The manipulator workspace is computed for all possible configurations stored in memory.

Chapter 6 describes the electrical network powering the SMA actuators. The actuators are arranged in a matrix-like network in which both lead and ground connections are controlled by electrical switches [33]. A description of the network as well as an analysis of the hardware is provided in this chapter.

Chapter 7 presents the details on the manufacturing process used to produce the key components of the manipulator structure. It describes the heat treatment process used to transform the SMA sheet and the moulding process used to form the manipulator's outer shell. The chapter also illustrates the prototype assembly process and discusses several fabrication issues.

Chapter 8 gives the detailed results of the SMA material tests, frequency response tests, and actuator tensile tests. This is followed by an analysis and discussion of the actuator and manipulator performance.

Chapter 9 then summarizes the results, discusses several limitations and suggests some areas for further work.

Chapter 2: Literature Review

2.1 RECENT WORK ON HYPER-REDUNDANT MANIPULATORS

In the last three decades, significant improvements in material and manufacturing technologies have lead to a wide range of innovative hyper-redundant designs and a1 steady trend towards miniaturization. Early experiments on redundant manipulators were performed on continuous manipulators. These devices have all their components fixed to a single non-extendable backbone. The structures are divided into sections and each section is controlled via motor-driven cables. It was found that the interaction between the active and conduit cables in the base section reduced the bending capabilities and that higher cable tensions were required to maintain sufficient structural stiffness as the length to width ratio increased [16]. However, these devices could only operate effectively in the downward vertical position or in low gravity environments. An example of such a design is shown in Figure 2-1.

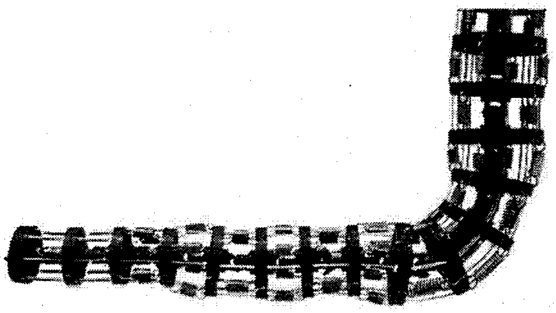

Figure 2-1: Trunk-like continuum manipulators [48]

These devices featured a much larger number of degrees of freedom (DOF) and could configure their structure to meet a wide variety of shapes. The discovery of NiTi shape memory alloys in 1962 prompted the development of muscle type actuators [18]. Increased configurability and dexterity could be achieved by replacing the cable-driven actuators and base control platform with directly driven SMAs. Again, it was found that the actuators had difficulties controlling the accumulated weight of each section and that the manipulator could not operate in the upright position [48]. In the same period, a pneumatic hyper-redundant manipulator with a variable geometry truss structure was developed at the Johns Hopkins University [7]. Results have shown that this device had a higher strength to weight ratio and greater manoeuvrability than the SMA actuated or cable driven trunk manipulators [7].

By the end of the 20th century, miniature hyper-redundant manipulators driven by SMAs were entering the biomedical field. The example shown in Figure 2-2 is a three joint sensor-less manipulator driven by nine SMA wire actuators. Each actuator is controlled independently via a built-in integrated circuit located in each link. This method reduces the number of wires in the manipulator to three: current source, ground and control voltage.

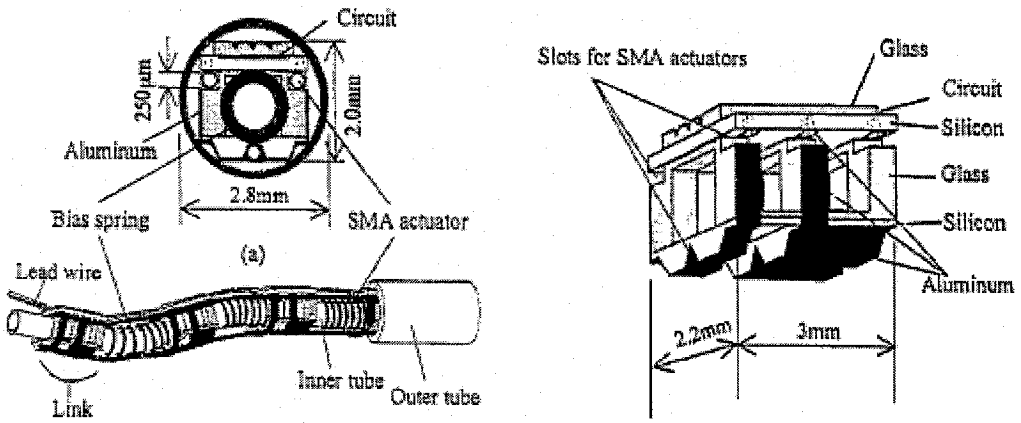

Figure 2-2: Active hyper-redundant endoscope [28]

Without a protective outer shell, each joint could achieve a bending angle of about 47° with a complete SMA transformation cycle of about 1.8 seconds [28]. The endoscopic actuator shown in Figure 2-3 is composed of parallel single DOF joints, actuated by two antagonistic SMA strips. Each 6mm diameter joint could achieve a stroke of ±15° without a protective shell [36].

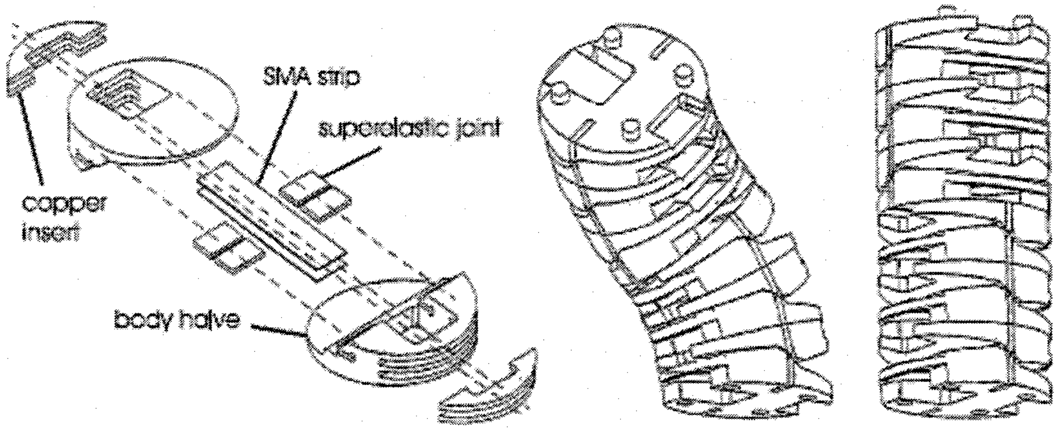

Figure 2-3: Endoscopic actuator [35]

It was also found that the compact design and insulating material protecting the SMA strips resulted in non-uniform cooling and low heat dissipation. From Figure 2-3 it is also clear that a large number of joints would lead to wiring issues. Shown in Figure 2-4 is a similar endoscopic tool developed by the Laboratoire de Robotique de Paris [44].

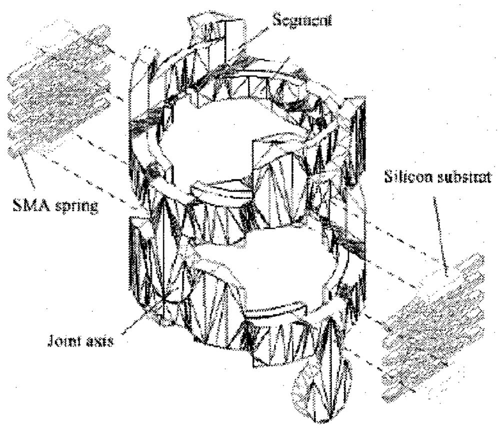

Figure 2-4: One DOF joint of a tubular endoscopic manipulator [44]

As opposed to the previous design, the actuators are located on the periphery of the structure. This architecture provides room for the various wires and cables and increases the heat dissipation capabilities of the actuator. Preliminary tests on a bare section of the manipulator demonstrated that the joint could achieve a stroke of ±15° [44]. Studies have also shown that the effects of an outer shell become more pronounced as the manipulator is miniaturized. As an example, the micromanipulator designed by T. Mineta has a 50° stroke without the outer tube and a 35° stroke with the outer shell [30].

On the macroscopic scale, recent hyper-redundant manipulators focus on applications in self-transforming robots and camera placement and light positioning in the biomedical field [11]. Figure 2-5 illustrates three experimental binary hyper-redundant manipulators developed at the MIT robotics laboratory. The three designs are based on the assembly of modular parallel platforms controlled by three actuators.

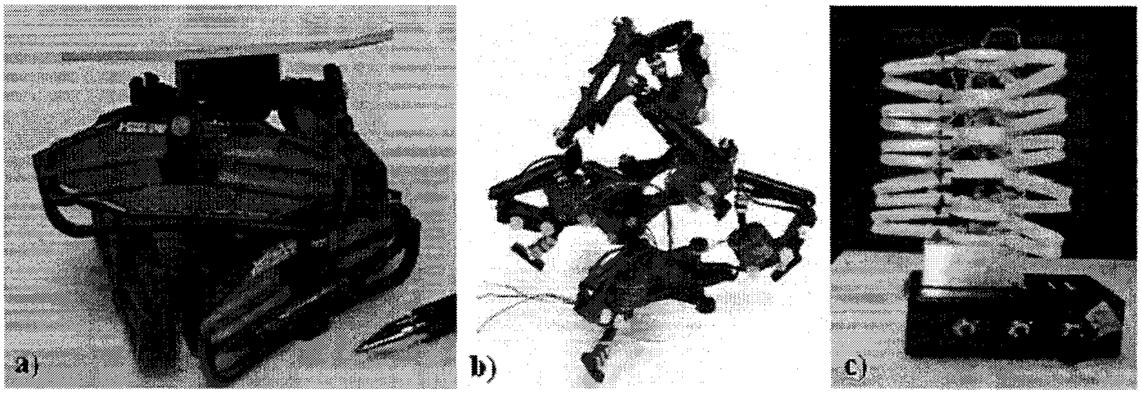

Figure 2-5: BRAID binary hyper-redundant manipulators: a) dielectric polymer actuators [11], b) magnet-coil actuators [17], and c) antagonistic SMA actuators [12]

The manipulators of Figure 2-5 a) and b) are equipped with discrete mechanisms which lock the actuators in fixed states. The bistability is achieved using the snap motion of buckling beams; this mechanism gives the device high repeatability, accuracy and maintains the desired configuration in the presence of disturbances [17]. All the manipulators are fabricated from lightweight and fatigue resistant material and are able to support moderate payloads. However, compared to the active catheters of Figures 2-3 and 2-4, the BRAID manipulators were not designed to accommodate a protective outer sheath and the numerous components and linkages are exposed to environmental factors.

2.2 ACTUATORS FOR MINIATURE MANIPULATORS

2.2.1 Summary of Actuation Methods

Robotic devices use many different types of actuators according to the required stroke, force, weight, dimensions, work capacity, frequency and efficiency. Moreover, the characteristics of a single actuator type or family can also differ depending on shape, size, configuration and application [2]. For practical applications, selecting an actuator can be achieved by reviewing actuators in existing designs and current actuation methods. Several studies also exist which numerically compare actuator families. Ashby et al. proposed a detailed analysis that uses normalized characteristics such as strain, stress and density to compare actuator families [1]. The results of one of these comparisons are shown in Figure 2-6. Similar plots can be found in Appendix A.

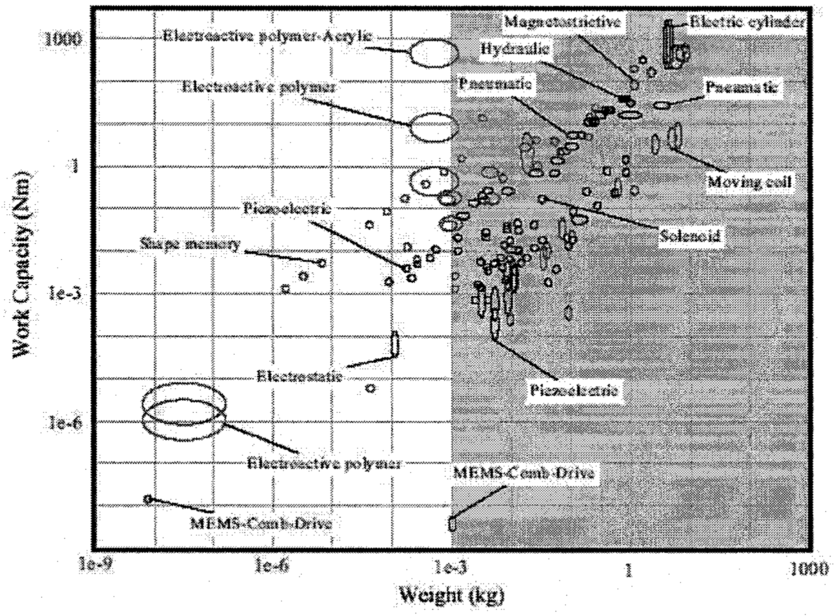

Figure 2-6: Actuator work capacity versus weight (adapted from [1])

In the case of hyper-redundant manipulators, the number of actuators becomes very large and weight becomes one of the most important constraints in the actuator selection. Actuator families located at the left side of Figure 2-6 demonstrate the lowest weight to work ratio. These include all actuators in the smart materials category: piezoelectric, electroactive polymer and shape memory alloy actuators.

Another study by Kornbluh et al. [24] compared the maximum performance of current actuation technologies based on several mechanical properties. As opposed to the previous analysis, the actuator properties are given in tabular form. Again, since each actuator family was evaluated under different conditions, the values listed are approximate.

Table 2-1: Actuator performance comparison (adapted from [24])

Actuator Type	Maximum Strain (%)	Maximum Pressure (MPa)	Specific Elastic Energy Density (J/g)	Maximum Efficiency (%)	Relative Speed (Complete Cycle)
Dielectric Elastomer	380	7.2	3.4	60-80	Medium/Fast
Electrostrictive Elastomer	4.3	43	0.49	~80	Fast
Shape Memory Polymer	100	4	2	<10	Slow
Polyelectrolyte Gel	>40	0.3	0.06	30	Slow
Nanotube	>2.5	>1	>0.013	<10?	Medium
Ionic Polymer	10	1.0	0.025	<10	Medium
SMA	>5	>200	>15	<10	Slow
Piezoelectric Crystal	1.7	131	0.13	90	Fast
Piezoelectric Ceramic	0.2	110	0.013	90	Fast
Magnetostrictive	0.2	70	0.0027	60	Fast
Electromagnetic	50	0.10	0.003	>90	Fast
Human Muscle	>40	0.35	0.07	-	Medium

Table 2-1 shows that shape memory alloys and dielectric elastomers have the highest energy densities. SMA actuators can produce the greatest pressure while dielectric elastomers can produce the highest strains. It is to be noted that the use of transformation mechanisms such as rigid links can increase the output force at the expense of strain or vice versa but that this approach may lead to weight problems.

SMAs have the advantage of being formed to the desired shape and used as a stand-alone actuator, requiring only a bias mechanism to return the material to its original shape. Their main disadvantage is that they have a low frequency response due to poor cooling capabilities and a low efficiency due to inefficient heating. However, they exhibit the highest energy density of all the materials and appear to be the most attractive choice in the development of micro-actuators.

2.2.2 SMA Behaviour Background

Shape memory alloys are composed of two phases: martensite and austenite. The change between the two crystalline structures is called the thermoelastic martensitic transformation. The martensite phase behaves ferroelastically due to its self-accommodating nature (can be deformed to very high strains). As the temperature is reduced, martensite plates nucleate in the austenite matrix in such a way to produce no observable strains. Applied stresses induce a reorientation of the martensite's structure (detwinning) resulting in large macroscopic deformations [6]. When the material is heated above the critical temperature, the martensite crystalline structure transforms to austenite resulting in the recovery of the previous induced strain. This second property is called the shape memory effect (SME) and is illustrated in Figure 2-7. If the material is composed primarily of austenite, applied stresses may induce martensitic transformation and the actuator deforms plastically. The material reverts back to the austenite state when the stresses are removed and the plastic strain, resulting from the martensite reorientation is recovered [15]. This third property is referred to as pseudoelasticity (PE). The schematic representation of each crystalline phase is illustrated in Figure 2-8.

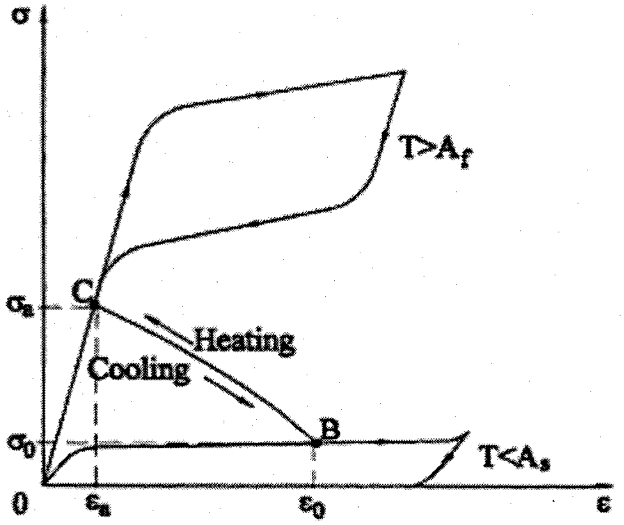

Figure 2-7: Shape memory effect [49]

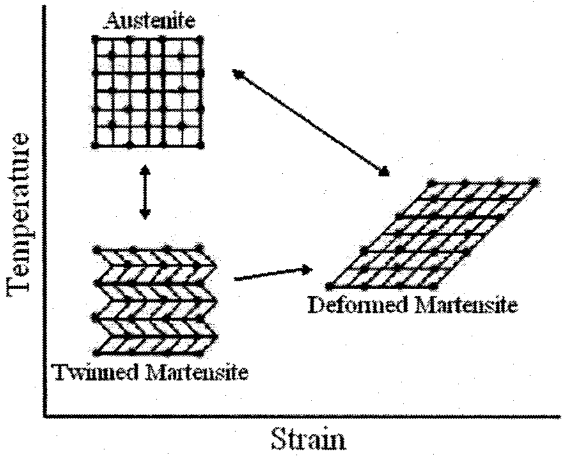

Figure 2-8: SMA crystalline structures [39]

A forth SMA property called the two-way shape memory effect (TWSME) has recently been observed. To obtain TWSME, irreversible defects such as dislocations or precipitates are introduced in the martensite phase. These defects induce internal stress fields, which control the growth of the martensite plates [52]. Experiments have shown that the strain recovery is only in the order of 1% [52]. This property will not be applied to the proposed actuator design

2.2.3 Possible SMA Actuator Configurations

Nitinol (Ti – 55.8% wt. Ni) is the most common type of shape memory alloy used in actuators. It comes in wire, ribbon or sheet format, and can be laser cut, electrochemically etched or sputter deposited [13,15]. Most SMAs have a maximum transformation strain of around 8%. To obtain larger displacements, the material strain orientation could be offset from the actuator strain by reorienting the SMA material or by using linkages to convert force into displacement. Geometrical reorientation of SMA wires is used to increase the total displacement in the actuator proposed by Grant and Harvard. This was accomplished by weaving several SMA wires in a counter-rotating pattern around supporting disks as seen in Figure 2-9 [29].

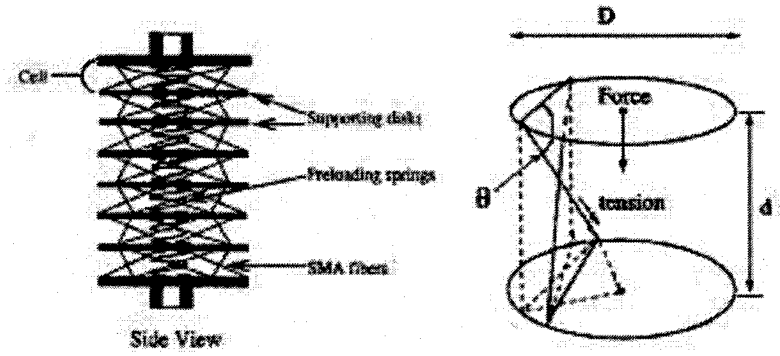

Figure 2-9: High strain SMA actuator [29]

With this configuration, the total actuator displacement is increased by a factor of $1/(\cos\theta)$ with respect to the displacement of the individual SMA fibres. Compared to pneumatic and electromechanical actuators of similar size, the actuator of Figure 2-9 can produce forces up to 400% higher for similar strain [29]. This design is limited to axial motion. Most hyper-redundant manipulators illustrated in the previous section are equipped with SMA bending actuators to produce multiple DOFs. Figure 2-10 is an example of a single DOF actuator activated by an SMA strip operating in bending mode. At the maximum current level, the end-effector of the catheter could achieve a 60° bending angle with a protective outer shell [30].

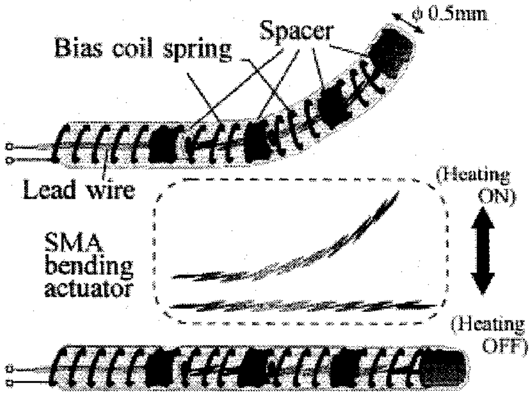

Figure 2-10: Catheter actuated by a SMA meandered beam [30]

Bending actuators were also used in rotary joints. An analysis by K. Kuribayashi compared the strength, ability to memorize original profiles, joint making and downscalablility of different SMA configurations attached to a miniature rotary joint

[25]. Figure 2-11 illustrates the six SMA actuator configurations evaluated: a) torsional spring, b) sinusoidal spring, c) spiral spring, d) meandered flat sheet, e) beam, and f) circular beam. Each actuator was given a qualitative rating between easy and difficult for each characteristic and the results are listed in Table 2-2.

These observations demonstrated that, except for type (d), all actuators exhibited similar strengths but that only the beam elements could be effectively connected to the linkages (due to the large surface area available for bonding). It was determined that the circular beam type actuator was the most apt to be used as an actuator in a miniature rotary joint.

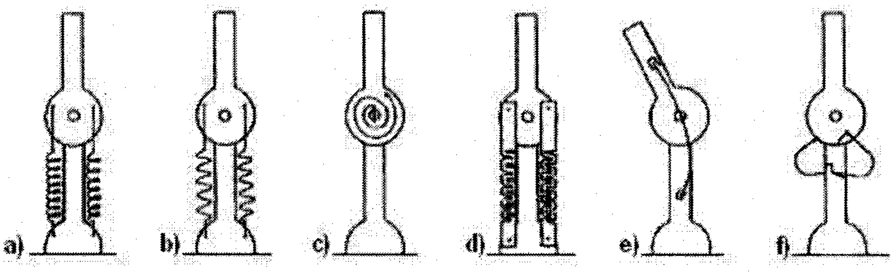

Figure 2-11: Several types of SMA shapes [25]

Table 2-2: Comparison chart [25]

Type	Memorizing Profile	Strength	Setting SMA to link	Down-scalability
a)	□	○	□	□
b)	□	○	□	□
c)	□	○	□	□
d)	○	□	Δ	□
e)	Δ	○	○	Δ
f)	○	○	○	○

○: easy Δ: moderate □: difficult

2.2.4 SMA Actuator Control

Heating SMAs above the austenite finish temperature induces the phase transformation and is most commonly achieved by electrically heating the SMA element. Several methods exist to control the transformation rate and steady-state temperature of the SMA actuator. The simplest approach consists of measuring the temperature increase directly using a temperature sensor such as a thermocouple or thermistor. Another method consists of measuring the electrical resistance of the SMA actuator since the two phases: austenite and martensite have two distinctive resistances [21]. As the temperature is increased the actuator resistivity gradually increases from around 80mΩcm in the martensite state to 100mΩcm in the austenite state (resistivity values supplied by Johnson-Matthey). This method has the advantage of requiring no additional components. The actuator resistance can be computed from the input voltage and current measurements.

SMA actuators exhibit severe hysteresis, which is often responsible for position inaccuracy in a regulation or tracking system and may even cause instability in some cases [42]. The memorizing capability of the SMA material also degrades in time as permanent strains are generated within the martensite matrix [52]. Feedback control, neural networks, pulse-width (PW) and pulse-width pulse-frequency (PWPF) modulation are just some of the control methods used to overcome these challenges [21,41,42]. However, this study is limited to the design and fabrication of the composite SMA actuator. As it will be mentioned in Chapter 5, the actuators are to be discretely controlled, eliminating the need for any feedback control.

Chapter 3:
Proposed Design

3.1 ACTUATOR DESIGN

In the previous section, it was shown that most SMA actuators used in high displacement manipulators operate in bending mode. SMA flexures provide large forces and displacements but require mechanisms such as links to transform the rotational motion into linear motion. SMA spring actuators are capable to producing large displacements but, as mentioned in K. Kuribayashi's experiments, are difficult to fasten in miniature manipulators [25]. High surface area actuators such as beams are easily bonded using temperature resistant epoxy.

3.1.1 Composite SMA Actuator Design

With this in mind the sinusoidal actuator shape (b) and the circular beam shape (f) in Figure 2-11 could be combined to produce linear motion while taking advantage of the large surface area of the beam. The preliminary design for such an actuator is shown in Figure 3-1. SMA actuators have the disadvantage of having low frequency responses but their use is justified by their very high work capacity; however, the actual work capacity of the actuator is often much lower than the maximum rated value due to the geometric configuration of the actuator. The entire straight segment shown in the enlargement of Figure 3-1 has little effect on the actuator's total performance. It simply serves as a link between each circular section to convert the rotary motion into linear motion and generates unnecessary heat during actuation; which reduces the cooling capabilities of the actuator, especially in confined environments.

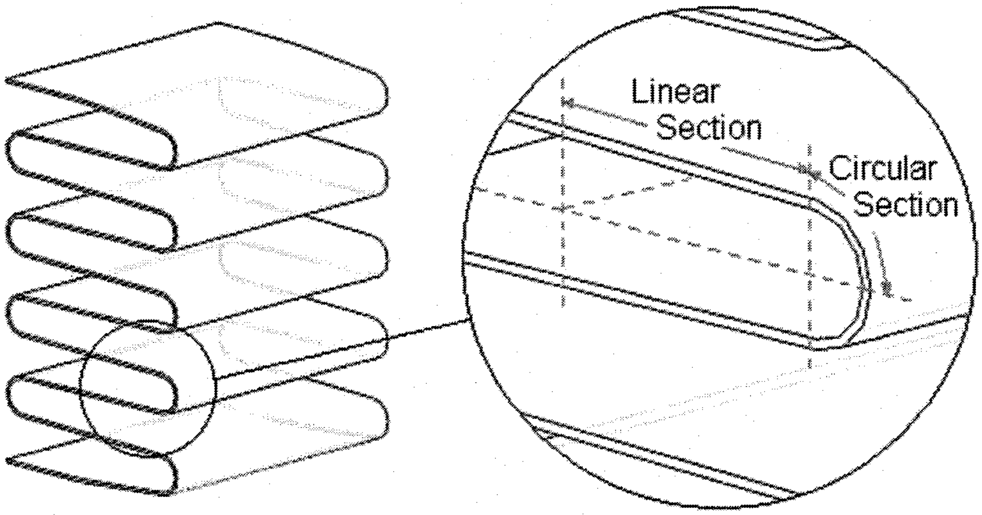

Figure 3-1: Actuator design

A solution to this problem involves the reinforcing of the straight segments of the actuator with small metal panels to reduce bending in that region. The use of conducting epoxy and low resistivity metal panels (or films) lowers the heat generated in that region by reducing its resistance. During the cooling cycle the straight portion may also act as a heat sink, which should improve the frequency response of the actuator (since the frequency response is dominated by the cooling capabilities of the actuator).

A schematic diagram of a section of the proposed composite SMA actuator is shown Figure 3-2 (the dimensions of the epoxy layer and metal film are not to scale).

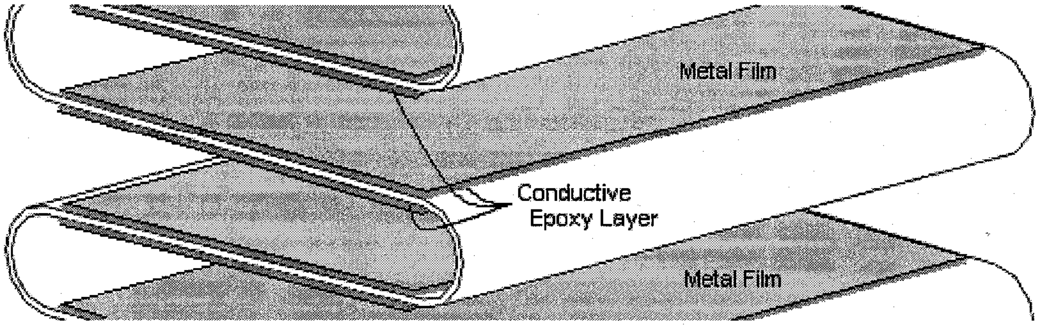

Figure 3-2: Composite SMA actuator

3.1.2 Geometric Constraints

Several geometric relations were needed to obtain the actuator force and displacement curves. From the actuator profile shown in Figure 3-3, the unit section is separated into two parts: a circular segment of length l_C and a straight segment of length l_l.

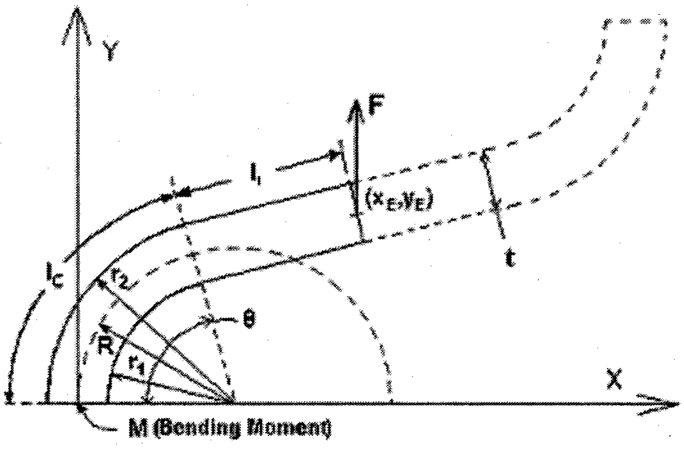

Figure 3-3: Profile of SMA sheet actuator

Assuming the straight segment remains flat throughout the cycle, the following relation can be obtained given both lengths remain constant.

$$\begin{aligned} R_0\theta_0 &= R\theta \\ R\theta &= l_C \end{aligned} \tag{3-1}$$

where R_0 and θ_0 are the initial radius of curvature and angle of the actuator and R and θ are the varying parameters. For circular beams, the neutral axis does not pass through the centroid. The neutral axis, represented by R_{CG}, is located somewhere between the internal radius and the centre of gravity and is given by:

$$R_{CG} = \frac{A}{\int (dA/r)} \tag{3-2}$$

where A is the cross-section area. Solving (3-2) for a rectangular cross-section results in (3-3).

$$R_{CG} = t/\ln(r_2/r_1) \tag{3-3}$$

where t is the thickness of the sheet and r_1 and r_2 are the initial internal and external radii of the bend. Using the equations above, relationships between the endpoint ($x_{E,}$ y_E) of the section and the angle θ can be obtained. Since the length of the circular arc and the straight segment remain constant, x_E and y_E are derived from Figure 3-3.

$$\begin{aligned} x_E &= (R - R\cos\theta) + l_l \sin\theta \\ x_E &= \frac{R_0\theta_0}{\theta}(1-\cos\theta) + (l_l - R_0\theta_0)\sin\theta \\ y_E &= R\sin\theta + l_l\cos\theta \\ y_E &= \frac{R_0\theta_0}{\theta}\sin\theta + (l_l - R_0\theta_0)\cos\theta \end{aligned} \tag{3-4}$$

In the numerical implementation $d\theta$ is the control variable, where:

$$\theta = \theta_0 - d\theta \tag{3-5}$$

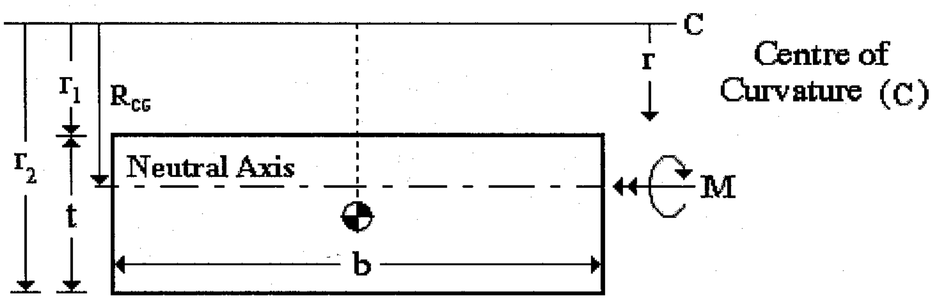

Figure 3-4: Radius of curvature

3.1.3 Approximate SMA Model

Due to the complex elastoplastic properties of the SMAs, the derivation of a complete model is complex and time consuming; therefore, an approximate model was used to obtain initial estimates of the required SMA actuator profile [25]. It will be shown at the end of this chapter that the maximum force required to bend the manipulator is 3.8N.

The maximum variation in the angle θ is constrained such that the strain at the surface of the sheet does not exceed 3%. Studies have shown at this strain level, the SMA material could sustain as much as 10^4 cycles [20,23]. In curved beam bending, the strain varies hyperbolically along the cross section and is given by:

$$\varepsilon(r) = \frac{\Delta\theta}{\theta}\left(\frac{R-r}{r}\right) \tag{3-6}$$

where for simplicity, θ is set to θ_0 and the radius of curvature R is assumed to remain constant as theta changes. Equation (3-6) is only valid for small changes in θ. To determine the stress at each r location of the beam, it is assumed that both austenite and martensite phases contain elastic and plastic components.

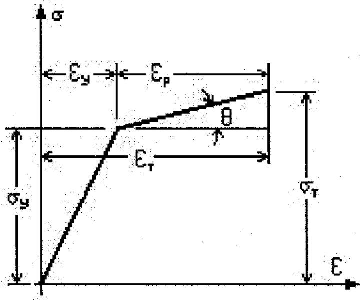

Figure 3-5: Approximate stress-strain response of austenite and martensite [3]

From the stress-strain relationship of Figure 3-5, the relation for the stress in the plastic region is given by:

$$\sigma_{P(A,M)} = \sigma_Y(1 - H/E) + (\varepsilon_T - \varepsilon_y)H \tag{3-7}$$

where H is the equivalent plastic modulus, E is the elastic modulus and ε_T is the total strain. Although the austenite phase exhibits very low pseudoelasticity compared to the martensite phase, the relation below is applicable to both phases since, as the stress is increased, the austenite phase transforms into martensite (assuming the temperature is not well above the austenite finish temperature). Using the strain field obtained from (3-6), the stress *σ(r)* is generated for every unit area of the entire cross-section for both the full austenite and full martensite states. The moment M generated by these stresses is calculated numerically with the following equation, where w is the actuator width:

$$M = w\sum_{r=r1}^{r2}\sigma(r)(R-r)dr \tag{3-8}$$

The moment increases as theta is varied from θ_0 to $\theta_0 + d\theta_{max}$ and the output force is given by:

$$F(\theta) = {M(\theta)}\Big/{x_E(\theta)} \tag{3-9}$$

The austenite and martensite material properties E, H and ε_y were obtained from a study on the one-dimensional behaviour of shape memory alloys [5]. To determine the feasibility of the design, the test case actuator dimensions were selected based on material availability and preliminary design constraints. Both SMA material properties and actuator dimensions are listed in Table 3-1. The output force-displacement plot was obtained by solving (3-4) to (3-9) and the results are shown in Figure 3-6 for both the austenite and martensite states.

Table 3-1: Material and geometric properties

Parameter	**Symbol**	**Units**	**Value**
Martensite elastic modulus	E_M	MPa	67000
Martensite plastic modulus	H_M	MPa	678
Martensite yield strain	$\varepsilon_{y\,M}$	%	0.185
Austenite elastic modulus	E_A	MPa	67190
Austenite plastic modulus	H_A	MPa	900
Austenite yield strain	$\varepsilon_{y\,A}$	%	0.647
Width	w	mm	8
Thickness	t	mm	0.08
Internal radius of bend	r_1	mm	0.4
Initial angle of circular section	θ_0	rad	π/2
Length of unit section	$l\ (= l_l + l_c)$	mm	2.5

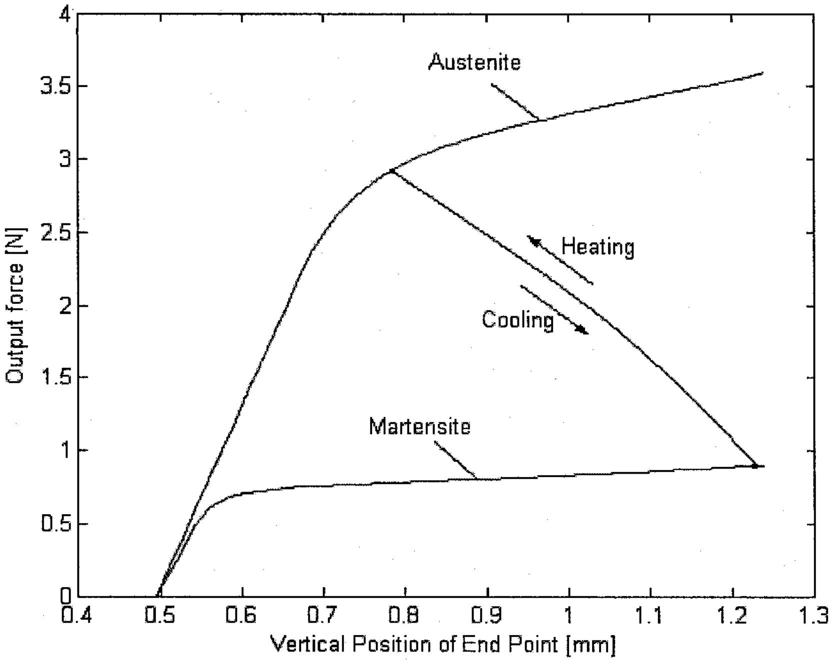

Figure 3-6: Approximate force-displacement of end-effector

The output force generated by the transition of martensite to austenite is close to the target value of 3.8N with deformation strains of over 100% while the size of the SMA sheet remains acceptable. These results justified the application of a constitutive SMA model to the proposed actuator design.

3.2 MANIPULATOR DESIGN

3.2.1 Inherent Problems in Existing Designs

The SMA actuated manipulators described in the review section use either a bias spring or antagonistic actuators to provide the actuator return force. The return force is defined as the force required to extend the actuator to its un-actuated state after actuation (to convert twinned martensite into deformed martensite). Springs provide stiffness to the manipulator structure and in some cases are used as an outer shell to separate the internal components from the working environment. Antagonistic actuators are actuator pairs that provide each other's return force. This arrangement offers the ability to control the structure's stiffness level and eliminates the spring component from the design.

Several complications are inherent to both designs. First, manipulators driven by antagonistic actuators require twice as many actuators and wires. Also, to maintain a relatively constant stiffness, at least one actuator in each link must be maintained in the *ON* state. With the bias spring design, the output force of a bias spring is linear with respect to its displacement; which implies that the actuator must produce a maximum force at the desired final position. Subsequently, the addition of a spring increases the weight of the manipulator, raising issues in hyper-redundant manipulators with a large number of modules.

Moreover, since most of the aforementioned manipulators operate in sensitive, harsh or liquid filled environments, they require a protective outer skin to protect the actuators from the exterior and for delicate operations, or to protect the sensitive environments from the internal components. The protective skin reduces the performance of manipulator by introducing additional constraints and by confining the actuators (reducing the cooling capabilities of the actuators).

3.2.2 Pressurized Hyper-redundant Manipulator Design

The proposed solution combines the outer skin and bias spring into one mechanism. Pressurized air, pumped in at the base of the manipulator, provides the necessary actuator return force and maintains a semi-rigid manipulator structure. Simple calculations have demonstrated that the pressure in a contained four-stage miniature manipulator would increase dramatically if only several SMAs were actuated simultaneously. In addition, the pressure would gradually increase as the air temperature in the structure rises (as a result of heating the actuators). The performance of each subsequent actuator would diminish as a result of the increasing pressure. In order for the high-strain/low-force actuators to function in parallel the pressure should have to remain relatively constant. This could be accomplished in two different ways. First, a relief vessel could be connected to the manipulator to absorb the pressure variations. Changing the volume of the relief vessel could control the internal pressure and the stiffness of the manipulator. The second option would be to pump air in the manipulator and control the airflow at the exit. This solution has the disadvantage of requiring additional components such as valves, tubing and an air compressor, which would increase the overall weight and the power consumption of the system. On the other hand, it would maintain fixed environmental conditions (ensuring repeatability) and would decrease the cooling time of the SMA actuators (ensuring a better frequency response). From a fabrication and controllability point of view, the ventilated system appears to be the better solution. With this in mind, the conceptual design shown in Figure 3-7 was proposed.

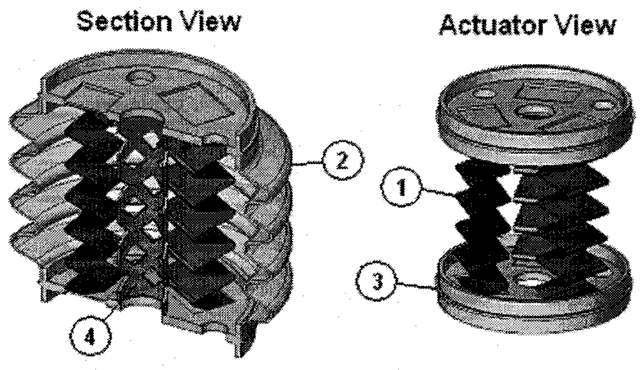

Figure 3-7: Prototype design

Figure 3-7 illustrates a single unit module of the proposed four-module manipulator. Item #1 shows the position and arrangement of the SMA actuators. The three actuators provide three degrees of freedom: pitch, yaw, and vertical linear motion. The four-stage manipulator would then have a total of 12 degrees of freedom, leading to 2^{12} (4096) different manipulator configurations. The outer shell (item #2) is designed as a miniature bellows to provide little resistance in the direction of motion. It is manufactured using highly flexible polyurethane rubber. The actuators are fixed to the lightweight fibreglass support plates (or vertebrae) shown by item #3. The plates have a centre hole and three smaller holes at the periphery to provide air circulation.

The forth component is a highly flexible porous ventilating tube. Its purpose is to evenly distribute the cold air to all sections of the manipulator. In theory, the size of the ventilating holes in the tube should diminish as the unit module is actuated, to reduce the amount of cold air pumped in that section. As the section stretches to its original length, the holes in the inner tube increase and air is allowed to flow in that section. Figure 3-8 shows the direction of airflow through the ventilating tubes to the actuators of the manipulator.

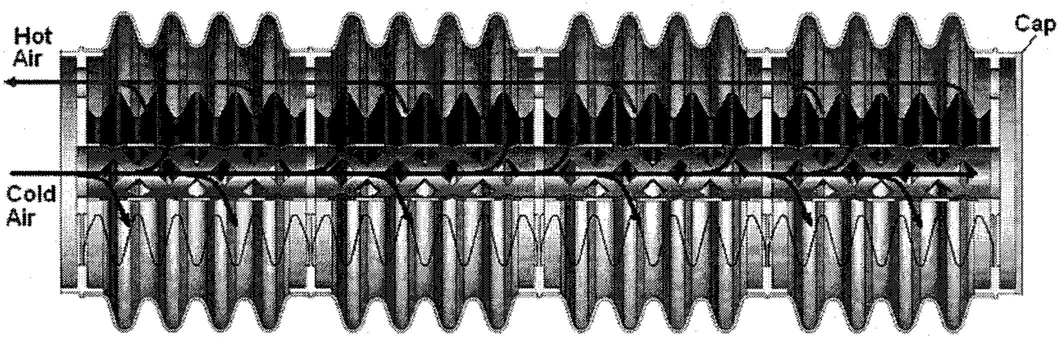

Figure 3-8: Airflow path

3.2.3 Static Analysis

A simple static analysis was performed to determine the approximate forces required to maintain adequate structural integrity. The performance criterion is as follows: the manipulator should remain in a horizontal position when fully stretched. It is assumed that the minimum pressure should be greater or equal to the maximum compressive stresses generated by the bending moment at the base of the first unit module (assuming the manipulator has a rigid structure). Figure 3-9 shows the positions of the acting forces and the resulting moment.

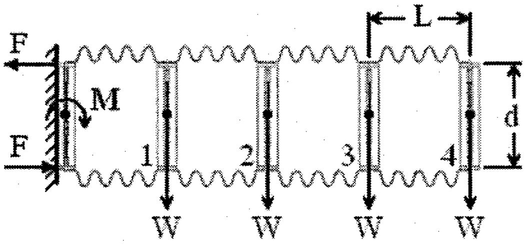

Figure 3-9: Manipulator free-body diagram

To avoid underestimating the required forces, the weight of the unit module is taken at the tip of the supporting plate and the resulting moment is calculated at the base of the manipulator. The dimensions l and d are the length and diameter of the unit module and are set at 30mm and 20mm respectively (note that l is the maximum length in the un-actuated state). The mass of the unit module is estimated based on 1) early experimental prototypes, 2) CAD weight estimations and 3) material volume. The mass of each component and the method of estimation are given in Table 3-2.

Table 3-2: Unit module mass breakdown

Component	Method	Mass [g]
Actuator	2	0.2/each
Support Plate	3	1.0
Wire	3	1.0
Bellows	1	1.4
Epoxy	3	0.5
	Total	4.5

The moment is calculated using the following equation:

$$M = WL + 2WL + 3WL + 4WL = 10WL \qquad \textbf{(3-10)}$$

The maximum compressive stress σ_{MAX} is located at the bottom of the first module and is given by:

$$\sigma_{MAX} = Mr/S\ , \quad S = \pi * r^4/4 \qquad \textbf{(3-11)}$$

where S is the moment of inertia for a circular section and r is the unit module radius. For the manipulator to remain in a horizontal position the minimum pressure must be greater or equal to the maximum compressive stress, or $P \geq \sigma_{MAX}$. The maximum force F_p applied to the unit module is simply the stress multiplied by the area.

$$\begin{aligned} F_p &= P * A_{SECTION} \\ F_p &= \sigma_{MAX} * A_{SECTION} \end{aligned} \qquad \textbf{(3-12)}$$

Solving (3-10) to (3-12) results in an internal pressure of around 17kPa and a force of 5.4N, however the individual actuator force would be slightly lower than the rated value due to the offset location of the actuator within the module. Neglecting the gravity effects, the approximate actuator forces were computed based on the diagrams of Figure 3-10. Due to the low resistance of martensite, the effects of the un-actuated SMAs were neglected and the actuator forces depend only on the number of actuated SMAs and the pressure force F_p. The actuator forces are computed for three cases: one, two and three actuated SMAs. The free-body diagrams for the three cases are shown in Figure 3-10, where the subscript *0* represents the un-actuated side.

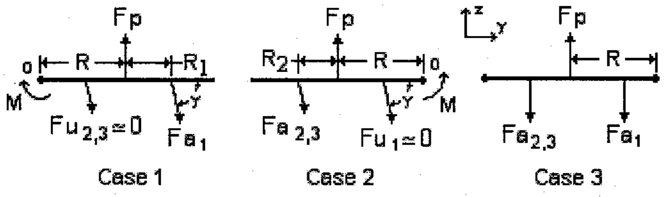

Figure 3-10: Actuator force and moment diagrams

In the single actuator case, the actuator force is given by (3-13).

$$F_{a_1} = \left(\frac{R}{R+R_1}\right)\left(\frac{F_p}{\sin(\gamma)}\right) \tag{3-13}$$

As stated in the following chapter, $R = 10\text{mm}$, $R_1 = 6\text{mm}$, $F_p = 5{,}4\text{N}$ and $\gamma_{approx} = 75°$. For the second case, the actuator force is given by:

$$F_{a_2} = \frac{1}{2}\left(\frac{R}{R+R_2}\right)\left(\frac{F_p}{\sin(\gamma)}\right) \tag{3-14}$$

Where $R_2 = 3\text{mm}$ and $\gamma_{approx} = 60°$. In the third case the actuation force is simply given by:

$$F_{a_3} = {}^{F_p}\!/_{3} \tag{3-15}$$

The resulting actuator forces are F_{a1} = 3.8N, F_{a2} = 2.4N and F_{a3} = 1.8N. In the case of the fully un-actuated module, the actuator lengths are equal to the maximum bellows length.

Chapter 4:
SMA Actuator Model

The results obtained from the approximate elastoplastic analysis demonstrated that a sinusoidal shape sheet miniature actuator was capable of high strains while satisfying the force requirements of the proposed manipulator. The following analysis explores the shape memory constitutive behaviour in order to obtain a better assessment of the mechanical characteristics of the actuator.

Early constitutive models focused on the unidirectional tensile properties of SMAs [45]. In 1996, J.G. Boyd proposed a bi-directional model in which the applied strain was decomposed into elastic, temperature and phase transformation components using a free energy function and dissipation potential [4]. C. Lexcellent proposed a micromechanical model based on the Helmholtz free energy expression that could describe the intermediary martensite states (twinned and detwinned) [27]. This model was expanded by Tanaka to include the effects of local back stress on the volume fraction of martensite. In recent years, models based on the microscopic behaviour of SMAs were developed in which the overall properties could be obtained using an averaging process [22]. However, most constitutive models offer only quantitative descriptions of the SMA behaviour for specific actuator configurations and are by no means capable of describing the complex constitutive behaviour of all actuator types. The two-phase model proposed by X. Peng was used to model the SMA sheet actuator proposed in this study [37]. This model is based on the concept that an SMA is dynamically composed of austenite and martensite, and the constitutive behaviour is a dynamic combination of the elastic behaviour of austenite and the elastoplastic behaviour of martensite [37]. This model was chosen for its relative simplicity and its ability to treat stresses and strains independently. The latter is critical in the analysis of the bending actuator since the internal stresses vary along the SMA cross-section.

4.1 TWO-PHASE CONSTITUTIVE MODEL

4.1.1 Model Description

The following sections describe the two-phase constitutive model established by X. Peng and its application to the proposed SMA actuator [37]. The model describes the evolution of the volume fraction of martensite based on temperature and stress or strain inputs. It assumes that the material is plastically incompressible and that the transformation lattice volume change is negligible compared to the lattice shear deformation [43]. It also assumes that the material will be subjected to small deformations and that the strain rate or stress rate is small enough such that the martensitic transformation stress and work dissipation remain relatively constant [46]. Algebraically, the macroscopic deviatoric stress $\boldsymbol{s}$ and volumetric stress σ_{kk} of the two-phase SMA model are represented by:

$$s = \bar{s}_A + \bar{s}_M = \begin{bmatrix} \sigma_{11} - \sigma_{kk} & \sigma_{12} & \sigma_{13} \\ \sigma_{21} & \sigma_{22} - \sigma_{kk} & \sigma_{23} \\ \sigma_{31} & \sigma_{32} & \sigma_{33} - \sigma_{kk} \end{bmatrix}$$

$$\sigma_{kk} = \left(\bar{\sigma}_{kk}\right)_A + \left(\bar{\sigma}_{kk}\right)_M = \frac{\sigma_{11} + \sigma_{22} + \sigma_{33}}{3} \tag{4-1}$$

where the subscripts *A* and *M* represent the austenite and martensite contributions to the overall stress. It is assumed that in a polycrystalline SMA there is no relationship between the stresses in a SMA and its two phases [43]. The deviatoric strain $\boldsymbol{e}$ consists of an elastic component $\boldsymbol{e}^e$, a plastic component $\boldsymbol{e}^P$ and a phase transformation component $\boldsymbol{e}^T$.

$$e = e^e + e^P + e^T \tag{4-2}$$

With the assumption that the overall strain *e* and the transformation strain e^T are identical for both phases, the conventional mixture theory states that:

$$\begin{aligned} \bar{s}_M &= \xi(s_M) \\ \bar{s}_A &= (1-\xi)s_A \end{aligned}, \quad \begin{aligned} \left(\bar{\sigma}_{kk}\right)_M &= \xi(\sigma_{kk})_M \\ \left(\bar{\sigma}_{kk}\right)_A &= (1-\xi)(\sigma_{kk})_A \end{aligned} \tag{4-3}$$

where ξ is the volume fraction of martensite, s_M and $(\sigma_{kk})_M$ are the respective deviatoric and volumetric stress components of martensite and s_A and $(\sigma_{kk})_A$ are the respective deviatoric and volumetric stress components of austenite. To account for the dynamic change in volume fraction, the deviatoric stresses of (4-1) can be rewritten in a more general form,

$$\bar{s}_A = \bar{s}_A\left(e, e^T, T, \xi\right), \qquad \bar{s}_M = \bar{s}_M\left(e, e^T, T, \xi, p^{(r)}\right) \tag{4-4}$$

Where T is the temperature and $p^{(r)}$ is a set of internal variables related to the irreversible deformation characteristic of the constitutive behaviour of martensite [37]. The internal variables $p^{(r)}$ are illustrated in the mechanical model proposed by W.D. Iwan. Elastic and plastic components are represented by a parallel set of springs and dashpot elements as shown in Figure 4-1 [31].

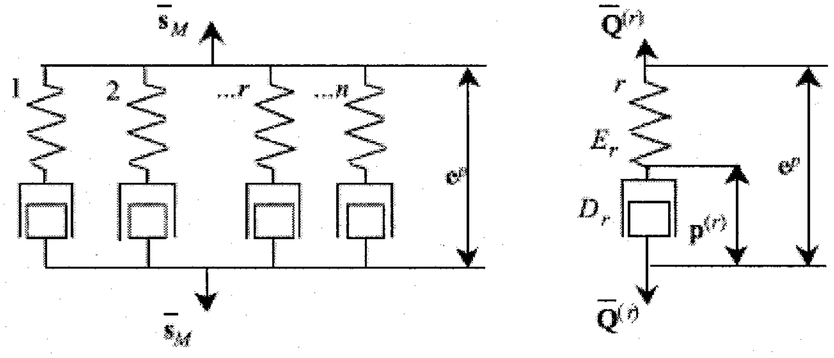

Figure 4-1: Mechanical model of the stress of martensite (adapted from [37])

The internal variable $\mathbf{p}^{(r)}$ corresponds to the displacement of the dashpot element D_r and the total displacement of all the r^{th} elements corresponds to the plastic strain component e^P, the variable E_r is related to the stochastic internal structures and the energy stored in E_r corresponds to that stored in the micro-stress fields induced by the respective pattern of defects at the micro level [37]. The dashpot elements D_r have a macroscopic average plastic damping coefficient $\overline{a}_r$ and the spring elements E_r have a macroscopic average stiffness $\overline{C}_r$, both function of temperature and martensite volume fraction. $\overline{Q}^{(r)}$ is the generalized force conjugated with the r$^{\text{th}}$ internal variable $p^{(r)}$ and the following inequality should be satisfied if any change occurs to $p^{(r)}$ [14].

$$\overline{Q}^{(r)} : dp^{(r)} \geq 0 \qquad r = 1,2,\ldots,n \tag{4-5}$$

The colon operator represents a tensor contraction, where,

$$X = Y : Z \rightarrow X_{cd} = \sum_{a,b} Y_{ab} Z_{abcd}\,, \tag{4-6}$$

and $$A = B : C \rightarrow A = \sum_{f,g} B_{fg} C_{fg}$$

The deviatoric martensite stress is equal to the summation of all the $\overline{Q}^{(r)}$ elements.

$$\bar{s}_M = \sum_{r=1}^{n} \overline{Q}^{(r)} \tag{4-7}$$

From Figure 4-1, $\overline{Q}^{(r)}$ relates to the spring and dashpot elements with the following relationships:

$$\overline{Q}^{(r)} = \overline{C}_r(T,\xi)\left(e^P - p^{(r)}\right), \quad \overline{Q}^{(r)} = \overline{a}_r(T,\xi)\, dp^{(r)}\big/ dz \tag{4-8}$$

P. Sittner et al. [40] have demonstrated that under biaxial loading conditions some SMAs did not obey the von Mises rule of equivalent stress (did not show isotropic response). The generalized time variable *z* was introduced to describe this phenomenon. It accounts for anisotropic material properties through the tensor of rank four ***P*** and the change in plastic damping capabilities of the dashpot elements *f(z)*. The generalized time is represented by the following relationship:

$$dz = \frac{d\varsigma}{f(z)}, \qquad (d\varsigma)^2 = de^P : P : de^P \tag{4-9}$$

In this case de^P is a 3x3 tensor of rank two (3x3 matrix) and ***P*** is a 3x3x3x3 tensor of rank four. In the case of the double contraction of (4-9), $d\varsigma$ is scalar.

The differentiation of (4-8) results in:

$$d\overline{Q}^{(r)} = \overline{C}_r(T,\xi)de^P + \left(\frac{1}{\overline{C}_r}\frac{\partial \overline{C}_r}{\partial T}dT + \frac{1}{\overline{C}_r}\frac{\partial \overline{C}_r}{\partial \xi}d\xi - \alpha_r dz \right)\overline{Q}^{(r)}, \quad \alpha_r = \frac{\overline{C}_r}{a_r} \tag{4-10}$$

Substituting this result into (4-7) yields:

$$d\overline{s}_M = \sum_{r=1}^{n} d\overline{Q}^{(r)} = \overline{A}de^P + \overline{B}dz + \overline{C}dT + \overline{D}d\xi \tag{4-11}$$

where,

$$\overline{A} = \sum_{r=1}^{n}\overline{C}_r, \quad \overline{B} = -\sum_{r=1}^{n}\alpha_r\overline{Q}^{(r)}, \quad \overline{C} = \sum_{r=1}^{n}\frac{1}{\overline{C}_r}\frac{\partial \overline{C}_r}{\partial T}\overline{Q}^{(r)}, \quad \overline{D} = \sum_{r=1}^{n}\frac{1}{\overline{C}_r}\frac{\partial \overline{C}_r}{\partial \xi}\overline{Q}^{(r)} \tag{4-12}$$

It is known that the temperature-induced reverse martensitic transformation causes the recovery of the distortion lattice, which is related to both the current states of plastic strain and martensitic phase transformation strain [37]. The variation in phase transformation strain is assumed to behave linearly.

$$de^T = \frac{1}{2}k_t\left(e^P + e^T\right)\left(\frac{\partial \xi}{\partial T}dT - \left|\frac{\partial \xi}{\partial T}dT\right|\right) \tag{4-13}$$

where k_t is a material constant. The variation in phase transformation strain occurs only during the reverse martensitic transformation (when $(e^P+e^T) \neq 0$ and $((\partial\xi/\partial T)\,dT < 0)$.

The deviatoric elastic response of austenite and martensite are related to the macroscopic average shear modulus $\overline{G}_{A,M}$ through the following relation:

$$\bar{s}_M = 2\overline{G}_M(T,\xi)\left(e - e^P - e^T\right), \quad \bar{s}_A = 2\overline{G}_A(T,\xi)\left(e - e^T\right) \tag{4-14}$$

The differential of (4-14) yields:

$$\begin{aligned} d\bar{s}_M &= 2\overline{G}_M\left(de - de^P - de^T\right) + \frac{\bar{s}_M}{\overline{G}_M}\left(\frac{\partial \overline{G}_M}{\partial T}dT + \frac{\partial \overline{G}_M}{\partial \xi}d\xi\right), \\ d\bar{s}_A &= 2\overline{G}_A\left(de - de^T\right) + \frac{\bar{s}_A}{\overline{G}_A}\left(\frac{\partial \overline{G}_A}{\partial T}dT + \frac{\partial \overline{G}_A}{\partial \xi}d\xi\right) \end{aligned} \tag{4-15}$$

The volumetric stress for austenite and martensite and their differentials are given by:

$$\begin{aligned} \left(\bar{\sigma}_{kk}\right)_M &= 3\overline{K}_M(T,\xi)\left[\varepsilon_{kk} - 3\alpha_M(T)(T - T_0)\right], \\ \left(\bar{\sigma}_{kk}\right)_A &= 3\overline{K}_A(T,\xi)\left[\varepsilon_{kk} - 3\alpha_A(T)(T - T_0)\right] \end{aligned} \tag{4-16}$$

$$\begin{aligned} \left(d\bar{\sigma}_{kk}\right)_M &= 3\overline{K}_M d\varepsilon_{kk} + \frac{1}{\overline{K}_M}\frac{\partial \overline{K}_M}{\partial \xi}\left(\bar{\sigma}_{kk}\right)_M d\xi \\ &+ \left[\frac{1}{\overline{K}_M}\frac{\partial \overline{K}_M}{\partial T}\left(\bar{\sigma}_{kk}\right)_M - 9\frac{\partial \alpha_M}{\partial T}\overline{K}_M(T - T_0) - 9\alpha_M\overline{K}_M\right]dT, \\ \left(d\bar{\sigma}_{kk}\right)_A &= 3\overline{K}_A d\varepsilon_{kk} + \frac{1}{\overline{K}_A}\frac{\partial \overline{K}_A}{\partial \xi}\left(\bar{\sigma}_{kk}\right)_A d\xi \\ &+ \left[\frac{1}{\overline{K}_A}\frac{\partial \overline{K}_A}{\partial T}\left(\bar{\sigma}_{kk}\right)_A - 9\frac{\partial \alpha_A}{\partial T}\overline{K}_A(T - T_0) - 9\alpha_A\overline{K}_A\right]dT, \end{aligned} \tag{4-17}$$

In (4-16) and (4-17), T_0 is the reference temperature, ε_{kk} is the volumetric strain, $\overline{K}(T,\xi)$ is the macroscopic average elastic volumetric modulus and $\alpha(T)$ is the thermal expansion coefficient for both martensite and austenite.

K. Tanaka suggested an expression for the volume fraction ξ. It states that the volume fraction is a function of temperature, applied stress and material properties [45].

$$\xi = \begin{cases} 1-\exp\left[-A_M\langle M_S + B_M\sigma_e - T\rangle\right] & A \rightarrow M \\ \exp\left[-A_A\langle T-(A_S + B_A\sigma_e)\rangle\right] & M \rightarrow A \end{cases} \quad \textbf{(4-18)}$$

where,

$$\langle\phi\rangle = \begin{cases} \phi & if\ \phi > 0 \\ 0 & if\ \phi \le 0 \end{cases} \quad \textbf{(4-19)}$$

The differential of (4-18) is given by:

$$d\xi = \begin{cases} A_M(1-\xi)(B_M d\sigma_e - dT) & A \rightarrow M \\ -A_A\xi(dT - B_A d\sigma_e) & M \rightarrow A \end{cases} \quad \textbf{(4-20)}$$

The parameters M_S and A_S denote the martensite and austenite transformation start temperatures, the material constants A_M, B_M, A_A and B_A are related to the phase transformation and the equivalent stress σ_e is defined by:

$$\sigma_e = \sqrt{\frac{3}{2}s:P:s} \quad \textbf{(4-21)}$$

4.1.2 Analytical Simplifications

It was found that the effects of temperature on the material constants could be neglected [37]. The material studied, Au-47.5 at. % Cd, did not show any signs of isotropic hardening and behaved isotropically under uniaxial behaviour, therefore *f(z)* was set to 1 and ***P*** was set as the identity tensor. This simplification is also made for the Nitinol shape memory alloy used to fabricate the actuators since its mechanical properties are closely related to the Au-Cd memory alloy. The following austenite material relations are simplified under these assumptions:

$$\begin{aligned}\overline{G}_A &= (1-\xi)G_A^0 \\ \overline{K}_A &= (1-\xi)K_A^0\end{aligned} \tag{4-22}$$

And,

$$\begin{aligned}\overline{G}_M &= \xi G_M^0 \\ \overline{K}_M &= \xi K_M^0\end{aligned}, \qquad \begin{aligned}\overline{a}_r &= \xi a_r^0 \\ \overline{C}_r &= \xi C_r^0\end{aligned} \tag{4-23}$$

All material properties are taken at the reference temperature T_0, as indicated by the superscript *0*. The material properties can be determined experimentally using a tensile test as described in Appendix B. The equivalent stress σ_e being no longer dependent on the material properties is simply given by:

$$\sigma_e = \sqrt{\frac{3}{2}s:s} \tag{4-24}$$

And the generalized time becomes:

$$dz = \sqrt{de^P : de^P} \tag{4-25}$$

4.1.3 Numerical Implementation

The two-phase constitutive model can be used in either stress or strain control mode. Since the stress field in the sheet actuator is difficult to obtain due to geometry, strain is chosen as the control variable. Several manipulations were required to compute the internal variables using the strain control mode and these were obtained from the paper presented by X. Peng [37]. The differential of the deviatoric stress of martensite in (4-15) was combined with (4-11) to generate:

$$\left(\bar{A}+2\bar{G}_M\right)de^P=-\bar{B}dz+d\bar{\psi} \tag{4-26}$$

where,

$$d\bar{\psi}=2\bar{G}_M\left(de-de^T\right)-\left(\bar{C}-\frac{\bar{s}_M}{\bar{G}_M}\frac{\partial\bar{G}_M}{\partial T}\right)dT-\left(\bar{D}-\frac{\bar{s}_M}{\bar{G}_M}\frac{\partial\bar{G}_M}{\partial\xi}\right)d\xi \tag{4-27}$$

Substituting (4-26) into (4-25) yields:

$$\left[\bar{B}:\bar{B}-\left(\bar{A}+2\bar{G}_M\right)^2\right]dz^2-\left(2\bar{B}:d\bar{\psi}\right)dz+d\bar{\psi}:d\bar{\psi}=0 \tag{4-28}$$

4.1.4 Algorithm

The SMA actuator is subjected to temperature and extension variations. The maximum actuator extension E_{max} is computed based on the 3% maximum surface strain, where y_e is calculated with (3-4).

$$E_{\max}=\frac{y_e\left(\theta_0-d\theta_{\max}\right)-y_e\left(\theta_0\right)}{y_e\left(\theta_0\right)} \tag{4-29}$$

The $d\theta$ history was obtained by solving (3-5) for a given actuator strain history. The SMA cross-section strain history was then acquired with (3-6) and then converted into deviatoric strain $\boldsymbol{e}$ and volumetric strain ε_{kk} according to (4-30).

$$\varepsilon = \begin{bmatrix} \varepsilon_{11} & \varepsilon_{21} & \varepsilon_{31} \\ \varepsilon_{21} & \varepsilon_{22} & \varepsilon_{32} \\ \varepsilon_{31} & \varepsilon_{32} & \varepsilon_{33} \end{bmatrix}, \ \varepsilon_{kk} = \frac{\varepsilon_{11} + \varepsilon_{22} + \varepsilon_{33}}{3}, \ e = \begin{bmatrix} \varepsilon_{11} - \varepsilon_{kk} & \varepsilon_{12} & \varepsilon_{13} \\ \varepsilon_{21} & \varepsilon_{22} - \varepsilon_{kk} & \varepsilon_{23} \\ \varepsilon_{31} & \varepsilon_{32} & \varepsilon_{33} - \varepsilon_{kk} \end{bmatrix} \qquad \textbf{(4-30)}$$

With the temperature and deviatoric strain histories, $d\xi$ and de^T were obtained via (4-16) and (4-10) respectively; dz was obtained by solving (4-25) followed by de^P and $d\overline{Q}^{(r)}$ with (4-23) and (4-7), and then $d\overline{s}_M$ with (4-8). On the other hand $d\overline{s}_A$ was simply calculated using (4-12) and the total deviatoric stress s was calculated with (4-1).

To obtain the actuator output force and displacement, the cross-section of the SMA sheet is divided into 51 partitions. The algorithm runs through the entire strain and temperature history for each partition. The actuator moment M and output force F are then calculated using (3-8) and (3-9) respectively and plotted against the total strain E. A flow diagram of the numerical calculations is shown in Figure 4-2 and the source code for the two-phase constitutive model can be found in Appendix C.

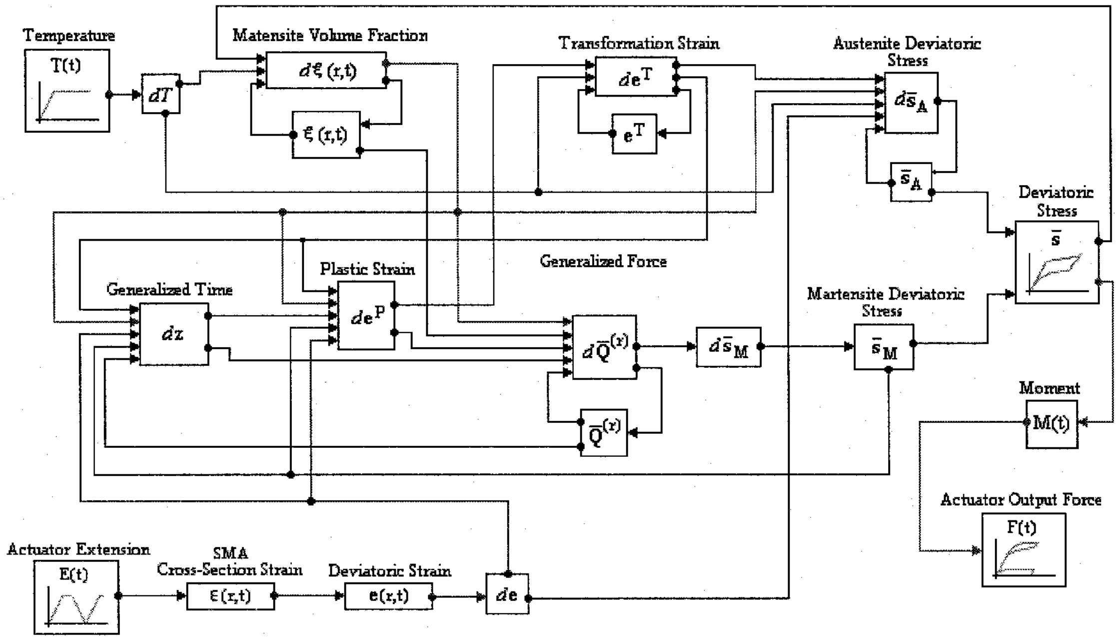

Figure 4-2: Model block diagram

4.2 SMA AND ACTUATOR RESPONSE

The validity of the constitute model proposed by X. Peng was assessed using the detailed results of the uniaxial behaviour of SMA Au-47.5 at.% Cd provided by N. Nakanishi [34]. To satisfy the requirements of both accuracy and efficiency in the analysis of practical engineering problems, r = 3mm in (4-5) through (4-7) and (4-10) through (4-12) [47]. Material properties of martensite and austenite for NiTi SMA were obtained from the manufacturer: Johnson Matthey.

$$G_M^0 = 13.0 \text{ GPa}, \ G_A^0 = 31.0 \text{ GPa}, \ \nu_M = \nu_A = 0.33.$$

The other parameters were extrapolated by comparing the material properties listed above with the ones presented in X. Peng's analysis.

$$C_{1,2,3}^0 = 550,\ 13,\ 1.3 \text{ GPa}, \quad \alpha_{1,2,3} = 28000,\ 750\ 80,$$

$$A_A, B_A, A_M, B_M = 0.45, 60, 0.25, 30, \qquad k_t = 3.2,$$

$$A_S, A_F, M_S, M_F = 345, 358, 331, 303 \text{ K}.$$

To examine the ferroelastic property of martensite, the temperature was maintained below the martensite transition finish temperature M_F and loaded to the maximum strain of 3%. Figure 4-3 illustrates the elastoplastic deformation and the large residual strains present after unloading. In Figures 4-4, 4-5 and 4-6, the vertical axis represents the maximum positive stress located at the surface of the SMA strip.

In Figure 4-3, the actuator reached a maximum stress of 43.4 MPa. This is approximately 2½ times higher the maximum stress reached by the SMA Au 47.5 at.%Cd which has a shear modulus three times lower than NiTi.

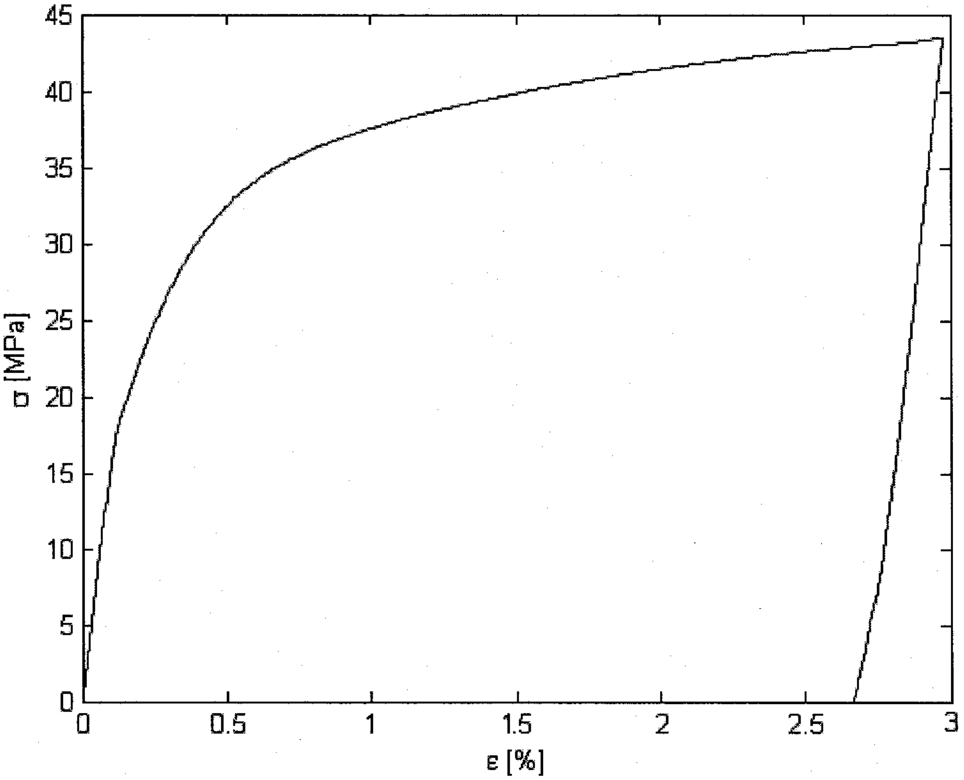

Figure 4-3: Ferroelastic analysis: martensite loading and unloading curve

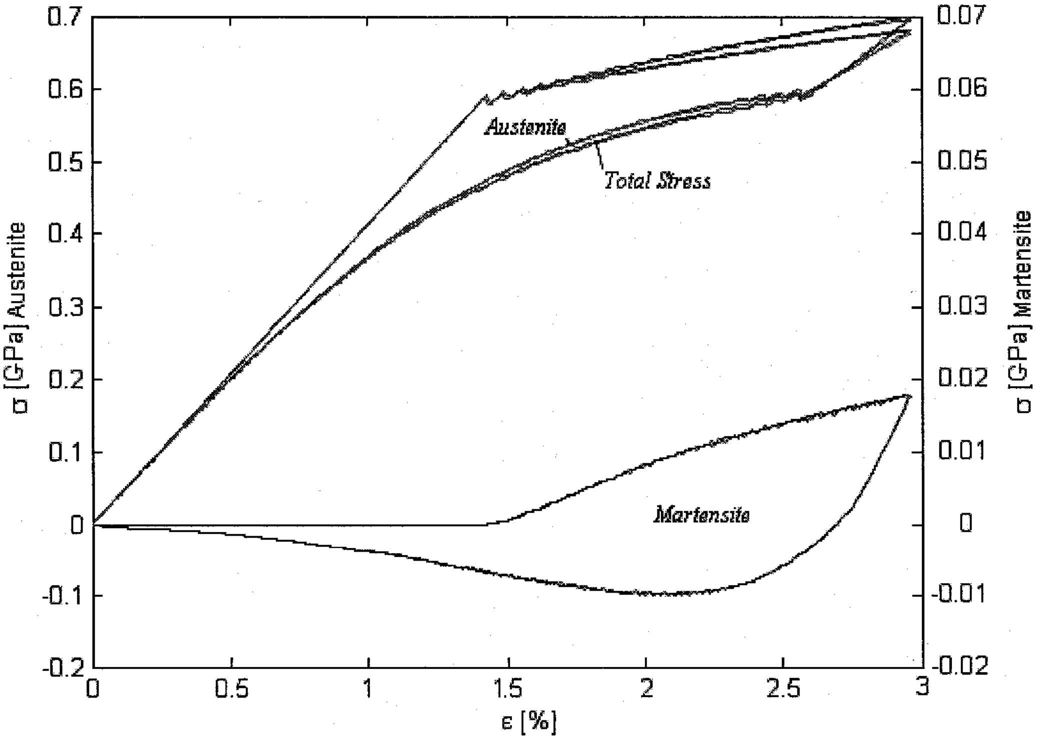

Figure 4-4: Pseudoelasticity of NiTi at 84°C (357 K)

The pseudoelastic behaviour occurs as the temperature is close to the austenite transition finish temperature A_F. Figure 4-4 shows the behaviour of both austenite and martensite phases at a temperature of $T \approx A_F = 84°$. Although the austenite phase was assumed to be elastic, the combination of both phases is pseudoelastic.

Under no load, the material is completely composed of austenite. At the approximate strain of 1.5% the term $M_S + B_M\sigma_e$ surpasses T and induces martensitic transformation. Upon unloading, the reverse martensitic transformation occurs as $A_S + B_A\sigma_e$ falls below T. The saw tooth shape of the austenite curve in the forward martensitic transformation region may have been caused by the lack of smoothing functions on the differential stress variable, however it will be shown that the actual SMA material exhibited a similar response under an applied tensile load. The model shows identical results for negative strains. The results can be found in Appendix D.

The SMA actuator response at different temperatures is shown in Figure 4-5. At temperatures well above the austenite finish temperature (T = 112 °C > A_F = 85 °C), the response is almost completely elastic and the hysteresis loop is almost completely eliminated (the SMA was composed of over 96% austenite). Raising the temperature to 127 °C (400 K) completely inhibits martensitic transformation. The material remains in the austenite phase and the response is completely elastic. For temperatures below the austenite start temperature ($T < A_S$ = 72°C) the SMA is composed entirely of martensite.

The output force characteristics of the actuator were obtained from (3-8) and (3-9). The initial shape parameters of the actuator are listed below, where t is the thickness and w is the width of the SMA strip. The force-displacement results are shown in Figure 4-6.

$$l\,(= l_l + l_c) = 2.7\text{mm}, \quad r_l = 0.4\text{mm}, \quad t = 0.070\text{mm}, \quad w = 7.0\text{mm}.$$

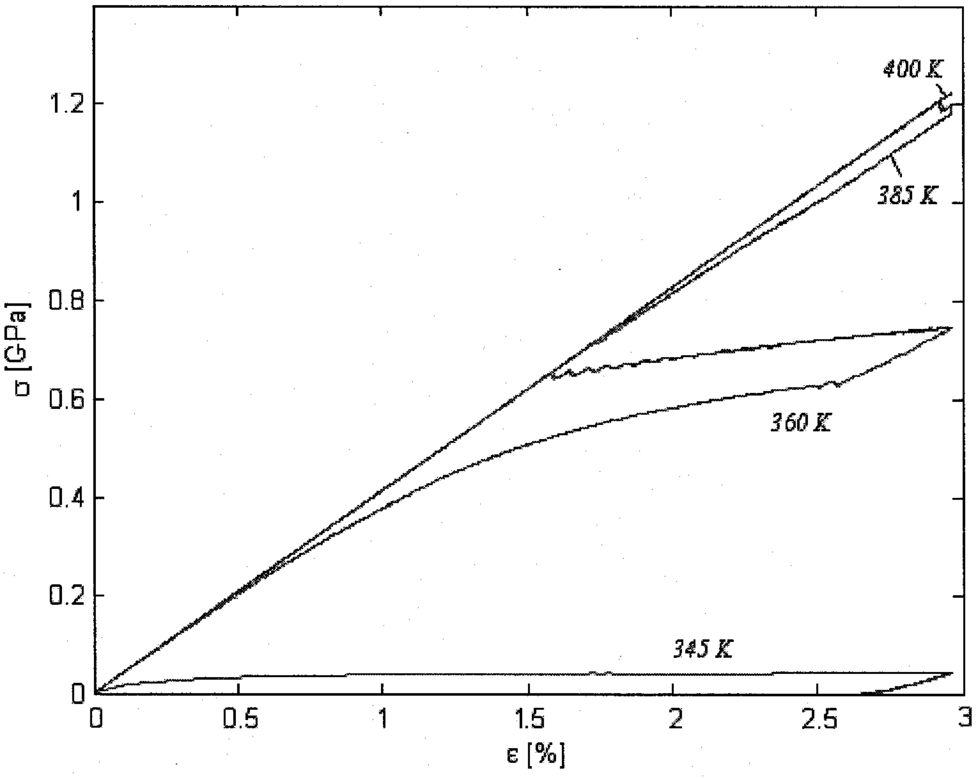

Figure 4-5: NiTi tensile response at different temperatures

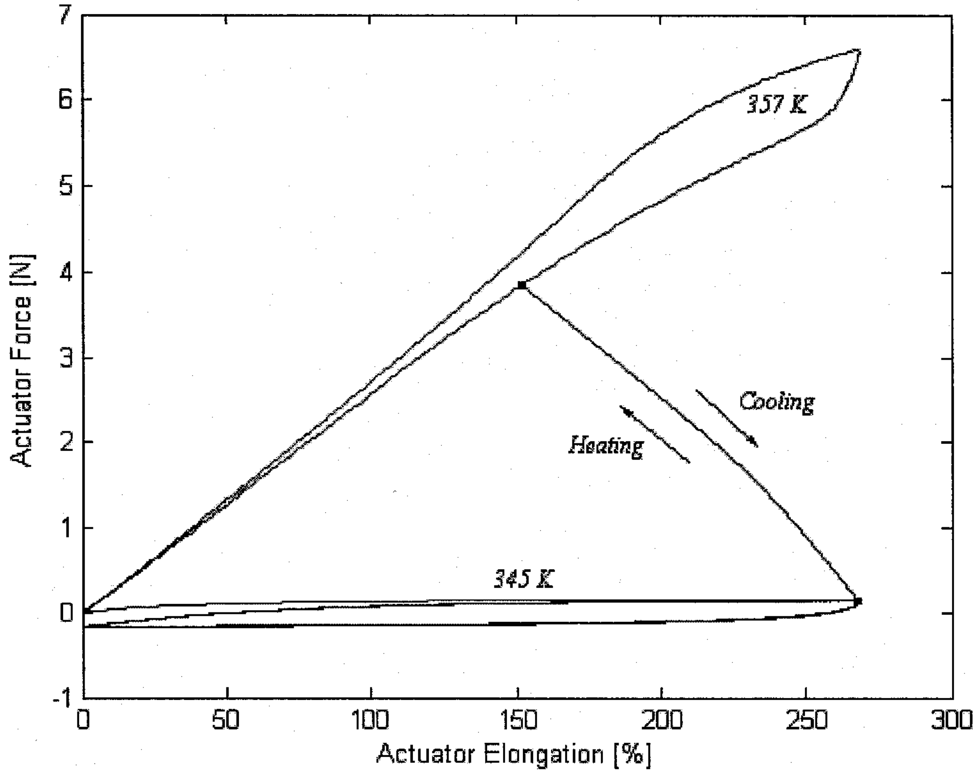

Figure 4-6: Actuator force-displacement response

The two-phase constitutive model demonstrated that the sheet actuator is capable of larger forces and larger displacements compared to the estimated output force generated using the elastic-plastic model of Figure 3-5. The output force of the actuator is approximately 1N greater for SMA sheet thickness 37% thinner and a narrower width (higher forces can be obtained by increasing the width of the SMA strip).

Due to the elastoplastic behaviour of martensite the actuator response at 345 K exhibits a negative output force as the strain decreases. This residual force is quickly recovered as the temperature is increased above the austenite start temperature. This behaviour is of no concern since the actuator does not operate in this region.

4.3 ACTUATOR SIZING

4.3.1 Geometric, Material and Electrical Constraints

The maximum allowable space is defined to obtain the maximum force output from an optimally sized actuator. The shaded regions of Figure 4-7 represent the space available to the un-stretched SMA actuator based on a 20mm internal diameter. The design allows for a 2mm gap between each actuator and between the actuators and the outer wall. The latter is expected to increase once the actuator is stretched within its working range. From the figure, the maximum size of the actuator is 4mm long by 7mm wide.

It was found that high training strains could induce cracks in the SMA material. In a study by C.D. Lagoudas [26], a maximum training strain of 10.5% was used in experiments on Nitinol wire. The proposed actuator is formed using flat SMA strips and the maximum training strain is dependent on the radius and on the thickness of the strip. The length L_0 at the centre of curvature R_0 remains constant during the bending process and the maximum strain occurs on the outer edge at r_2 as seen in Figure 4-8.

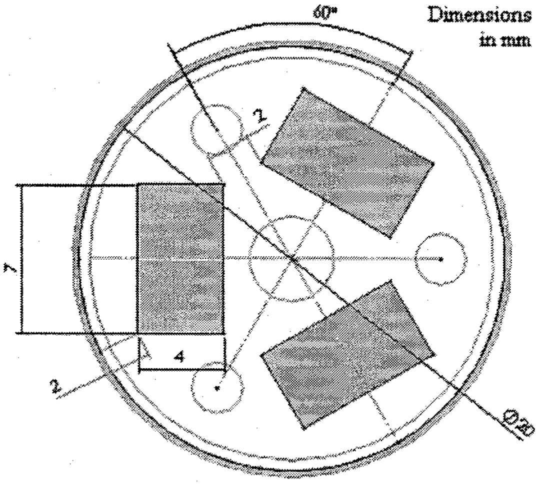

Figure 4-7: Vertebra top view - actuator locations

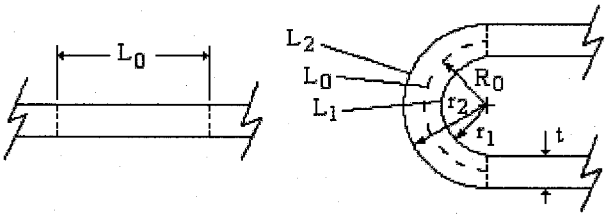

Figure 4-8: Bend radius

The following relation gives the strain on the outer surface of the bend:

$$\%_{MAX} = \left(\frac{r_1 + t}{t}\right)\ln\left(\frac{r_1 + t}{r_1}\right) - 1 \tag{4-31}$$

With the maximum training strain of 10.5%, the maximum SMA sheet thickness was calculated for several radii.

Table 4-1: Maximum SMA sheet thickness

Bend Radius [mm]	Strain %	Thickness [mm]
0.26	10.57	0.059
0.30	10.56	0.068
0.34	10.55	0.077
0.38	10.54	0.086

The actuator's electrical resistance is primarily a function of the SMA cross-section. The power requirements depend on the largely on the SMAs resistance and, to a certain extent, on the actuator shape and local environment. A list of several SMA actuators and their heating currents is given in Table 4-2 and the current per square millimetre is computed for each case.

Table 4-2: Actuator currents

SMA Shape	**Reference**	**Area [mm^2]**	**Current [mA]**	**Amps/mm^2**
Flat sheet	[30]	0.011	60	5
Wire	[10]	0.050	700	14
Wire	[23]	0.018	400	22
Wire	[38]	0.070	1800	25
Flat sheet	[13]	0.004	100	28
Wire	[28]	0.002	60	30

With a current of 5Amps/mm^2, a sheet actuator with a width of 7mm and a thickness of 0.070mm would require approximately 10 Amps to reach the desired temperature. Therefore, to limit the power consumption, the maximum thickness of the SMA strip was set at 0.070mm.

4.3.2 Performance Criteria

The unit module of the proposed design can bend in two axes by activating any combination of one or two actuators and can compress vertically by activating all three actuators. The goal is to achieve a deflection of over 45° using a single actuator. Assuming that the length of the un-actuated edge of the outer shell remains constant, the position of the module and the actuator lengths can be extrapolated from Figure 4-9.

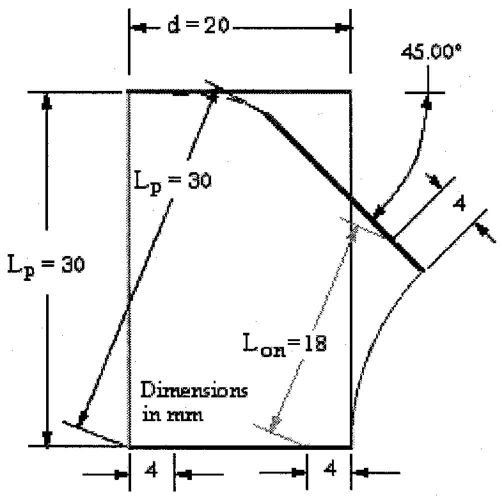

Figure 4-9: Actuated unit module

The un-actuated length L_p of the proposed unit module (when pressurized) is set at 30mm and is assumed to remain constant throughout actuation. The actuated module shown in Figure 4-9 has an inclination of 45° and an actuator *ON* length of around 18 mm. The approximate variation of the actuated and un-actuated SMA lengths with respect to the deflection angle is shown in Figure 4-10.

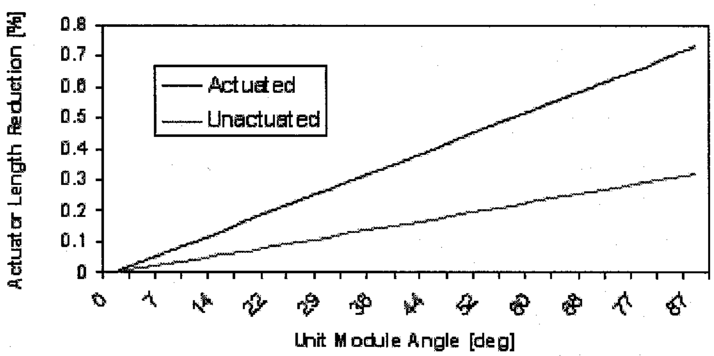

Figure 4-10: Actuator length

At an inclination of 90°, the actuated SMA exhibits length reduction of 75% (from the stretched position) resulting in an actuator length of 8 mm. The length of the un-actuated SMA also decreases but was not taken into consideration due to the low forces involved. For the purpose of generating initial geometric parameters, the actuator *ON* length was set at 20 mm (for a single SMA strip).

The two-phase constitutive model adopted in the previous section assumed that the strains in both austenite and martensite were identical to the overall strain in the SMA sheet and that the maximum total actuator strain was independent of the martensite volume fraction [37]. The maximum strain is reached when the manipulator is fully stretched (actuator in the *OFF* state). This strain as well as the strain required to obtain the desired unit module inclination $\%_{design}$ are expressed below.

$$\%_{off} = \frac{L_{off} - L_0}{L_0}, \quad \%_{design} = \frac{L_{on} - L_0}{L_0} \qquad \textbf{(4-32)}$$

The maximum strain $\%_{off}$ was obtained from the extreme right point on the force displacement plot. The required strain at full actuation $\%_{design}$ was determined by combining (4-31) and (4-32). With L_{off} = 30mm and L_{on} = 20mm, the design strain is given by:

$$\%_{on} = \frac{L_{on}}{L_{off}}\left(1 + \%_{off}\right) - 1 = \frac{2}{3}\left(1 + \%_{off}\right) - 1 \qquad \textbf{(4-33)}$$

Once this value was obtained, the actuator output force could be extrapolated from a force/displacement curve as shown in Figure 4-11. The actuator has a maximum extension of 255%. To obtain a deflection of 45°, the actuator must compress to 135% of its memorized length. At this strain level the actuator exerts a force exceeding 4 N. The upper force plateau occurs during the forward martensitic transformation (A→M) and the lower force arises during the reverse transformation (M→A). The lower curve was used to determine the shape parameters of the SMA actuator since actuation is a result of the reverse transformation.

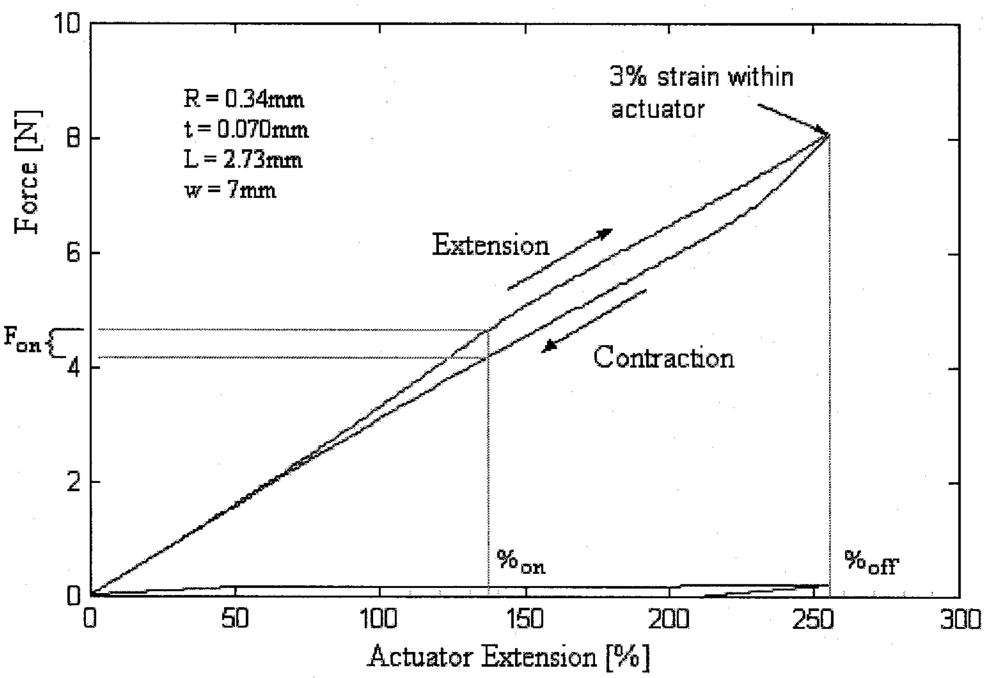

Figure 4-11: Actuator force-displacement curve

4.3.3 Geometric Parameter Selection

The output characteristics of several actuator sizes were computed and the design strains were compared for each case. The first iteration consisted of determining the effects of bend radii and sheet thickness on the output force. In this trial, all actuators had the same 4×7mm projected area when un-stretched (see Figure 4-7). Output forces were plotted for four different radii and five thicknesses. For each radius, the test is performed up to the maximum rated thickness determined by (4-31). For clarity, only the reverse transformation load line is presented.

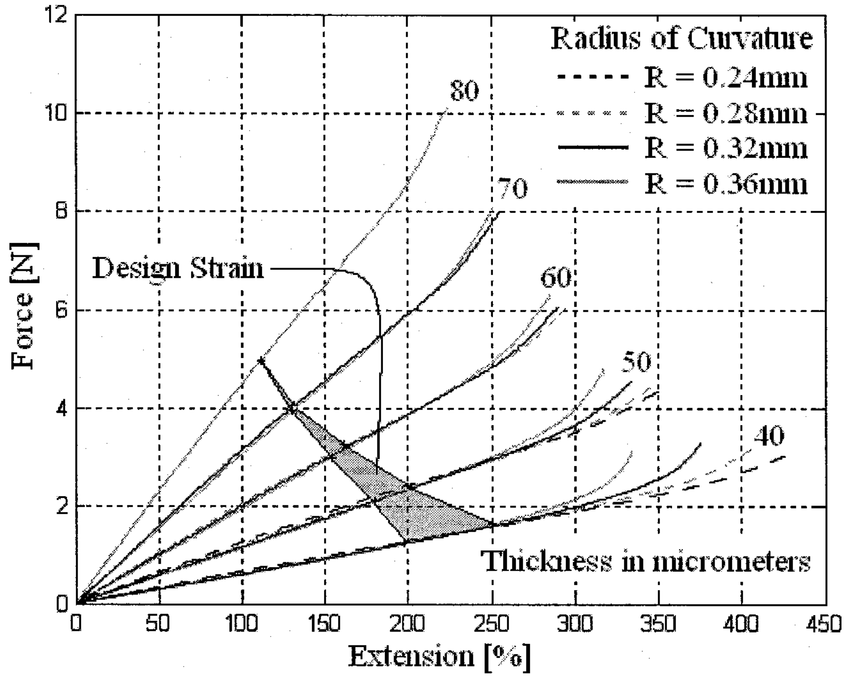

Figure 4-12: Actuator force-displacement curves for selected actuator thicknesses

The shaded area in Figure 4-12 indicates the strain required to obtain a 45° inclination. It is clear from the figure that the output force is primarily controlled by the thickness of the SMA sheet. A minimum sheet thickness of 65μm is required to achieve the required force of 3.8N. The output is also directly proportional to the width of the sheet. From a power consumption point of view, the optimal dimensions are those resulting in the lowest cross-sectional area since lower cross-sections have higher resistances and thus lower power requirements. Based on this criterion, the optimum width required to produce an output force of 3.8N is approximated for several thicknesses and the results are shown in Table 4-3.

Table 4-3: Actuator cross-section at F = 3.8N

Thickness [μm]	**Width required to obtain F ≈ 3.8N** [mm]	**Cross-Section Area** [mm^2]
60	8	0.480
65	7	0.455
70	5.93	0.415
75	5.31	0.398
80	4.8	0.384
85	4.27	0.363
90	4	0.360

The results demonstrated that the actuator cross-section diminishes with an increasing thickness and levels out at a thickness of about 90μm. The largest drop in cross-section is between 65 and 70μm. Following the design constraints set in Section 3.2, the actuator cross-sectional dimensions were selected as 0.070×5.9mm. According to Table 4-1, the minimum bend radius for a 70μm sheet is 0.31mm. The optimal bend radius was found from the output characteristics of actuators with bend radii between 0.31 and 0.40mm. The comparison is shown in Figure 4-13.

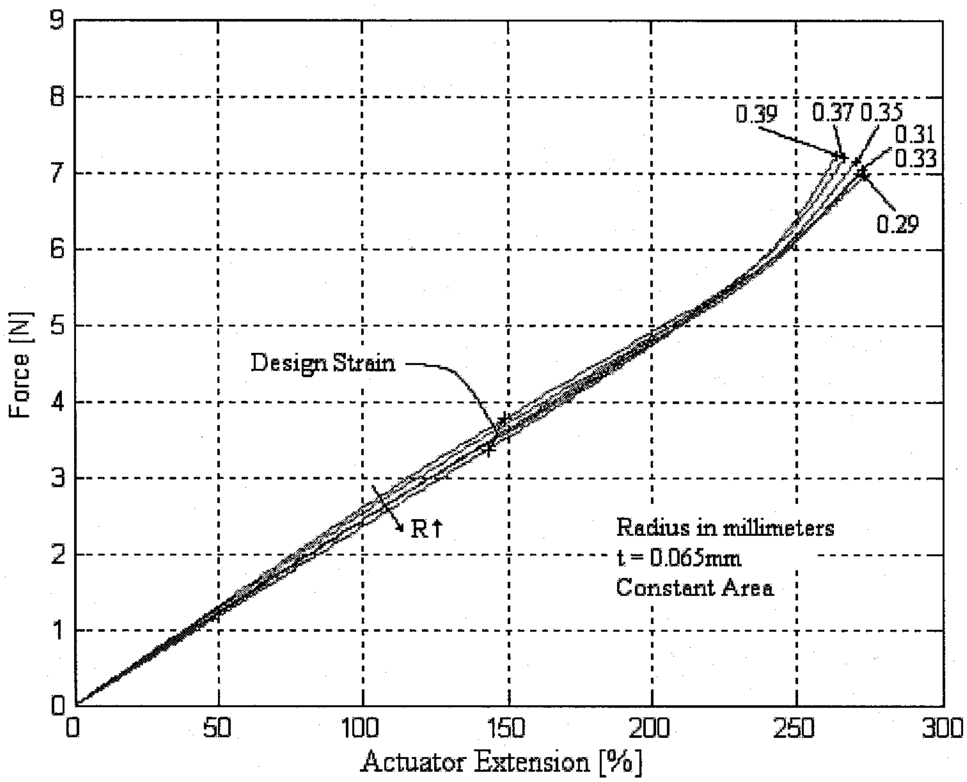

Figure 4-13: Actuator force-displacement curves for several actuator radii

The actuator with the smallest bend radius produced the highest displacements and the highest output forces. Both force and displacement diminished as the radius was increased. For the purpose of this project, the radius of curvature was selected to be at least 0.31mm and no more than 0.40mm since higher radii would produce output forces lower than 3.8 N.

The un-stretched actuator length was obtained by solving for L_o in either the *ON* or *OFF* versions of (4-32) and is equal to approximately 8.3mm. The un-stretched actuator is composed of 11 circular sections and is shown in Figure 4-14.

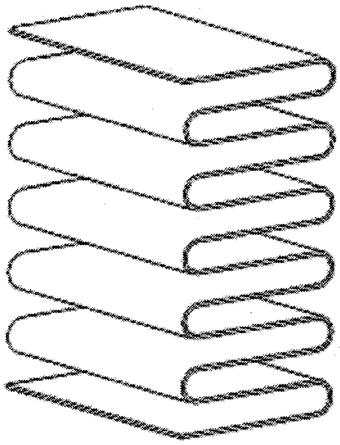

Figure 4-14: Scale actuator design

Chapter 5:
Control System

The forward kinematics used in this model is based on the principle of binary actuation. Although there are no mechanisms restraining the actuators in fixed positions, the model assumes that each actuator has only two states on the basis that the variance in actuator length remains small under low end-effector loads. Since there are currently no closed form solutions to the Jacobian matrix, the transition times between forward and reverse transformations are also neglected [12]. The complete forward kinematics are computed ahead of time and the workspace parameters are stored in memory. The controller is based on the minimum position error. It locates the manipulator configuration closest to the desired position by searching within the workspace.

5.1 FORWARD KINEMATICS

5.1.1 Initial Approximation

Each state can be defined by three rotational and three translational kinematic variables and represented by a four-by-four homogeneous transformation matrix. The triangular configuration of the actuators leads to kinematic coupling and reduces the number of independent variables to two rotations and one translation: pitch, yaw and vertical displacement. As mentioned in Chapter 3, each module is capable of eight different configurations resulting in eight different homogeneous transformation matrices per module. The fixed frame *0* is located at the base of the manipulator and the moving frame *4* is attached at the tip of the end-effector module.

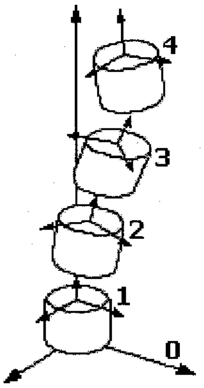

Figure 5-1: Manipulator reference frame

The forward kinematics for the four-stage manipulator $A_{0,4}$ is simply the combination of the transformation matrix of each module: $A_{0,1}$ to $A_{3,4}$.

$$A_{0,4} = A_{0,1}A_{1,2}A_{2,3}A_{3,4} \tag{5-1}$$

To eliminate the need for complex derivations, specific transformation matrices are developed for each of the eight states shown in Figure 5-2.

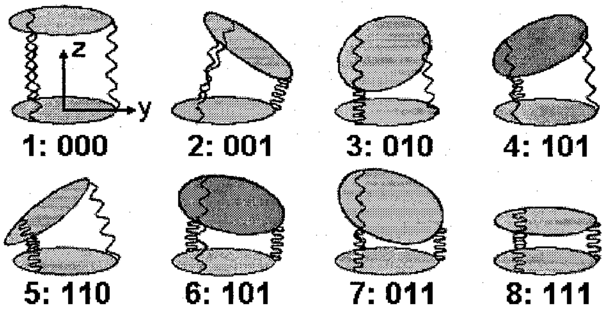

Figure 5-2: Module configurations

Since the actuation system is not truly discrete, the transformation matrix of a particular stage must also take into account the gravity forces and moments of each successive stage, however the resulting moments applied to each stage can only be determined once the relative position of each stage is known. As a result, an approximation of the forward kinematics was used to obtain the moments applied to each stage. The applied moments are then used to compute new actuator lengths and a new set of forward kinematics.

The unit module homogeneous transformation matrix is composed of a rotation matrix R and a displacement vector X and is given by:

$$A_{i-1,i} = \begin{bmatrix} R_{3x3} & \overline{X}^{i}_{3x1} \\ \overline{0}^{T}_{3x1} & 1 \end{bmatrix} \tag{5-2}$$

The rotation matrix R and displacement vector X for states *2* and *5* are given by (5-3), where $D_h = D_y$.

$$R = \begin{bmatrix} 1 & 0 & 0 \\ 0 & \cos\alpha & -\sin\alpha \\ 0 & \sin\alpha & \cos\alpha \end{bmatrix} \qquad \overline{X} = \begin{bmatrix} 0 \\ D_y \\ D_z \end{bmatrix} \tag{5-3}$$

The vertical displacement D_z is the z component of the displacement vector X and the horizontal displacement D_h is the y component. For these two states the displacement in the x-axis is zero. The relations between the actuator lengths, unit module inclination and deflection were derived from the cross-section view of Figure 5-3.

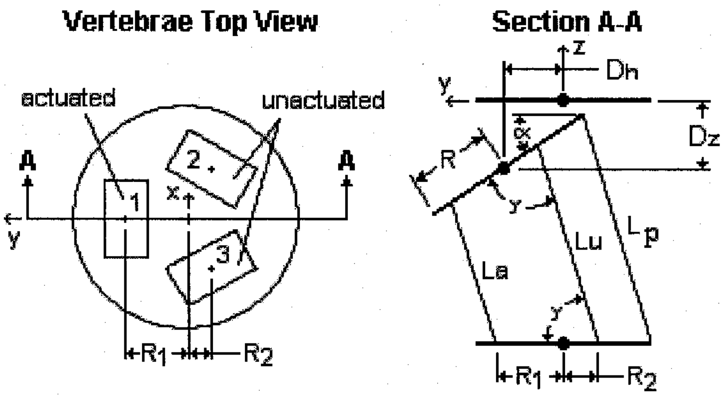

Figure 5-3: Unit module cross-section view

It is assumed that the bellows wall length L_p on the un-actuated side of the module remains constant throughout actuation except for the case in which all three actuators are activated. It is also assumed that the angle gamma between the actuator lengths and the vertebra are equal for all three lengths: L_p, L_a and L_u. The relation between the actuated and un-actuated length is given by:

$$L_u = L_a + \frac{(R_1 + R_2)(L_p - L_a)}{(R + R_1)} \tag{5-4}$$

The angles α and γ are found by solving:

$$\sin(\alpha) = \frac{(L_p - L_a)\sin(\gamma)}{R + R_1}, \quad \cos(\gamma) = \frac{(R + R_1)(\cos(\alpha) - 1)}{L_a - L_p} \tag{5-5}$$

And the vertical and horizontal displacements, D_z and D_h, are given by:

$$D_z = L_p(1 - \sin(\gamma)) + R\sin(\alpha), \qquad D_h = L_p\cos(\gamma) + R(\cos(\alpha) - 1) \tag{5-6}$$

The actuator forces computed in Chapter 3 equal to $F_{a1} = 3.8\text{N}$, $F_{a2} = 2.4\text{N}$ and $F_{a3} = 1.8\text{N}$. The actuated lengths were computed based on the elastic response of austenite.

$$L_a = {}^{F_a}\!/_{E_A} + L_{0A} \tag{5-7}$$

where E_A is the approximate elastic modulus of austenite computed from Figure 5-4 and L_{0A} is the actuator length at zero strain. The austenite and martensite properties were approximated from the diagram of Figure 5-4. The actuated SMA lengths for cases *1*, *2* and *3* were computed as 17.6mm, 13.9mm and 12.6mm respectfully. Using (5-4) to (5-7), the unit module angle α as well as the horizontal and vertical displacements, D_h and D_z, were computed and used to construct the homogeneous transformation matrices.

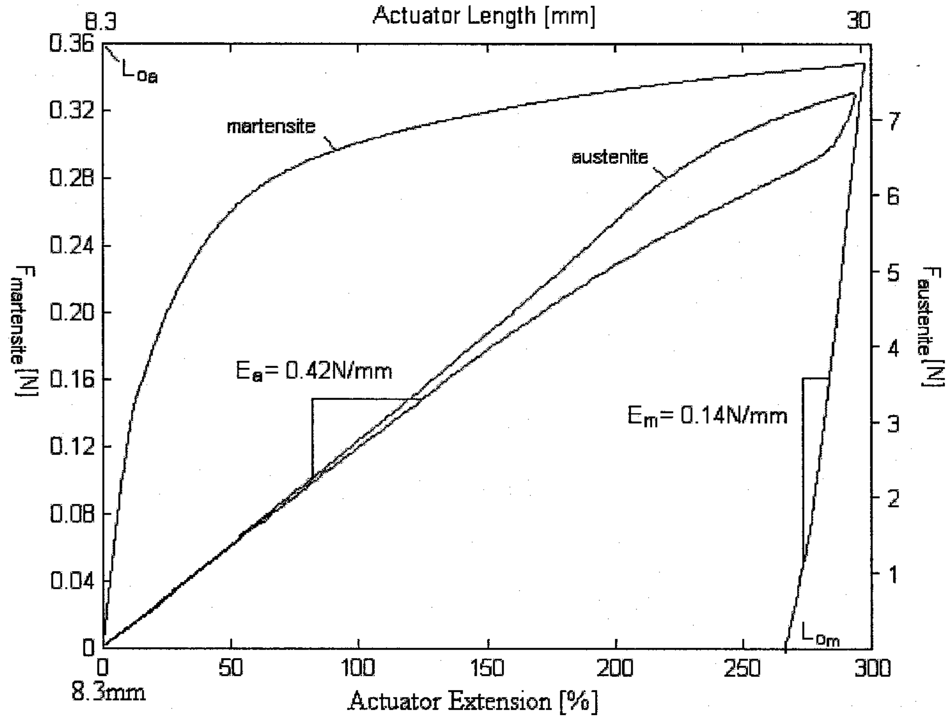

Figure 5-4: SMA elastic modulus

The rotation matrices and displacement vectors of states *3*, *4*, *6* and *7* are obtained by rotating the results of states *2* and *5* by ±120° about the vertical axis. The 4096 transformation matrices were obtained by computing each state combination and the end-effector positions are plotted in Figure 5-5. The Matlab m-files for the approximate forward kinematics and rotational conversions are given in Appendix E.

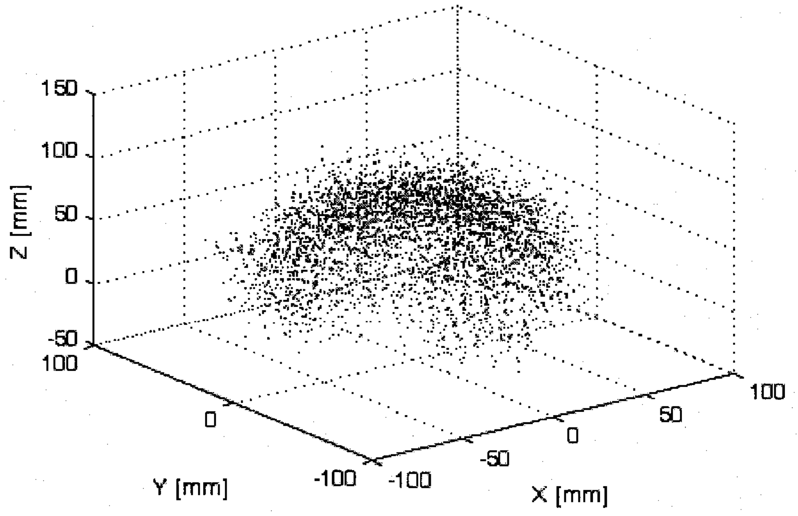

Figure 5-5: Workspace approximation

From Figure 5-5, it is clear that the workspace distribution is non-uniform. Optimization of the workspace in terms of the density of reachable states the state redundancy is an area of continuing research and will not be discussed [12].

5.1.2 Refined Forward Kinematics

Based on the approximate module positions, the moments generated by, and applied to, each module were computed and used to generate a new set of forward kinematics. With this information, the transformation matrix of each module is adjusted starting with the end-effector module and the procedure is repeated until the workspace converges. The refining algorithm is presented below and the source code is given in Appendix G.

- Obtain $A_{0,4}$ and $A_{0,3}$.
- Compute Δx, $\Delta y = y_{0,4}-y_{0,3}$ and moments M_x, $M_y = W(\Delta x)$ in the global reference frame (W is the unit module weight).
- Transform moments and forces in the local coordinates of module 3.
- Compute the new $A_{2,3}$ using one of the eight state algorithms (See Appendix F).
- Using the new $A_{2,3}$, revise $A_{0,4}$, $A_{0,3}$ and $A_{0,2}$.
- Compute Δy, $\Delta x = (x_{0,4}-x_{0,2})+(x_{0,3}-x_{0,2})$ and obtain moments in global reference frame then transform in the local coordinate system of module 2.
- Obtain the new $A_{1,2}$ using the appropriate state algorithm (See Appendix F).
- Using the new $A_{1,2}$, revise $A_{0,4}$, $A_{0,3}$, $A_{0,2}$ and $A_{0,1}$.
- Compute Δy, $\Delta x = (x_{0,4}-x_{0,1})+(x_{0,3}-x_{0,1}) +(x_{0,2}-x_{0,1})$ and moments in global reference frame then transform in the local coordinate system of module 1.
- Obtain the new $A_{0,1}$ using the appropriate state algorithm (See Appendix F).
- Compute the new $A_{0,4}$ and repeat for all other manipulator configurations
- Iterate entire process until the end-effector position is negligible (based on a selected manipulator end-effector configuration).

5.1.3 Manipulator Workspace

The sequence of operations is repeated for all 4096 states and the entire process is iterated until the change in the end-effector position becomes negligible. A manipulator configuration with an end-effector position located on the workspace periphery is most likely to be affected by the gravity forces and bending moments. As a result, the manipulator configuration {*4,4,1,1*} from the base to the end-effector was chosen as the reference point in determining the convergence of the refined forward kinematics algorithm. The end-effector coordinates computed from the approximate forward kinematics and two iterations of the refined forward kinematics algorithm are given in Table 5-1.

Table 5-1: Change in end-effector position for configuration 4-4-1-1

Coordinates	Initial Estimate	1st Iteration	2nd Iteration
x	-75.54	-76.72	-76.73
y	-43.61	-44.38	-44.39
z	43.04	34.07	33.95

As expected, the weight of the unit modules significantly reduces the location of the z-coordinate. The end-effector vertical coordinate converges to 33.95 after the second iteration. The workspace generated by the refined forward kinematics algorithm is shown in Figure 5-6 along side the results from the approximate kinematics.

5.2 INVERSE KINEMATICS

Since the workspace consists of a number of discrete points, there exists no closed form solution to the inverse kinematics problem. Within the workspace core of Figure 5-6, there exists a large number manipulator configurations leading to comparable solutions and for each additional unit module, the number manipulator configurations increase exponentially.

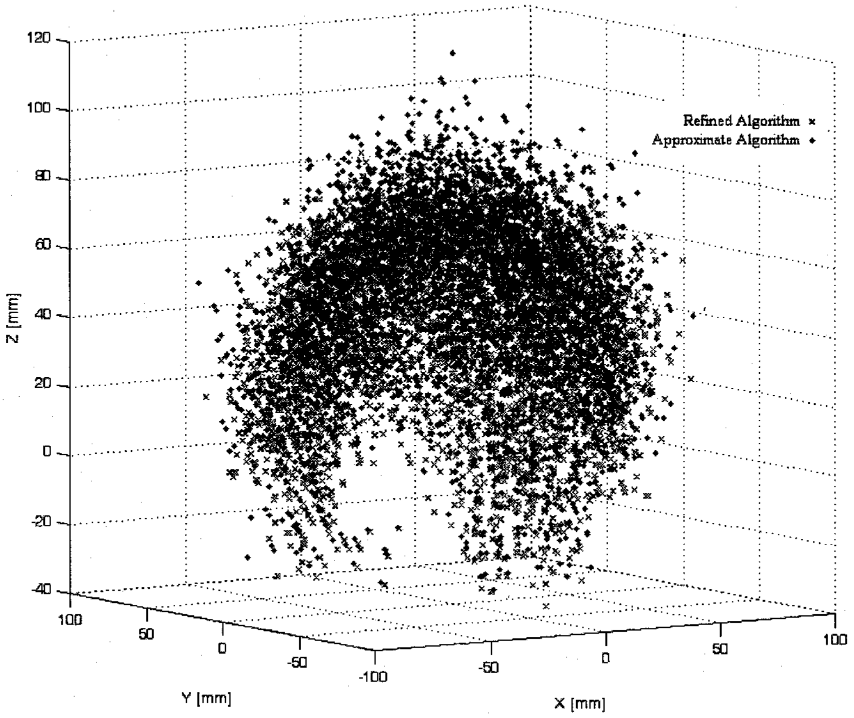

Figure 5-6: Approximate and refined manipulator workspace

A number of studies have tackled the optimization of the inverse kinematics problem in redundant devices [9,11,32,50,54]. Genetic and combinational heuristics algorithms have been used directly to solve the inverse kinematics of discrete devices [12]. Hyper radial basis functions in combination with neural networks are able to solve the inverse kinematics problem of non-discrete redundant robotic systems through a learning process and fitness and energy minimization functions have been developed to eliminate the complexities of the non-linear differential equations [8,51].

With such a large number of solutions, the inverse kinematics problem can be regarded as an entire field of research in itself and is not the focus of this research. The inverse kinematics of the proposed compliant manipulator is composed of a simple sort and search algorithm. The end-effector coordinates are organized in ascending order of elevation and an exhaustive search algorithm is used to find the closest point to the desired position of the end-effector.

5.3 CONTROLLER MODEL

The manipulator controller is based on the open loop Matlab Simulink model shown in Figure 5-7. It transforms the states generated by the inverse kinematics algorithm into a sequence of seven pulsed signals used to activate the electronic amplifiers.

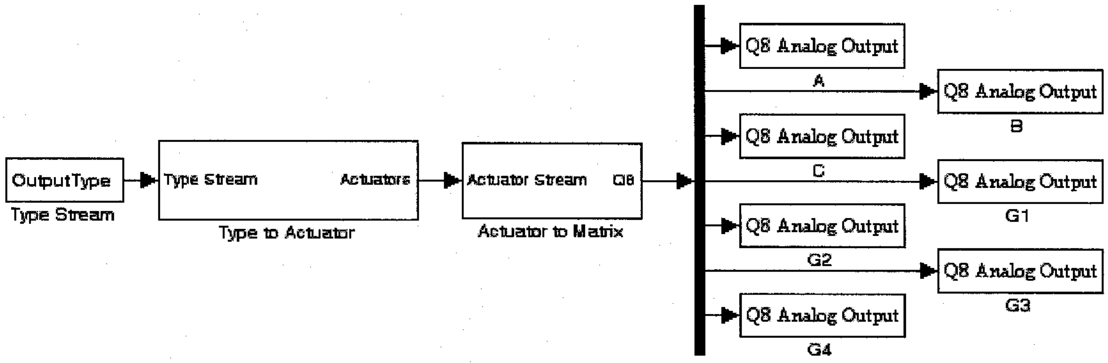

Figure 5-7: Manipulator controller

The user inputs a desired end-effector coordinate and the inverse kinematics algorithm locates the closest match from within the workspace and sends the module state information to the *type stream* block. The *type to actuator* converts each unit module state into an array defining the status of each actuator (*ON* or *OFF*). The *actuator to matrix* then piggybacks the actuator states on timed discrete signals indigenous to each actuator (the block diagrams for both functions can be found in Appendix I). The control signals are then sent to one of the three lead amplifiers (marked *A*, *B* and *C*) or one of the four ground amplifiers (marked *G1* to *G4*) via the Quanser Q8 input/output interface. The significance of each amplifier is discussed in the following chapter.

Chapter 6:
Actuation System

6.1 HEAT TRANSFER ANALYSIS

The martensitic transformation (austenite to martensite) is displacive, athermal (time independent), first order (liberates heat), associated with a hysteresis and occurs over a temperature span in which both phases exist [53]. During the reverse transformation, the austenite forms twinned martensite with little volume change. Twinned martensite is then transformed into deformed martensite through the application of small stresses and large strains. Heating the material above the austenite finish temperature A_f induces the formation of the austenite phase. The following analysis will describe two possible methods of electrical heating: continuous and discontinuous heating.

6.1.1 Continuous Heating

Electrical heating is the most commonly used method to induce the reverse martensitic transformation. The current required to heat an SMA actuator and maintain it above A_f can be obtained from the following heat-transfer equation [33]:

$$mc_P\left(\frac{dT}{dt}\right) = i^2 R - hA(T - T_\infty) \qquad \textbf{(6-1)}$$

where m is the mass of the SMA actuator, c_P is the specific heat of the austenite phase, T is the instantaneous temperature of the actuator in Kelvin, T_∞ is the ambient temperature in Kelvin, i is the current in the actuator, R is the resistance of the actuator, h is the coefficient of convective heat-transfer and A is the surface area of the actuator. The equation above can be reformulated to obtain the steady state current i_{ss} with respect to the steady state temperature T_{ss}.

$$i_{ss} = \sqrt{hA\left(T_{ss} - T_{\infty}\right)/R} \tag{6-2}$$

Due to the complex shape of the actuator, the convective heat transfer coefficient was computed based on the experimental results of vertical flat plates in still air, in which the active length is equal to the total length of all the circular sections of the actuator (the derivation is found in Appendix J). The SMA material produced by Johnson-Matthey exhibit an approximate 20% difference in resistance between austenite and martensite. Since the actuator is composed of austenite at steady state, the resistance R is calculated based on the resistivity of the austenite phase. The details can be found in Appendix K.

Given the actuator dimensions of 0.070mm×5.9mm×53.2mm, the heat transfer coefficient h is evaluated at $134\mathrm{Wm^{-2}C^{-1}}$. From the two-phase constitutive model, the austenite finish temperature A_f is assumed to be 87°C. The total resistance of the SMA composite actuator (circular sections and composite flat sections) is computed as 0.0450Ω. From (6-2), the current required to maintain the actuator temperature above A_f in still air at 27°C is equal to 3.9Amps.

6.1.2 Discontinuous Heating

R. Mukherjee first proposed using the thermal inertia properties of the SMA material to heat SMA actuators using short current pulses [33]. With this method, the actuator temperature fluctuates between T_1 and T_2, as shown in Figure 6-1. At steady state, the temperature T_2 must be the higher than austenite finish temperature A_f to ensure a complete phase transformation. Actuators are heated for τ seconds over a $n\tau$ time period where n is the number of actuators.

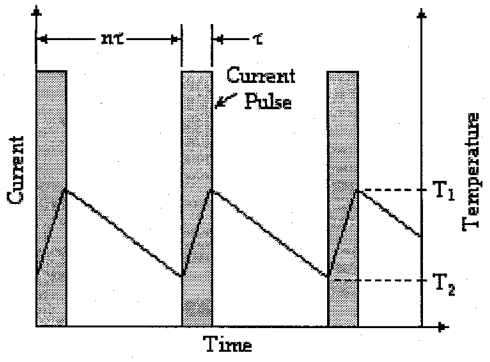

Figure 6-1: Discontinuous versus continuous heating (adapted from [33])

The current required to maintain the temperature T_2 above A_f is obtained by solving (6-1) at the boundary conditions. The result is given below and the complete derivation can be found in Appendix K.

$$i_d = \sqrt{\frac{hA}{R}(T_2 - T_\infty)\left[\frac{\exp(\Lambda n) - 1}{\exp(\Lambda) - 1}\right]}, \qquad \Lambda \propto \frac{hA\tau}{mc_P} \tag{6-3}$$

According to (6-3), the current is dependant only on the temperature T_2 and the pulse width τ. For the proposed design, n is equal to 12. The specific heat of the SMA material produced by Johnson Matthey is approximately 0.837J/gK. From the CAD model, the mass of the circular sections of the actuator is estimated at $3.81e^{-8}$g with a surface area of $8.44e^{-5}m^2$. The lumped parameter hA/mc_P is computed to be 0.355Hz. If the pulse width is lower than 10ms, the exponential term *exp(Λ)* can be truncated after the second term of its power series and the term *exp(Λn)* can be truncated after the third term with little integrity loss [33]. Expanding and simplifying (6-3) gives:

$$i_d = \sqrt{\frac{hA}{R}(T_2 - T_\infty)n\left(1 + \frac{1}{2}\Lambda n\right)} \tag{6-4}$$

If the pulse width τ is reduced even further, the parameter Λ can be eliminated from (6-4) and the current relation is simplified to, where i_{ss} is the steady state current given by (6-2).

$$i_d = \sqrt{\frac{nhA}{R}\left(T_2 - T_\infty\right)} = \sqrt{n} \times i_{ss} \tag{6-5}$$

Assuming an ambient temperature of 27°C and a lower bound temperature T_2 of 87°C, the results of (6-3) to (6-5) are given for different pulse widths.

Table 6-1: Required current

Equation	**Pulse Width (τ) [ms]**				
	1000	100	10	1	0.1
6-3	49.70	14.89	13.58	13.47	13.45
6-4	14.59	13.57	13.46	13.45	13.45
6-5	13.45	13.45	13.45	13.45	13.45

For pulse widths smaller than 10ms, the relation between the current and the lower bound temperature is independent of τ. Therefore, the current can be accurately estimated by multiplying the steady state current by the square-root of the number of actuators.

6.2 ACTUATOR DRIVER MATRIX

In essence, hyper-redundant manipulators have a large number of actuators. Since each actuator is controlled independently, the simplest method of actuation consists of one lead wire for each actuator and a common ground. For a manipulator with three actuators per unit module, the number of wires in the base module would be equal to $3n+1$ where n is the number of unit modules. In the proposed design, the base module would have 13 wires passing through the base module. This becomes a problem for millimetre-sized manipulators, where the limited space constrains the total number of lead wires that can be used.

The solution proposed by R. Mukherjee organizes the actuators in a matrix like fashion [33]. The actuators (marked 1 to 12) are arranged in a 3×4 matrix as seen in

Figure 6-2. The actuators are connected to three lead wires (marked *A*, *B* and *C*) and four ground wires (marked *G1* to *G4*).

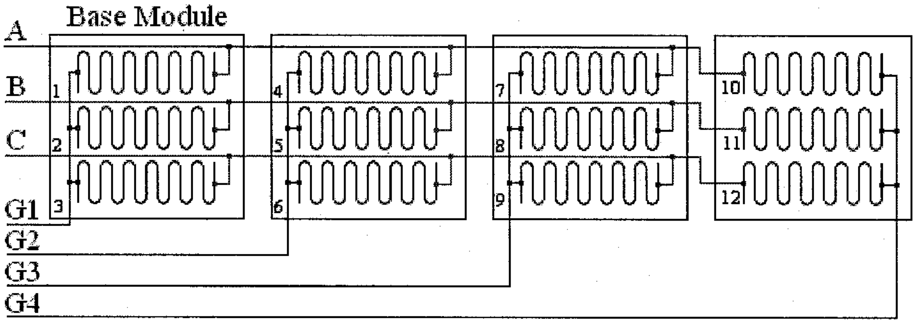

Figure 6-2: SMA actuator matrix

With this arrangement, the total number of wires at the base module is reduced to *n*+2, or in this case 6 wires instead of 13. Using the discontinuous heating principle each SMA element is actuated individually and sequentially by a short current pulse [33]. To heat a particular actuator, the controller enables the lead channel and the ground channel assigned to that actuator. Also, to reduce the heat strain on the wires within the actuator, the actuation order is selected such that each wire is powered sequentially. Table 6-2 indicates the order in which each SMA element is actuated in the $n\tau$ time period.

Table 6-2: SMA element actuation sequence

Time period (*n*)	1	2	3	4	5	6	7	8	9	10	11	12
Ground wire	G1	G2	G3	G4	G1	G2	G3	G4	G1	G2	G3	G4
Lead wire	A	B	C	A	B	C	A	B	C	A	B	C
Actuated SMA	1	5	9	10	2	6	7	11	3	4	8	12

6.3 CIRCUIT DESCRIPTION

The actuation system is composed of seven identical current amplifier units. The lead amplifiers are set in source mode and the ground amplifiers are set in sink mode. The complete diagram of the system is shown in Figure 6-3.

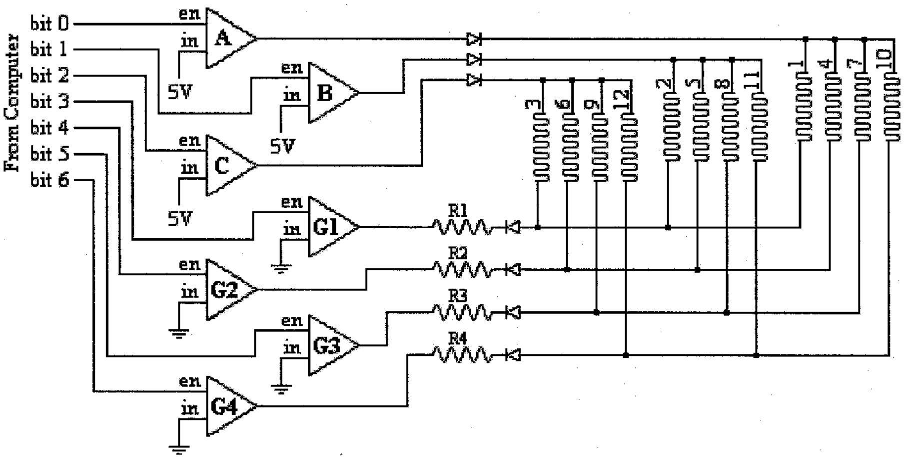

Figure 6-3: Circuit diagram

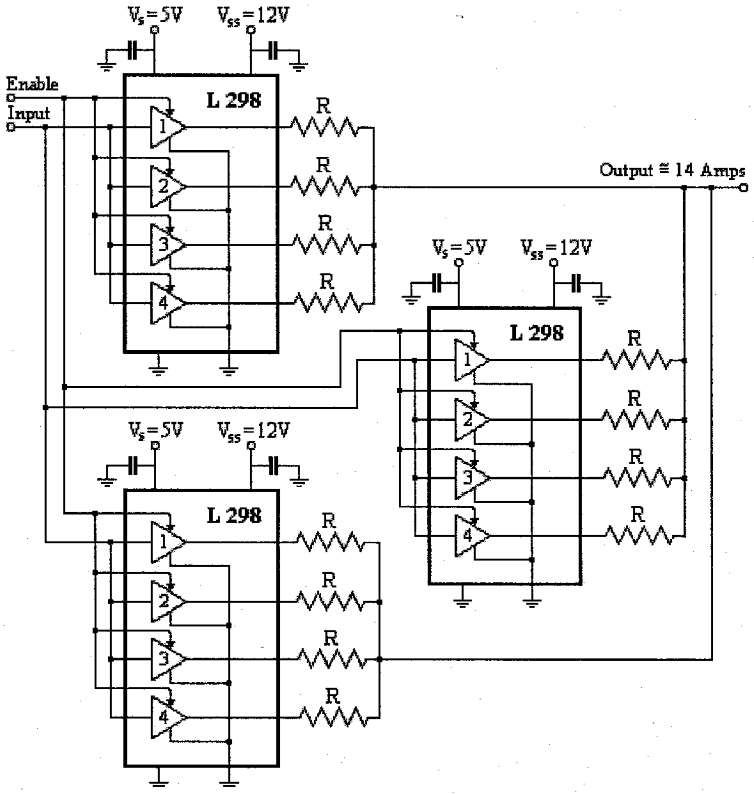

Figure 6-4: Ground amplifier unit block diagram

Each current amplifier unit in Figure 6-3 consists of three L298 dual full bridge drivers. Each driver provides a maximum of 6Amps in source or sink mode. To provide the 13.45Amps required to actuate one SMA elements, three drivers are connected in parallel.

The resistors *R* in Figure 6-4 refer to the current limiting resistors (marked *R1* through *R4*). Resistors were placed at each driver output instead of at the current amplifier unit output to reduce the resistor power requirements and lower the assembly costs. With this arrangement, the wattage in per actuator drops from approximately 12V×14Amps = 168Watts to 12V×1.2Amps = 14Watts.

The L298 exhibits a very high saturation voltage when operating at low voltages and high currents. This voltage reduces the output capabilities of the device. The saturation voltage was determined experimentally to be approximately 4.25Volts for a source voltage of 12.15Volts and an output current of 1.2Amps/channel (see Appendix N). The computed value for the current limiter resistors *R* of each driver bank are given in Appendix O. Figure 6-5 illustrates the actual set-up.

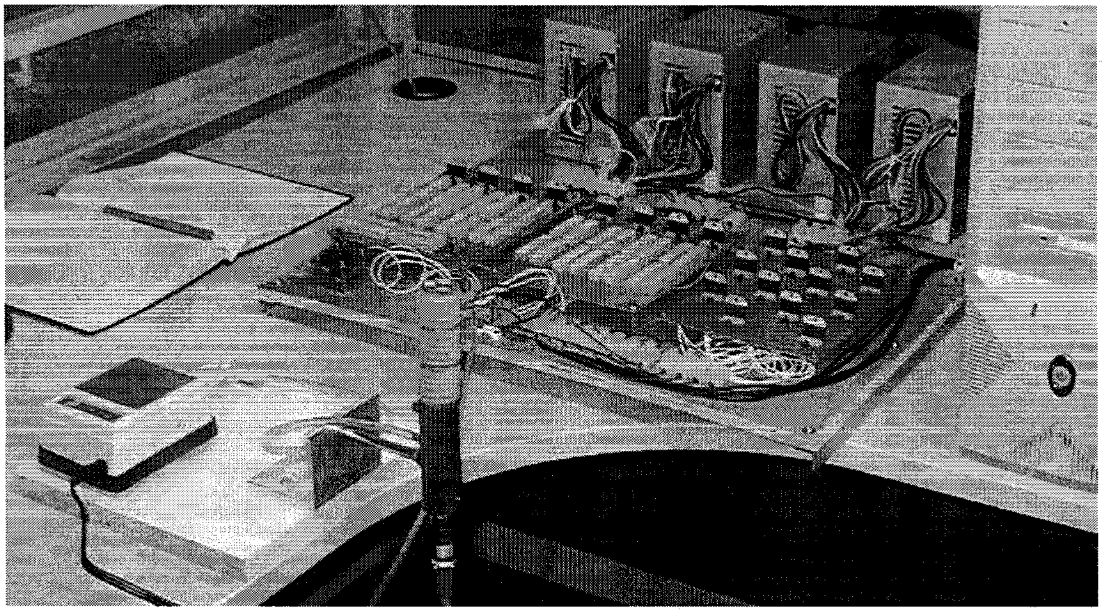

Figure 6-5: Experimental set-up

Chapter 7:
Fabrication

7.1 SMA ACTUATOR CONSTRUCTION

All actuators were fabricated using a 70μm Nitinol sheet supplied by Johnson-Matthey. Thin strips 5.9mm and 7.0mm wide were cut using a shear press. Figure 7-1(a) shows the SMA strip before the heat treatment. Its length is based on the maximum length of the raw SMA sheet such that several actuators could be produced in each batch. The strip was then folded repeatedly over stainless steel panels of thicknesses between 0.72 and 1.44mm as seen in (b). The strip and metal panels were stacked in the jig shown in (c) and clamped down with a u-bolt to maintain the desired shape during the heat treatment. Several actuator profiles were constructed to determine the best shape parameter configurations. These profiles included variations on flat section length, circular section radius, strip width, and heat-treatment temperature.

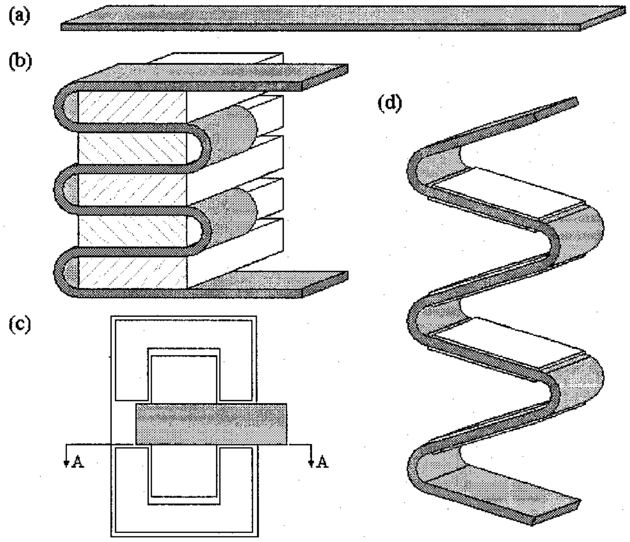

Figure 7-1: Fabrication process flow of the SMA actuator: (a) strip cut to length; (b) cross-section A-A view of forming process; (c) SMA actuator in heat treatment jig; (d) composite actuator

Following the heat treatment, the SMA strip was cut according to the prescribed actuator length. Aluminium films were then glued on both sides of the actuator's flat sections as seen in (d). Silver conducting epoxy was used to reduce the resistivity. A photograph of the heat-treatment jig and several actuator profiles are shown in Figure 7-2.

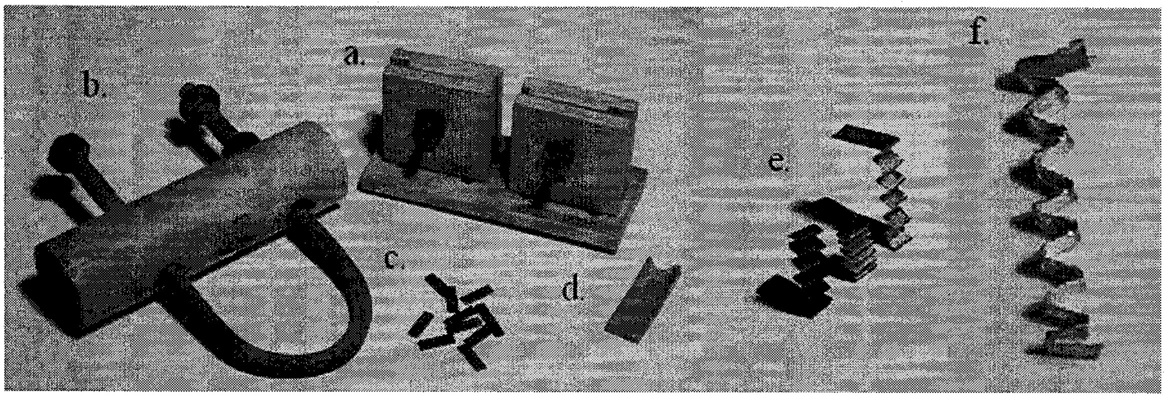

Figure 7-2: Heat-treatment jig and prototype actuator

Based on the tensile test results, the final prototype actuator seen in Figure 7-2(f) has a bend radius of 0.72mm, a width of 7.0mm and a flat section length of 3mm. To obtain the necessary manipulator deflection, the actuator was composed of 13 circular sections.

7.2 BELLOWS CONSTRUCTION

The bellows was designed to produce large displacements in the direction of motion. To limit the motion resistance, the outer shell was shaped in the form of a miniature bellows. The bellows is made up of a two-part rubber compound and was formed using a vacuum degassing moulding process. ReoFlex20 liquid urethane rubber manufactured by Smooth-On Products was used. It has a shore-A hardness of 20 and an elongation of 1000% at break. The cross-section of the bellows design is shown in Figure 7-3.

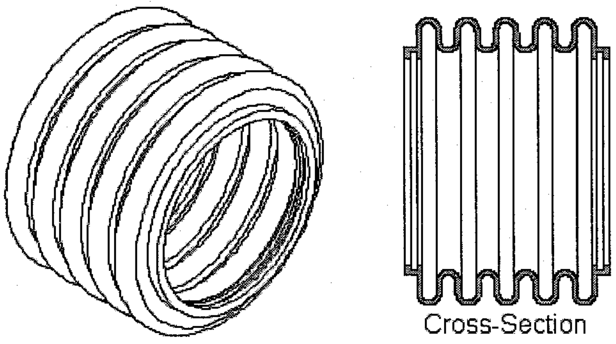

Figure 7-3: Outer shell design

The rubber mixture is poured into the wax moulds and insert shown in Figure 7-4, degassed to remove air bubbles and cured for 24 hours at room temperature. The inner mould was machined from a PVC stock rod and the outer moulds were cast in paraffin wax (using a nylon mould slightly larger than the inner mould).

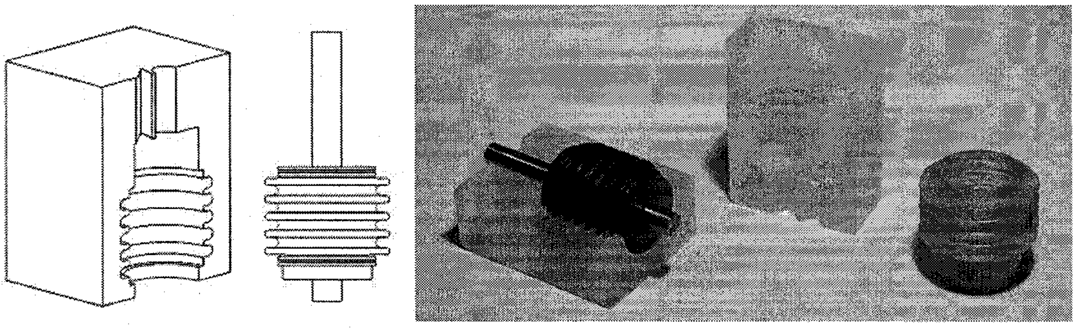

Figure 7-4: Conceptual and actual inner and outer moulds

As seen in Figure 7-5 the bellows could extend to 37mm at the approximate pressure of 22kPa and could compress to 15mm once the pressure was removed. The ventilating tube shown in Figure 3-7 was not fabricated due to time constraints and assembly issues.

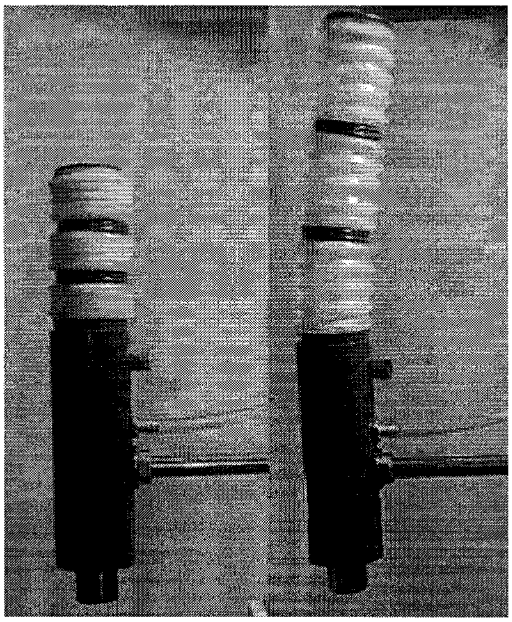

Figure 7-5: Bellows tests

7.3 PROTOTYPE MANIPULATOR ASSEMBLY

The manipulator structure is composed of repeating modules, each containing three actuators, a rubber bellows, wiring and a support plate or vertebra. The vertebrae are composed of a single sided copper clad fibreglass disk 1/64" thick and a PVC ring as shown in Figure 7-6a.

It was found that the 28-gauge magnet wire could not support the discontinuous heating current therefore it was replaced by 24-gauge magnet wire. Due to the high stiffness of the wire, it had to be coiled to the proper shape prior to assembly. Figure 7-6 (a) and (b) shows the addition of lead wires A, B and C followed by the ground wire G3. The actuators were then fastened to the vertebrae using conductive epoxy. In the final stage, the bellows were inserted and fixed in place using clear elastic bands and the manipulator was fixed to the base vertebra.

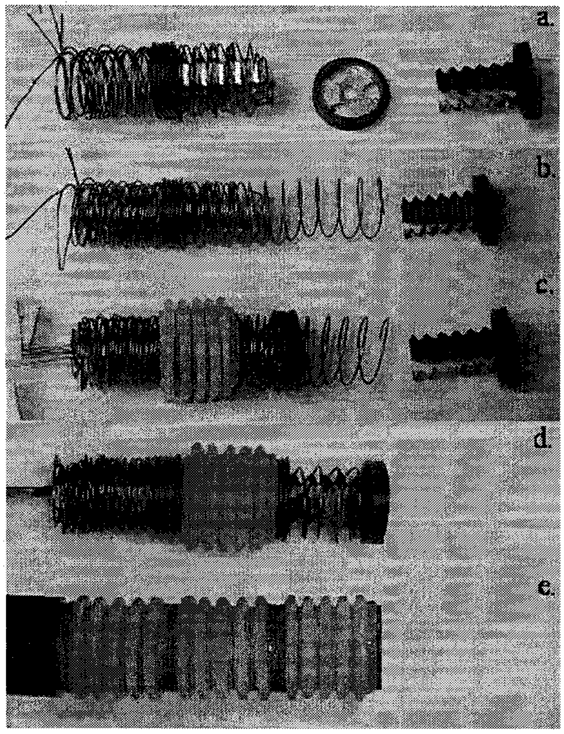

Figure 7-6: Three-stage prototype manipulator assembly

The maximum diameter of the support plate was equal to 24.3mm and the total external diameter was equal to 31mm. The unit module mass varied between 4.8 grams for the end-effector to 9.7 grams for the base module. The actual and estimated mass partitions are given in Table 7-1.

Table 7-1: Unit module mass

Component	Estimated Mass [g]	Actual Mass [g]
Actuators (and epoxy)	0.6	0.7
Support plate (and epoxy)	1.5	1.1 - 1.2
Bellows	1.4	2.9
Wire	1.0	1.0 - 5.0
Total	4.5	5.7 - 9.8

Due to connectivity problems incurred in the manipulator of Figure 7-6, a single module prototype was also fabricated. To reduce the resistance and heat production in the area of the connections, the second prototype was assembled using two fibreglass disks per vertebra. The actuator tabs (connecting surfaces on the actuators) were sandwiched between the two support plates with the copper sides inward and fixed with conductive epoxy. Figure 7-7 illustrates the internal components of the second prototype with one activated actuator.

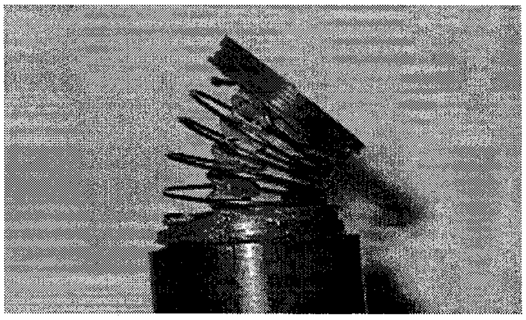

Figure 7-7: Single-stage prototype

Chapter 8:
Experimental Results

8.1 SMA MATERIAL PROPERTIES

The raw SMA material properties were obtained from a tensile test on a sample strip with a square cross-section of 6.98×0.07mm. Figure 8-1 shows the average results of tensile tests performed on an SMA sample in both the austenite and martensite state (tests results given in Appendix Q). The sample was subjected to 3% strains at 21°C and 1.5% strains at 70°C.

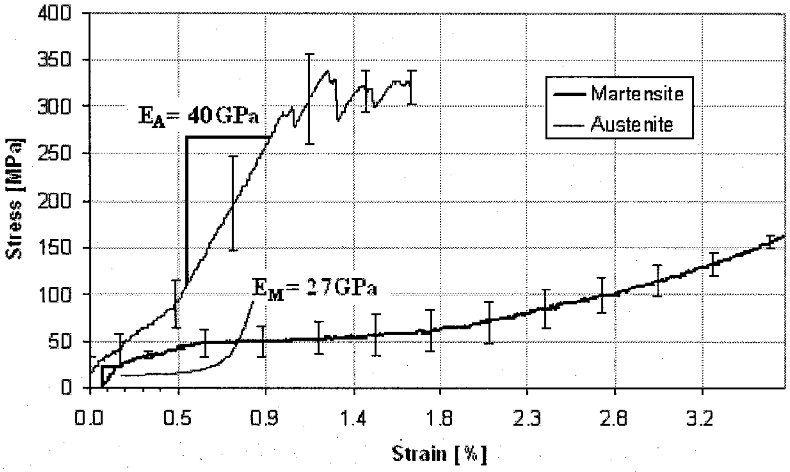

Figure 8-1: SMA engineering stress-strain curves

From the engineering stress-strain curve, the approximate austenite and martensite elastic moduli are computed as 40 and 27GPa respectively. According to the manufacturer, Young's modulus for the austenite phase is equal to 83GPa and between 28 and 43GPa for martensite. The large difference between the measured and specified values for the austenite elastic modulus can be attributed to both the lack of an extensometer during the tensile tests and the inaccuracies in the load cell readings (as seen by the large error bars in Figure 8-1). The variability of the data can be attributed to the 100kN load cell used in the experiment.

8.2 ACTUATOR EXPERIMENTAL RESULTS

8.2.1 Steady-State Continuous and Discontinuous Heating Current

The continuous current required to maintain the actuator's temperature above the austenite finish temperature was determined using an untreated sample of SMA material and a 10kΩ thermistor. The heating current was obtained by measuring the voltage across a current limiting resistance. For a 5.9×0.07×60mm sample strip, the steady-state material temperature was obtained for six continuous current levels and the results are given in Table 8-1.

Table 8-1: Continuous heating currents and temperatures

Current Limiter [Ω]	Measured Voltage [V]	Estimated Current [Amp]	Thermistor Resistance [kΩ]	Temperature [°C]
0	0	0	10.4	22
2.3	4.13	1.80	5.5	41
2.0	3.97	1.98	5.0	44
1.8	3.68	2.04	3.9	52
1.5	3.59	2.39	3.2	58
1.25	3.41	2.73	2.3	69
1.0	2.98	2.98	1.4	85

The SMA austenite start and finish temperatures are given by the manufacturer as 45°C and 95°C respectively. To maintain the actuator temperature within this range requires a constant current between approximately 2.0 and 3.2 Amps. According to (6-2), the current required to maintain the actuator at 65°C in 22°C ambient air is equal to 3.3Amps or approximately 18% lower than the value computed in Chapter 6. The difference between the actual and predicted temperatures is illustrated in Figure 8-2 for heating currents up to 3Amps. To maintain the actuator at 65°C using the principle of discontinuous heating, (6-5) predicted a current level of approximately 14Amps for a system composed of twelve actuators.

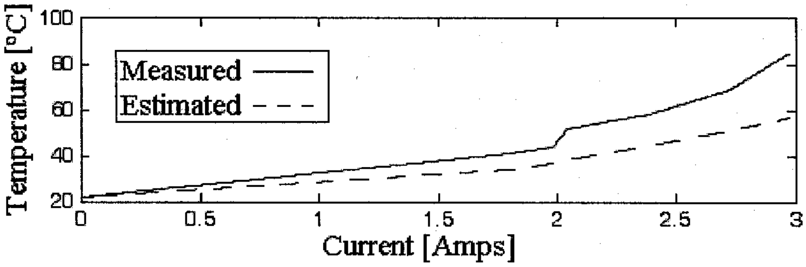

Figure 8-2: Continuous heating current

In the actual test, two actuators of 5.9 and 7.0mm widths were tested using the manipulator driver circuit. The actuators were connected in series with the appropriate length of magnet wire to simulate the actual set-up. The circuit's output current was estimated by measuring the resistance and voltage across the actuator-wire stage when operating in continuous mode (the output current is equal for both continuous and discontinuous cases). The measured output current was at least 8Amps (precise measurements could not be made due to the lack of adequate testing equipment).

At this current level, a thermistor attached to the base of a 5.9mm wide actuator registered a resistance between 1.4 and 1.6kΩ resulting in a temperature of approximately 85°C. The thermistor attached to a 7.0mm wide actuator registered a steady-state resistance between 1.5 and 1.9kΩ resulting in a temperature range of 75 to 85°C. Both actuators reached temperatures above the 45°C austenite start temperature of the SMA. However, the temperature readings may have been under-estimated due to the poor contact between the thermistor and the sample actuators.

8.2.2 Heat-Treatment Temperature Effects

An analysis on thermomechanical treatment of SMA springs found that the recovery rate of SMA springs decreased dramatically for heat-treatment temperatures below 425°C and decreases slightly for temperatures above 500°C [51]. To determine the heat-treatment temperature effects on the proposed actuator, three identical actuators were formed at 400, 500 and 600°C for 1h. Each actuator had a post-heat-treatment memorized length of 11mm. The actuators were then subjected to 3 to 5 tensile tests in the martensite state and 3 to 4 tensile tests in the austenite state. Following the tests, the memorized actuator lengths had increased to 24.0, 13.5 and 16.8mm respectively. Since the extension percentage is based on the memorized length, longer lengths resulted in lower maximum extensions. This effect can be seen in Figure 8-3.

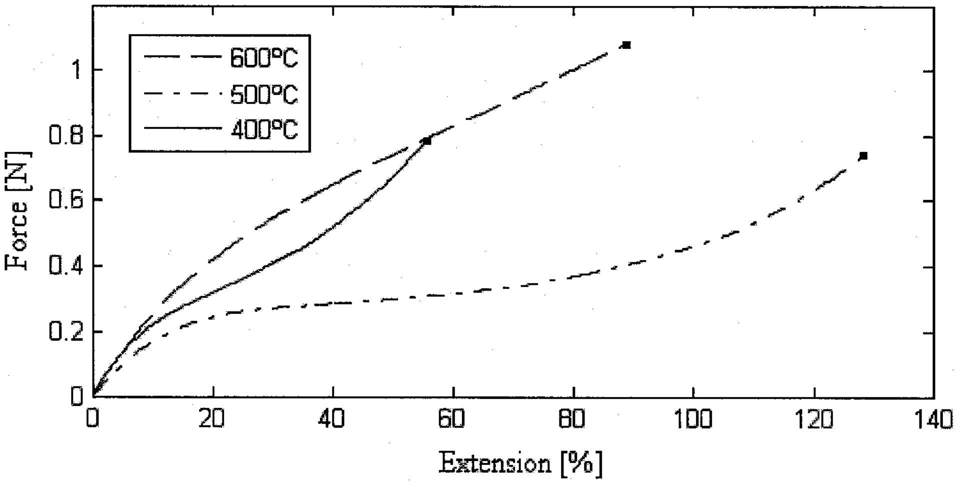

Figure 8-3: Maximum extension in the martensite state, R = 0.92m

The austenite force extension plot of Figure 8-4 demonstrates that the stiffness of the specimen treated at 600°C was slightly lower than the specimen treated at 500°C.

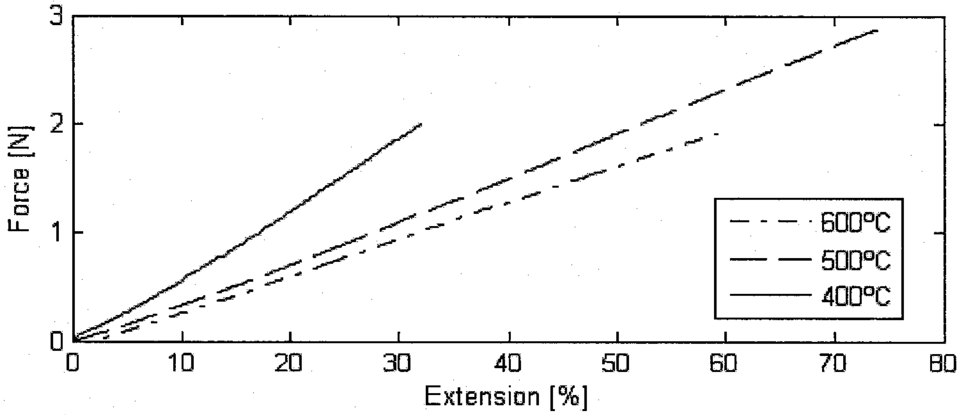

Figure 8-4: Output force in austenite state

Again, the higher stiffness exhibited by the actuator heat-treated at 400°C was a result of the permanent strain induced in the first few cycles. Extension percentages based on the initial actuator lengths would have shown that the specimen treated at 400°C had a lower stiffness. These tests demonstrated that the most favourable heat-treatment temperature was around 500°C, which is in agreement with the manufacturer's recommendations.

8.2.3 Actuator Frequency Response

Frequency tests were performed on each actuator profile using the layout shown in Figure 8-5. The actuators were attached to a weight and holder of 62.3 grams and allowed to move freely in the vertical direction. The heating current was provided by a PC power source and evaluated at 2.9Amps continuous ($V_{resistor} = 2.75V$, $R = 0.95\Omega$). At this level the actuators were expected to reach the 80°C level.

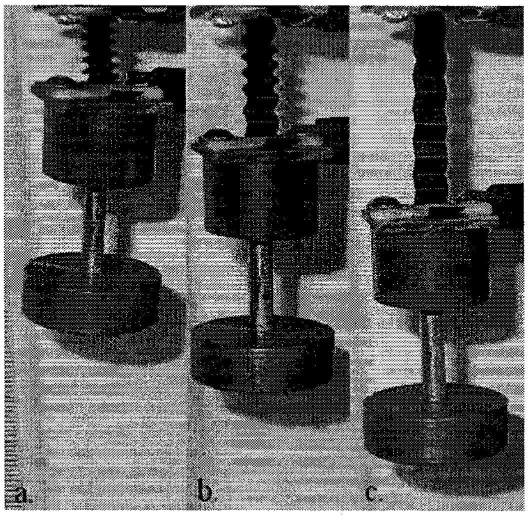

Figure 8-5: Frequency test layout

The results were divided between the two width sizes fabricated. Figure 8-6 consists of select 5.9mm wide actuators with various profiles and Figure 8-7 consists of several 7.0mm wide actuators with identical profiles. The test results shown in Figure 8-7 were used to determine the effects of the composite metal plating and the manufacturing quality on the frequency response. Except for the specimen treated at 600°C, all the specimens exhibited cooling times around 50 seconds, with heating times varying between 5 and 10 seconds.

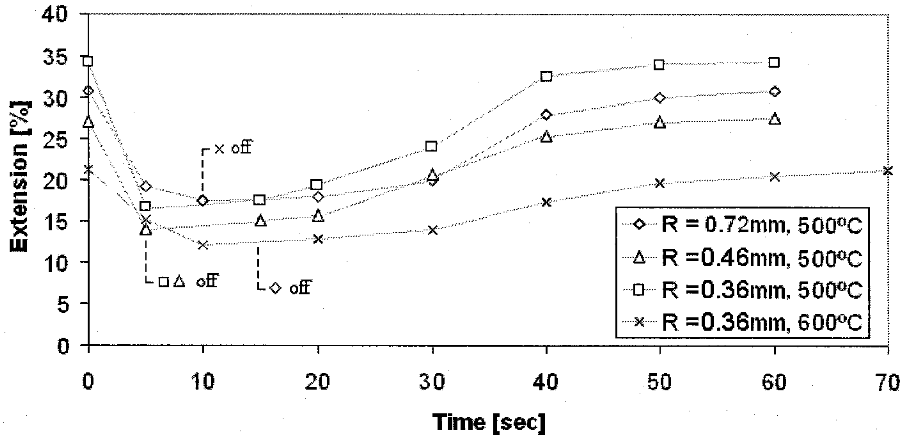

Figure 8-6: Frequency response of select 5.9mm wide actuators

Slightly sharper responses were recorded for profiles with small radii and for specimens heat-treated at 500°. In the case of the 7.0mm wide actuators, cooling times ranged between 50 and 85 seconds and the heating times between 10 and 20 seconds as illustrated in Figure 8-7. The sharpest response was observed in the bare specimen, which was not equipped with the aluminium plating. The randomly selected prototype actuators showed, on average, slightly slower responses than the bare specimen but much quicker responses than the composite specimen.

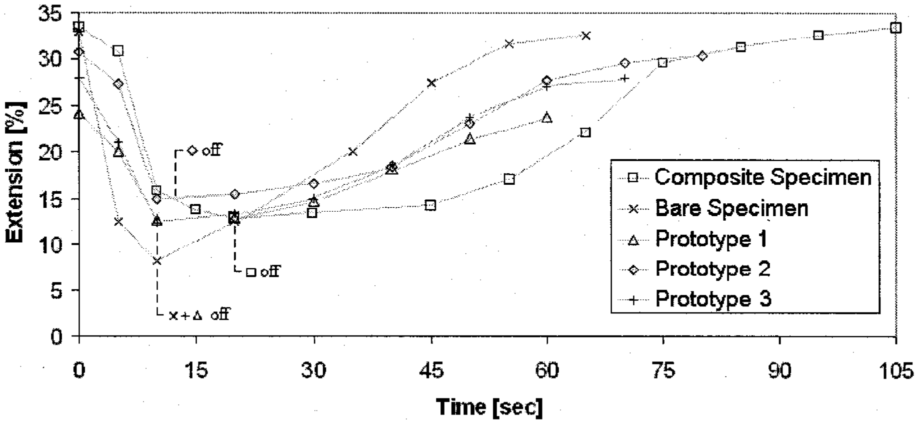

Figure 8-7: Frequency response of the prototype actuators

The slower response may have been caused by a gradual shape memory loss due to cycling or manufacturing defects (all prototype specimens were fabricated according to the composite specimen profile). In general the frequency response for the prototype actuators ranged between 0.014 to 0.017Hz

8.2.4 Training Strain

As mentioned in the previous section, permanent strains are generated in the first few cycles following the heat-treatment, resulting in an increase in the actuator memorized length and a reduction of the maximum actuator extension. The magnitude of this effect is given in Table 8-2.

Table 8-2: Actuator memorized length before and after training

Profile Radius L = 1.5mm W = 5.9mm	Heat-Treatment Temperature [°C]	Post heat-treatment length [mm]	Trained Length [mm]	Increase [%]
0.36mm	400	8.8	24.0	173
0.72mm	500	13.66	16.5	20.8
0.46mm		10.96	13.5	23.2
0.36mm		8.76	12.0	37.0
0.72mm	600	13.7	17.0	24
0.46mm		11.0	16.8	53
0.36mm		8.8	13.2	50

8.2.5 Shape Parameter Effects

Actuators with different lengths, widths and radii were constructed to determine the actual profile effects on the output force. Presented below are the results obtained from all the relevant tensile tests (the output characteristics for all the actuator profiles can be found in Appendix P). It should be noted that, except for the actuator profile selected for the manipulator construction, only a single specimen was fabricated for each profile and the results represent the average data of 3 to 6 tensile tests in both the austenite and martensite states. The number of tests performed on each profile was based on the variability of the data.

The first round of tests determined the effect of the straight section length on actuator response. Two actuators, of equal radius and width, with straight section lengths of 1.5 and 2mm were tested and the results are given in Figure 8-8. The two lower curves represent the martensite responses and the two upper curves represent the austenite responses.

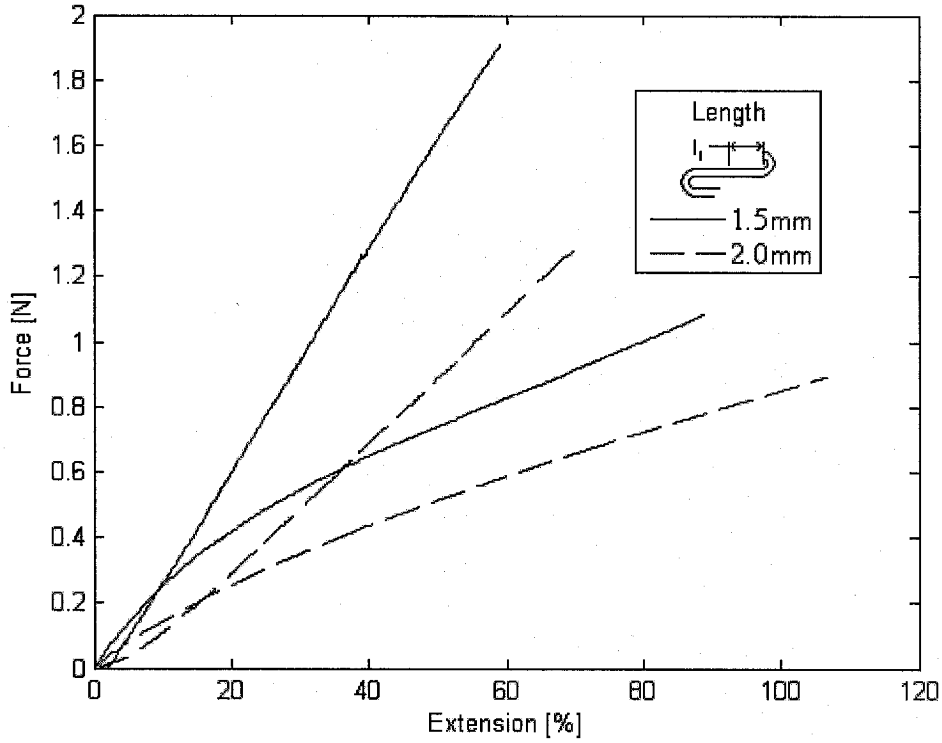

Figure 8-8: Output force of actuator with varying lengths heat-treated at 600°C

For a 20° change in circular section angle, the actuator with a straight length of 1.5mm produced an extension of 55% whereas the actuator with a length of 2.0mm produced an extension of 75%. In the martensite state, $F_{1.5mm\ (@55\%)} = 0.80N$ and $F_{2.0mm\ (@75\%)} = 0.73N$ resulting in a force ratio of 1:1.10. In the austenite state, $F_{1.5mm\ (@55\%)} = 1.8N$ and $F_{2.0mm\ (@75\%)} = 1.4N$ resulting in a force ratio of around 1:1.29. As expected the output force diminishes as the section length is increased. To satisfy the space restrictions and force requirements of the manipulator, all subsequent tests were conducted on actuators with a 1.5mm straight section length.

The second round of tests evaluated the performance of actuators with two different widths. Each actuator had a radius of 0.36, a straight section length of 1.5mm, and widths of 5.9 and 7.0mm.

The third round of tests evaluated the performance of actuators with various circular section radii. As with the previous tests, the two other shape parameters remained constant (w = 5.9mm and l_l = 1.5mm). The results of both comparisons are illustrated in Figures 8-9 and 8-10.

As expected, the actuator with the lowest radius could provide the largest extensions in the martensite state. From the figure, the actuator stiffness in the austenite state is approximately equal for the both 0.46 and 0.72mm radii but decreases dramatically for the R = 0.36mm specimen. Again, these discrepancies may be linked to the stress induced permanent strain; but, as it will be discussed in the following section, the large variation in actuator stiffness may also be linked to fabrication defects.

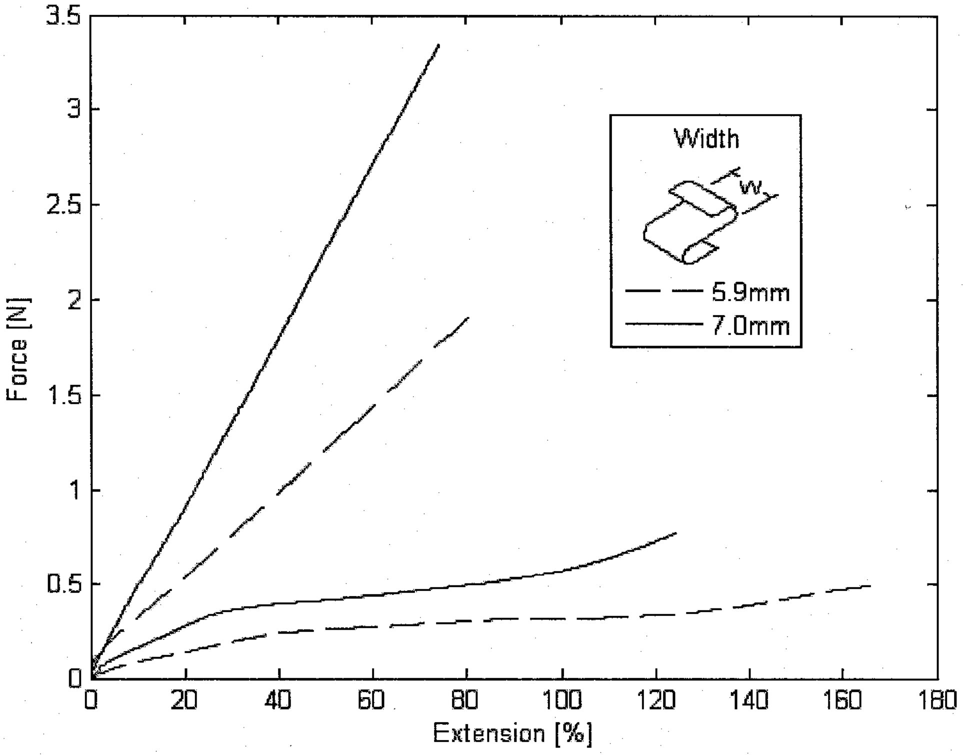

Figure 8-9: Output force of actuator with varying width heat-treated at 500°C

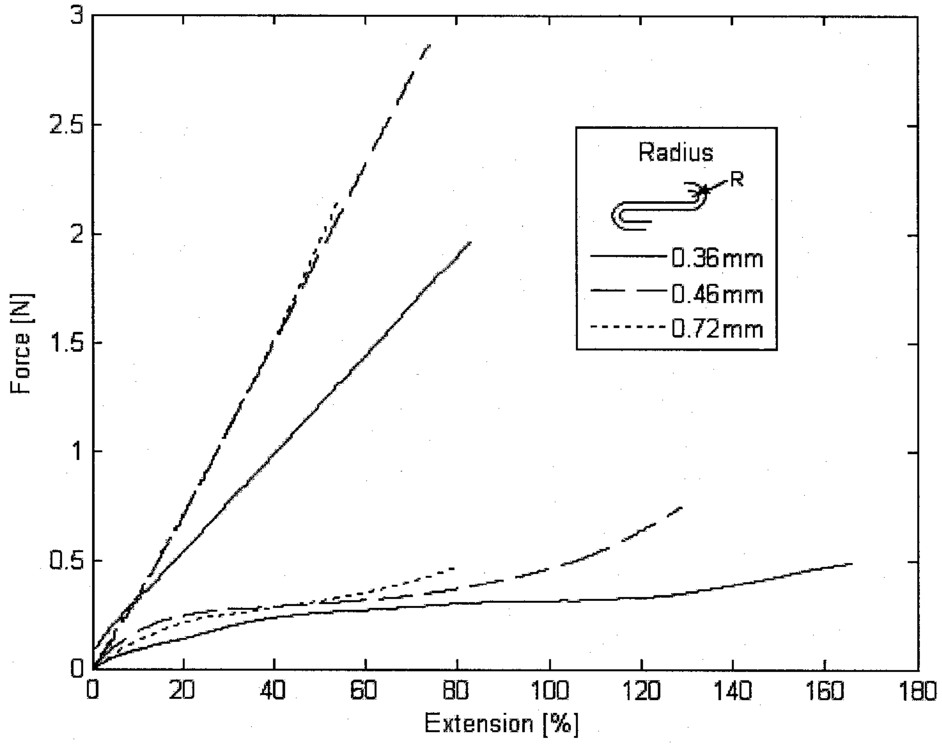

Figure 8-10: Output force of actuator with varying radii heat-treated at 500°C

A final comparison was done to determine the effects of the composite aluminium plating on the actuator performance. The actuator profiles used in the comparison have a radius of 0.36mm, a straight length of 1.5mm and a width of 7mm. As it can be seen in Figure 8-11, the two specimens display similar responses for both the austenite and martensite phases.

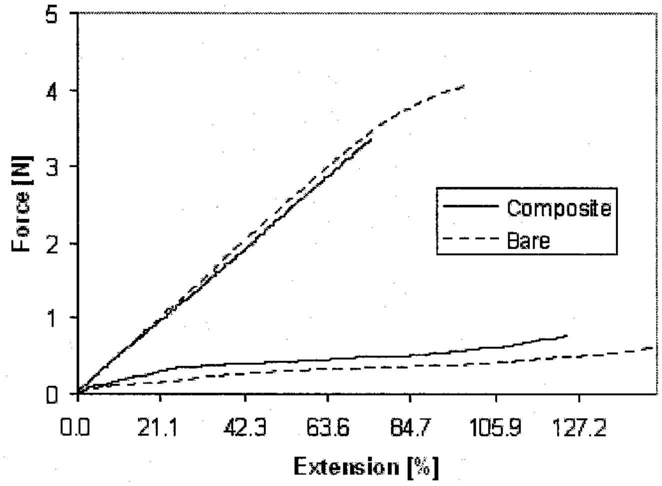

Figure 8-11: Composite actuator performance

8.2.6 Prototype Actuator Response

Since the goal was to design a high strain manipulator, the actuator capable of producing the largest extensions in the martensite state was chosen. According to Figure 8-10, the extension capacity of the actuator is primarily a function of the radius, with the smallest radius producing the largest deflections. For this reason the actuator with a radius of curvature of 0.36mm was chosen in the fabrication of the prototype manipulator. To reach the 3.8N force computed in Chapter 5, the width and straight section length of the actuator were set at 7.0mm and 1.5mm respectively and the output force characteristic for this profile is shown in Figure 8-12.

According these results, the actuator can achieve a 3.8N force at an extension of approximately 80% in the austenite state and stretches to around 140% in the martensite state. At this extension level the stretched actuator produces a force slightly under 1N. Since each module is equipped with three actuators, the total extension force is approximately 3N. This is below the computed pressure force of 5.4N and should be sufficient to extend the actuators to this point. Upon heating, the actuator contracts from the 140% level to around 80%. For a trained memorized length of 12mm, the actuator is capable of producing an 8mm stroke.

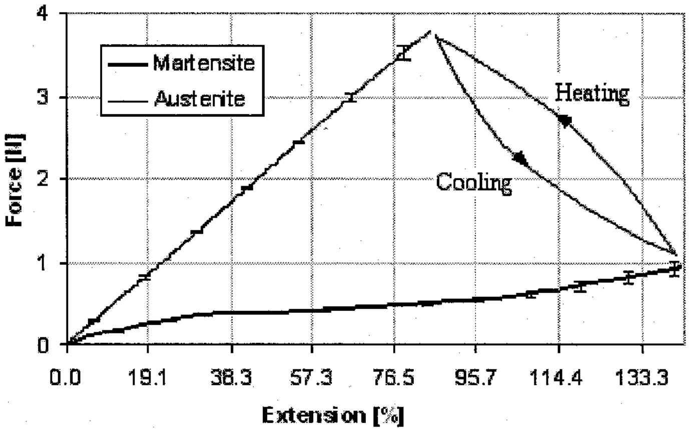

Figure 8-12: Prototype actuator response

8.3 MANIPULATOR EXPERIMENTAL RESULTS

In the first prototype, connectivity issues immediately rendered two of the three sections inoperable (the factors contributing to the bond failures will be discussed in the following section). Only the end-effector module was able to produce a small displacement for a short period of time. The activation of a single actuator (number 8) was captured in Figure 8-13.

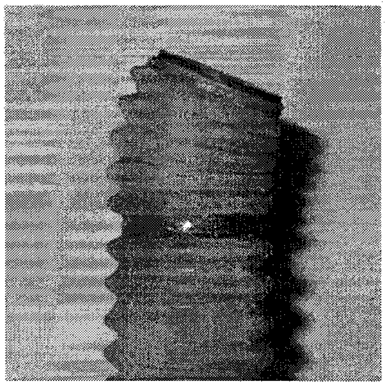

Figure 8-13: First prototype test

The internal pressure was set at 22kPa and the resulting deflection is approximately 20°. The connection was severed at around the third second of the heating cycle, which leads to believe that the actuator did not complete the phase transformation and could possibly generate larger displacements. In all other cases, connection failures occurred before the actuators could reach the austenite phase. All the bond failures occurred at the nodes connecting the actuators to the lead wires (*A*, *B* and *C*).

In the second prototype, the improved connections allowed for several complete cycles. Shown in Figure 8-14 are the images of the: a) pressurized un-actuated module, b) single activated actuator and, c) dual activated actuators. The unit module was unable to produce the fourth non-redundant configuration consisting of the activation of all three actuators since the bond between lead wire *B* and the second actuator failed after the 2nd cycle.

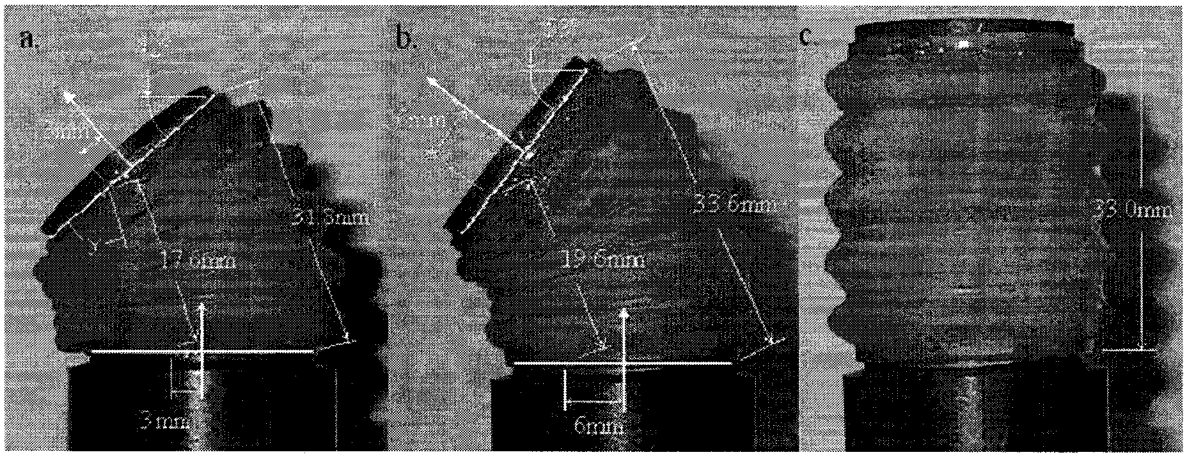

Figure 8-14: Second prototype tests

At the estimated pressure of 22kPa the average maximum extension produced in Figure 8-14c was equal to 33mm. Based on Figure 8-14b, the inclination angle produced by a single actuator was approximately 53° and the coordinates of the end-effector were y_1 = 9.9mm and z_1 = 23.0mm. In the case of the dual activated actuators of Figure 8-14a, the inclination angle was estimated at 42° with end-effector coordinates equal to y_2 = 8.8mm and z_2 = 20.0mm.

Video recordings of the second prototype tests were taken for both single and dual activated actuators. In the case of the single actuator, five recording were taken of the complete cycle. Table 8-3 gives the approximate heating and cooling times for the five cases.

Table 8-3: Frequency response times for a single actuator

Test	Heating time [sec]	Cooling time [sec]
1	3	22
2	2.5	18.5
3	2.5	17.5
4	2	19
5	2	20

The average heating and cooling times are 2.5 and 19.4 seconds and a frequency response of 0.046Hz. Only one recording was taken of the dual activated actuator configuration. From the video, the heating time was estimated at 5 seconds and the cooling time at 20 seconds resulting in a slightly lower module frequency response of

0.04Hz. The connection between actuator number one and lead wire *A* failed after the 6th cycle and the connection between actuator three and lead wire *C* failed after the 17th cycle.

Chapter 9: Analysis

9.1 ACTUATOR PERFORMANCE

Without taking into consideration the permanent strain induced during training, the actuator model proved successful in estimating the output force capabilities of the actuator. Figure 9-1 illustrates the difference between the actual actuator response based on the trained length and the estimated actuator response based on the initial annealed length.

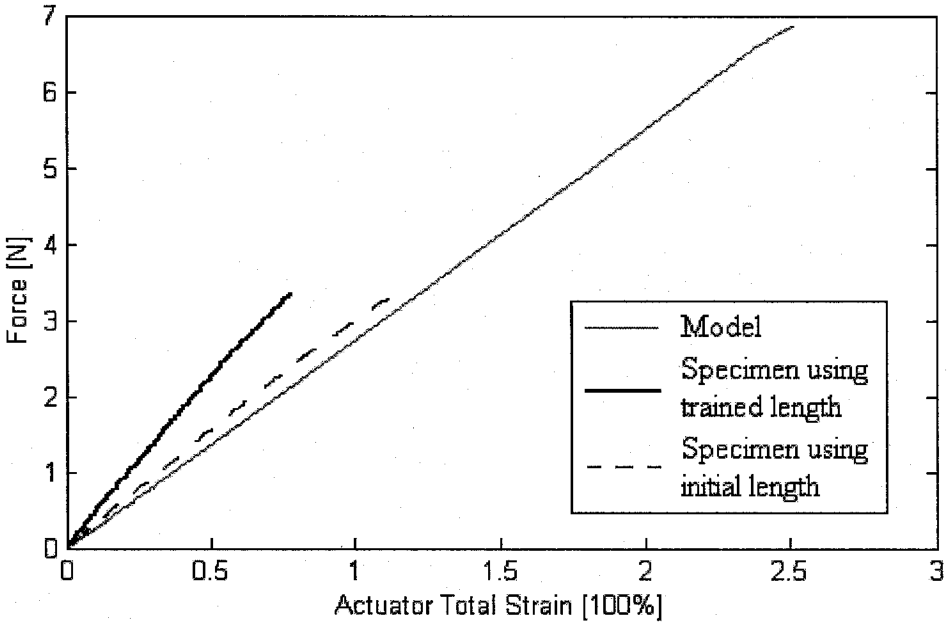

Figure 9-1: Actuator output force in the austenite state

In the case of the actuator response in the martensite state, the output forces were much higher than predicted and the model could not predict the large output force spike shown in Figure 9-2. This effect had been overlooked in the equations and assumptions made to generate the internal strain used by the model. Equation (3-6), used to obtain the strain field across the thickness of the SMA sheet, assumes that the change in angle θ remained small. The theoretical plots generated by the model were based on a $\Delta\theta$ of 90° and in the actual tests, $\Delta\theta$ could have been as high as 70° (based on visual inspection).

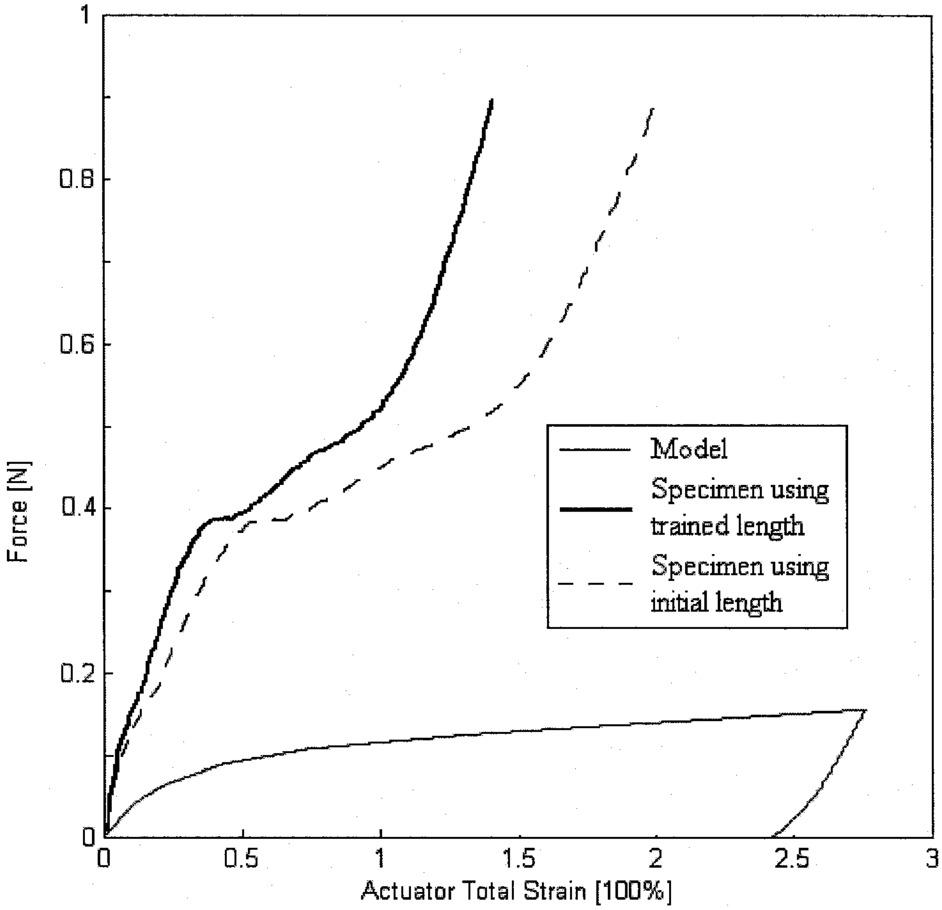

Figure 9-2: Actuator output force in the martensite state

Compared to the output force generated by the model, the actual output force in the plateau region is about four times higher and quickly climbs to around 0.9N at an extension of 140%. The maximum extension undergone by the sample actuator was approximately half that generated by the model. This is mainly due to the degradation of the memorized shape during training. The large discrepancies between the actual and computed martensitic response may also be attributed to the underestimation of the martensite macroscopic stiffness $C_{1,2,3}$ and plastic damping coefficient $\alpha_{1,2,3}$ used in the two-phase constitutive model since these material parameters were not determined experimentally. This limitation was also observed in the straight length comparison tests of Figure 8-8. According to (3-4) and (3-9), an actuator with a straight length of 1.5mm at an extension of 55% should have and output force ratio of 1:1.27 compared to an actuator with a length of 2mm at an extension of 75% (both cases evaluated at $\Delta\theta = 20°$). The actual force ratio was equal to 1:1.29 in the austenite phase and 1:1.10 in the martensite. The results suggest that the actuator model could only predict the effects of straight length variations on actuators in the austenite state.

On the other hand, the model could not accurately predict the effects of width on the actuator response. In the actuator model, the output force was presumed to be proportional to the actuator width. Modifying the response obtained from the 5.9mm wide actuator, according to (3-8), to reflect the increase in width resulted in the dashed curves of Figure 9-3.

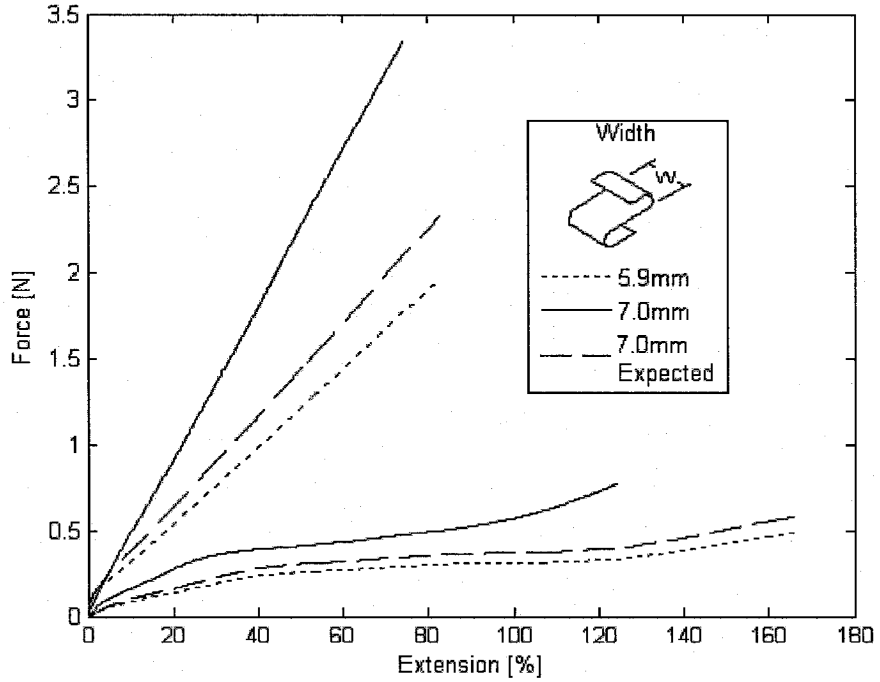

Figure 9-3: Width comparison

The predicted response for the 7.0mm wide actuator (based on the 5.9mm wide response) was lower than the actual response, indicating that the output force is not proportional to the width. Again, the differences in austenite stiffness may have been a result of the induced permanent strain mentioned above.

The addition of metal films on the straight sections of the actuator did not have any noticeable effects on the output force of the actuator. The composite specimen exhibited slightly higher heating and cooling times, which may have been caused by defects introduced in the manufacturing process. The large circle in Figure 9-4a shows an improperly installed metal film. A portion of the film touched the inside of circular section. As a result, the film may have inhibited the actuation of that section. A similar defect was found in the specimen of Figure 9-4b. In this case, a circular section was accidentally covered in conductive epoxy.

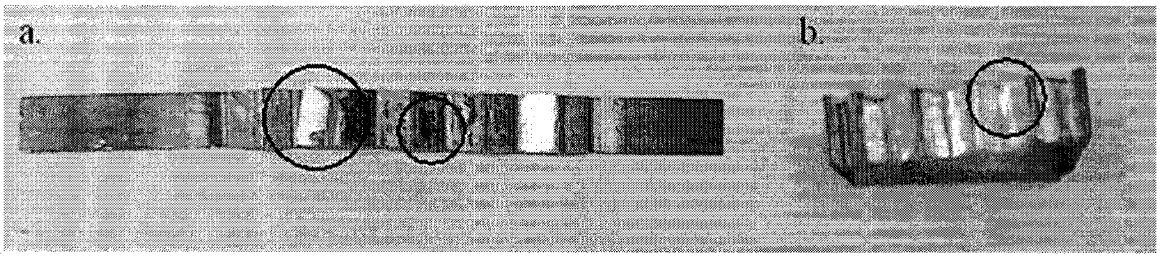

Figure 9-4: Composite actuator fabrication defects

After having removed the metal films from the straight sections, it was found that most of the films were not completely bonded to the SMA. The dark regions highlighted by the small circle in Figure 9-4a indicate areas were the film was improperly bonded to the SMA.

9.2 MANIPULATOR PERFORMANCE

The results obtained from the second prototype tests demonstrated that the unit module capabilities were similar to those generated by the manipulator and actuator models. The unit module performance was obtained by measuring the steady-state positions and orientations of the three different states generated in the experiment.

As predicted by the model, the angles γ between the actuators and the support plates were approximately equal for each projected length. The unit module model illustrated in Figure 5-3 assumed that the unit module length, L_p, on the un-actuated side remained constant (and equal to the length of case (c) for all states excluding the fully actuated state). Based on the measurements of Figure 8-14 the length of the un-actuated side decreased by 3.6% in case (a) and increased by 1.9% in case (b).

According to Figure 8-12, the prototype actuator stiffness in the austenite state was approximately 0.38N/mm with a memorized length of 12mm. With an internal pressure of 22kPa, (5-3) through (5-60 predict an actuator force of 4.5N, and actuator lengths of 23.5mm for case (b). This should produce an inclination of 35° as opposed to the 53° inclination observed in Figure 8-14b. The higher angle produced in the case (b) may have been a result of a larger actual radial distance R_1 in (5-2) to (5-4) (distance between the actuator tab and the manipulator centre axis). In the assembly process, the first circular section on the actuator was directed outwards, pushing the point of contact between the actuator and the vertebra closer to the edge of the support disks and increasing R_1 from 6mm to around 8mm.

In the dual activated case of Figure 8-14a, the module should have produced an inclination of 65° but the actual inclination was 42°. A sudden decrease in the un-actuated length and module inclination was observed in the video recording towards the end of the heating cycle. This effect may be explained by the actuator's attempt to straiten itself out. The actuator centreline is offset by an angle of π-γ during actuation. A realignment of the actuators in the final heating stage would generate a moment in the opposite direction, leading to a slight compression of the un-actuated side and a reduction of the module angle.

During fabrication it was found that the 24-gauge wire coiled with a 20mm diameter and with 6 complete loops exhibited a non-negligible resistance to motion in both the axial and radial directions and that this effect significantly influenced the performance of the unit-modules containing more than one wire. Figure 9-5 illustrates the difference in maximum extension between the bellows structure in (a-b) and the complete manipulator in (c-d).

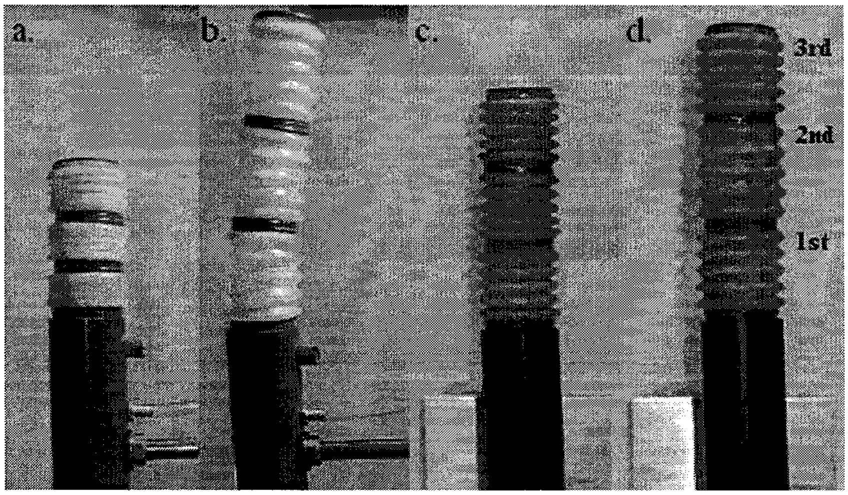

Figure 9-5: Manipulator extension under 22kPa internal pressure

The first module in Figure 9-5d contained three actuators and 5 coiled wires and extended to approximately 29mm at a pressure of 22kPa; a 12% length reduction compared to the second prototype at the same pressure.

The effects directly linked to the additional wires could be observed in the second module of Figure 9-5d. It contained four coiled wires and no actuators and could extend to 34mm at 22kPa, a 7% reduction compared to the empty bellows of Figure 9-5b. The poor connections between the actuators and the vertebra could not withstand the applied stress, current and heat. No actuation data could be obtained on the first and second unit modules. Several factors may have contributed to the connection failures. First, high temperatures in the vicinity of the connections between the support plates and the actuators may have lead to a breakdown of the adhesive bonds. The maximum operating temperature of the conductive epoxy is 90°C whereas the austenite finish temperature of the SMA material is 95°C. The temperature increase at the nodes could be linked to a combination of the high resistivity of the epoxy/copper layer on the vertebra, the poor quality of the bonds between the actuator and the vertebra, and the presence of an oxidized film on the actuator surface. The raw SMA sheet was flat grey in colour.

Following the heat-treatment, the actuator colour changed to flat gold when treated at 400°C, to reflective gold and purple when treated at 500°C, and to dark grey when treated at 600°C.

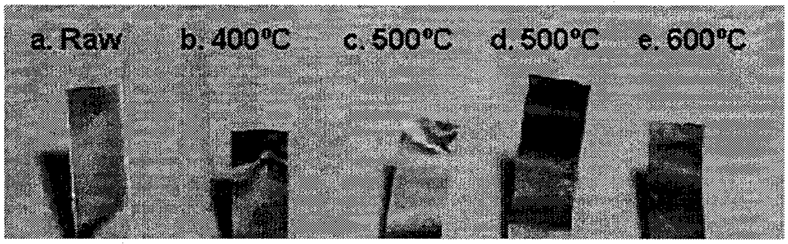

Figure 9-6: SMA Surface colour for various heat-treatment temperatures

Connection failures may also have been caused by short circuits on the lead side of the vertebra. The highlighted area in Figure 9-7a shows a thin layer of conducting epoxy between two lead connections. On the vertebra of Figure 9-7b, an epoxy bridge between the lead connections A and B caused a short circuit and charred the surrounding fibreglass. The sudden surge in current may have heated the connection beyond the operating point of the epoxy.

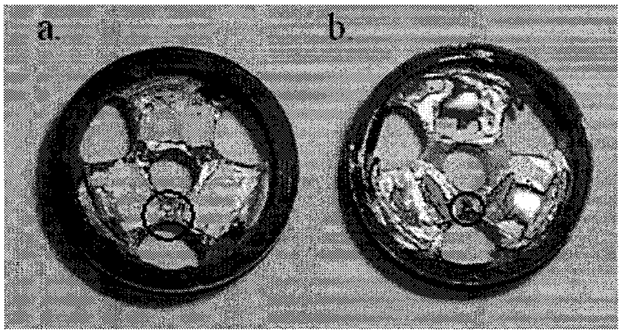

Figure 9-7: Dismantled vertebrae inspection

On average, the frequency response of the second prototype was three times higher than individual actuators in still air. The amplifier circuit and controller software was designed to accommodate a four-stage manipulator containing twelve actuators and could heat each actuator in approximately 2.5 seconds. Based on resistance and voltage measurement, the amplifier was capable of generating 9Amp pulses, which would, according to (6-5), amount to a continuous current of 2.6Amps. According to Table 8-1, this should lead to steady-state temperature of around 65°C. On the other hand, the frequency tests on individual actuators were performed at 2.9Amps, or 85°C, and resulted in a heating time above 10 seconds. This discrepancy may have been due to two factors: first, the actual output current of the amplifier circuit may have been higher than originally observed, and second, the high currents associated with the discontinuous heating method may have lead to quicker responses.

However, the airflow provided by the pump was the major contributor in the improvement of the frequency response. The airflow effectively reduced the cooling cycle from approximately 50 to 20 seconds. It is probable that even higher frequencies could be achieved by increasing the airflow speed (since the pump was operating at maximum capacity). It is to be noted that the pulsating action of the pump may also have promoted a more rapid phase transformation into twinned martensite; however, the full extent of this effect has yet to be determined.

The goal of this study was to evaluate the feasibility of the pressurized manipulator design. The optimum actuator profile was determined based on the tensile test results. However, several non-essential factors have been overlooked and remain to be investigated. These include the effect of bellows geometry, thickness and material type, the effects of the ventilating tube, and the effects of the electrical wiring on the manipulator stiffness. The performance of a complete multi-stage manipulator also remains to be investigated.

Chapter 10:
Conclusions & Recommendations

10.1 CONCLUSIONS

The goal of this research was to develop a compliant pressurized hyper-redundant manipulator driven by SMA actuators. Although manufacturing issues prevented the validation of the hyper-redundant manipulator, the unit module constituting the base element of the design was successfully modeled, fabricated and evaluated. A single unit module prototype driven by three SMA actuators demonstrated that the proposed design could achieve large displacements and rotations of over 50 degrees. The two-phase constitutive model could not predict the stress induced permanent strain that effectively reduced the actuator stroke, but this phenomenon did not significantly affect the performance of the actuator. The pressurized unit module and actuator combination was able to produce repeatable motion at a frequency of 0.05Hz. Several limitations such as: 1) The high current requirement of the actuators, 2) The inefficient actuation system, and 3) The connectivity issues between the actuators and the modules remain to be solved in order to build a reliable device.

10.2 RECOMMENDATIONS

Addressing the three issues listed above is crucial in the development of a working SMA driven hyper-redundant manipulator. Further optimization of the actuator profile to decrease the SMA sheet cross-section would help reduce the heating current and power requirements. A detailed study of the effects of composite plating on the straight sections of the actuator should also be carried out since the results proved inconclusive. Cold spraying techniques offer the possibility of creating solid composite panels, eliminating the need for conductive epoxy and increasing the fatigue resistance of the actuators. This process could also be used to include copper solder tabs at the actuator ends, again eliminating the need for epoxies. The greatest challenge remains the reformulation of the actuation system. Even with the small number of actuators, it was found that the proposed actuation system required a large number of wires. These findings, along with results taken from the literature favour an on-board electronic system, which would limit the number of wires and greatly facilitate the assembly process.

References

1. Ashby, M., Fleck, N. and Huber, J., 2001. "The selection of Sensors", *Progress in Materials Science*, vol. 46, no. 3-4, pp.461-504.
2. Ashby, M., Fleck, N. and Zupan, M., 2002. "Actuator Classification and Selection-The Development of a Database," *Advanced Engineering Materials 2002*, vol. 4, no. 12, pp. 933-939.
3. Avallone, E. and Baumeister III, T., 1996, "Marks' Standard Handbook for Mechanical Engineers, tenth edition", *McGraw Hill*, pp. 5-50.
4. Boyd, J. G. and Lagoudas, D. C., 1996. "Memory materials part 1: The monolithic shape memory alloy", *International Journal of Plasticity*, vol. 12, no. 6, pp. 805-842.
5. Brinson, L. C., 1993. "One-dimensional constitutive behavior of shape memory alloys: thermomechanical derivation with non-constant material functions and redefined martensite internal variables", *Journal of Intelligent Material Systems and Structures*, vol. 4, no. 2, pp. 229-242.
6. Brocca, M., Brinson, L. C. and Bazant, Z. P., 2002. "Three-dimensional constitutive model for shape memory alloys based on microplane model", *Journal of the Mechanics and Physics of Solids*, vol. 50, no. 5, May, pp.1051-1077.
7. Chirikjian, G. and Suthakorn, J., 2001. "Design and Implementation of a New Discretely-Actuated Manipulator," *Springer Berlin/Heidelberg*, vol. 271, pp. 151-157.
8. Cieslak, R. and Morecki, A., 1999. "Elephant Trunk Type Elastic Manipulator – a tool for bulk and liquid materials transportation," *Robotica*, vol. 17, pp. 11-16.
9. Conkur, E. S., 2003. "Path following algorithm for highly redundant manipulators", *Robotics and Autonomous Systems,* vol. 45, no. 1, Oct., pp. 1-22.
10. Deyer, C. W. and Brei, D. E., 2001. "Proof of Concept of a Novel SMA Cage Actuator", *Proc. of SPIE*, vol. 4332, June, pp. 234-245.

11. Dubowsky, S., Hafez, M., Lichter, M. and Wingert, A., 2002. "Hyper-Redundant Robot Manipulators Actuated by Optimized Binary Dielectric Polymers," *Proc. SPIE*, vol 4695, pp.415-423.
12. Dubowsky, S. and Sujan, V., 2004. "Design of a Lightweight Hyper-Redundant Deployable Binary Manipulator," *J. Mech. Design,* vol. 126, Jan., pp.29-39.
13. Esashi, M., Kobayashi, S., Haga, Y., Watanabe, Y., Mitsui, T. and Mineta, T., 2002 "An Active Guide Wire with Shape Metal Alloy Bending Actuator Fabricated by Room Temperature Process," *Sensors and Actuators A*, vol. 97-98, pp. 632-637.
14. Fan, J. and Peng, X., 1991. "A physically based constitutive description for non-proportional cyclic plasticity", *J. Eng. Mater. Tech.*, vol. 113, pp. 254-262.
15. Fu, Y. and Du, H., 2003. "RF magnetron sputtered TiNiCu shape memory alloy thin film", *Mater. Sci. Eng. A Struct.: Mater. Prop. Microstruct. Proc.*, vol. 339, no. 1-2, pp. 10-16.
16. Gravagne, I. A. and Walker, I., 2002. "Uniform Regulation of a Multi-Section Continuum Manipulator," *IEEE Int. Conf.: Robotics and Automation*, vol.2, pp. 1519-1524.
17. Hafez, M., Lichter, M. D. and Dubowsky, S., 2003. "Optimized binary modular reconfigurable robotic devices", *IEEE/ASME Trans. on Mechatronics*, vol. 8, no. 1, March, pp. 18-25.
18. Hirose, S., 1987. "Biologically Inspired Robots – Snake-Like Locomotors and Manipulators," *Oxford Science Publications*, Tokyo, (translated in 1993).
19. Holman, J. P., 1997. "Heat Transfer", *McGraw-Hill*, pp. 341-350.
20. Hornbogen, E., 2002. "Some effects of martensitic transformation on fatigue resistance", *Fat. Fract. Eng. Mater. & Struct.*, vol. 25, no. 8-9, Sept., pp.785-790.
21. Hsu, T. Y. and Xuemin, L., 1987. "An investigation of phase transformations in a 50.8at.%Ni-Ti shape memory alloy", *Material Science and Engineering*, vol. 91, no. 1-2, July, pp. 189-194.
22. Jin, Y. M. and Weng, G. J., 2000. "Micromechanics study of thermomechanical characteristics of polycrystal shape-memory alloy films", *Thin Solid Films*, vol. 376, no. 1-2, pp. 198-207.

23. Kim, B., Lee, S., Park, J. H. and Park, J., 2005. "Design and Fabrication of a Locomotive Mechanism for Capsule-Type Endoscopes Using Shape Memory Alloys", *IEEE/ASME Trans. on Mechatronics*, vol. 10, no. 1, Feb., pp. 77-86.
24. Kornbluh, R., Pelrine, R., Pei, Q., Heydt, R., Stanford, S., Oh, S. and Eckerle, J., 2002. "Electroelastomers: Applications of dielectric Elastomer transducers for actuation, generation, and smart structures", *Proc. SPIE*, vol. 4698, pp.254-270.
25. Kuribayashi, K., 1989 "Millimeter-sized Joint Actuator Using a Shape Memory Alloy", *Sensors and Actuators*, vol. 20, no. 1-2, Nov., pp.57-64.
26. Lagoudas, D. C. and de Blonk, B. J., 1998. "Actuation of elastomeric rods with embedded two-way shape memory alloy actuators", *Smart Materials and Structures*, vol. 7, no. 6, Dec., pp.771-783.
27. Lexcellent, C., Moyne, S., Ishida, A. and Miyazaki, S., 1998. "Deformation behavior associated with the stress-induced martensitic transformation in Ti-Ni thin films and their thermodynamical modelling", *Thin Solid Films*, vol. 324, no. 1, July, pp.184-189.
28. Lim, G., Park, K., Sugihara, M., Minami, K. and Esashi, M., 1996. "Future of active catheters", *Sensors and Actuators A*, vol. 56, Aug., pp. 113-121.
29. Lu, A., Grant, D. and Hayward, V., 1997. "Design and Comparison of High Strain Shape Memory Alloy Actuators", *Proc. of the 1997 IEEE: International Conference on Robotics and Automation*, vol.1, Apr., pp.260-265.
30. Mineta, T., Mitsui, T., Matanabe, Y., Kobayashi, S., Haga, Y. and Esashi, M., 2001. "Batch fabricated flat meandering shape memory alloy actuator for active catheter", *Sensors and Actuators A*, vol. 88, no. 2, pp. 112-120.
31. Mineta, T., Mitsui, T., Matanabe, Y., Kobayashi, S., Haga, Y. and Esashi, M., 2002. " An active guide wire with shape memory alloy bending actuator fabricated by room temperature process", *Sensors and Actuators A*, vol. 97-98, pp. 632-637.
32. Molina-Vilaplana, J., Pedreño-Molina, J. L. and López-Coronado, J., 2004. "Hyper RBF model for accurate reaching in redundant robotic systems", *Neurocomputing*, vol. 61,Oct., pp. 495-501.

33. Mukherjee, R., Christian, T. F. and Thiel, R. A., 1996. "An actuation system for the control of multiple shape memory alloy actuators", *Sensors and Actuators A*, vol. 55, no. 2, July, pp. 185-192.
34. Nakanishi, N., Mori, T., Miura, S., Murakami, Y. and Kashi, S., 1973. "Pseudoelasticity in Au-Cd thermoelastic martensite", *Phil. Mag.*, vol. 28, no. 2, pp. 277-292.
35. Peirs, J., Reynaerts, D. and Van Brussel, H., 1998. "A Micro Robotic Arm for a Self Propelling Colonoscope," *Proc. Actuator 98, 6th International Conference on New Actuators,* Bremen, Germany, pp. 576-579.
36. Peirs, J., Reynaerts, D. and Van Brussel, H., 1998. "Design of a shape memory actuated endoscopic tip", *Sensors and Actuators A*, vol. 70, no. 1-2, pp.135-140.
37. Peng, X., Yang, Y. and Huang, S., 2001. "A comprehensive description for shape memory alloys with a two phase constitutive model", *International Journal of Solids and Structures*, vol. 38, no. 38-39, p.6925-6940.
38. Russell, R. A. and Gorbet, R. B., 1995. "Improving the Response of SMA Actuators", *Int. Conf.: Robotics and Automation*, vol. 3, May, pp. 2299-2304.
39. Ryhänen, J., 1999. "Biocompatibility evaluation of nickel-titanium shape memory metal alloy", Ph.D. Thesis, Oulu University, Finland.
40. Sittner, P. and Takuda, M., 1995. "Reorientation in combined stress-induced martensite", *J. Physique IV*, vol. 5, no. 8, pp. C8.1003-C8.1008.
41. Song, G., Chaudhry, V. and Batur, C., 2003. "Precision tracking control of shape memory alloy actuators using neural networks and a sliding-mode based robust controller", *Smart Materials and Structures*, vol. 12, no. 2, pp. 223-231.
42. Song, G. and Ma, N., 2003. "Control of shape memory alloy actuators using pulse-width pulse-frequency (PWPF) modulation", *Journal of Intelligent Material Systems and Structures*, vol. 14, no. 1, pp. 15-22.
43. Sun, Q. P. and Wang, K. C., 1993. "Micromechanics modeling for the constitutive behavior of polycrystalline shape memory alloys", *J. Mech. Phys. Solids*, vol. 41, no. 1, pp.1-17.

44. Szewczyk, J., de Sars, V., Bidaud, P. and Dumont, G., 2000. "An Active Tubular Polyarticulated Micro-System for Flexible Endoscope," *Springer-Verlag: Experimental Robotics VIII*, vol. 271, Dec., pp. 179-188.

45. Tanaka, K., 1986. "A thermomechanical sketch of shape memory effect: One-dimensional tensile behavior", *Res. Mech.*, vol. 18, no. 3, pp. 251-263.

46. Tobushi, H., Shimeno, Y., Hachisuka, T. and Tanaka, K., 1998. "Influence of strain rate on superelastic properties of TiNi shape memory alloy", *Mechanics of Materials*, vol. 30, no.2, pp. 141-150.

47. Valanis, K. C. and Fan, J., 1983. "Endochronic analysis of cyclic elastoplastic strain fields in a notched plate", *J. App. Mech.*, vol. 50, no. 4A, pp. 789-793.

48. Walker, I. D. and Hannan, M., 1990. "A Novel 'Elephant's Trunk' Robot," *Proc. IEEE/ASME Int. Conf. On Advanced Intelligent Mechatronics*, pp.410-415.

49. Wang, G. and Shahinpoor, M., 1997. "A new design for a rotatory joint actuator made with shape memory alloy contractile wire", *Journal of Intelligent Material Systems and Structures*, vol. 8, no. 3, March, pp. 215-219.

50. Wang, Y. and Chirikjian, G. S., 2004. "Workspace generation of hyper-redundant manipulators as a diffusion process on *SE(N)*", *IEEE Trans. on Robotics and Automation,* vol. 20, no. 3, June, pp. 399-408.

51. Wang, Z., Zu, X., Feng, X. and Dai, J., 2002. "Effect of thermomechanical treatment on the two-way shape memory effect of NiTi alloy spring", *Materials Letters*, vol. 54, no. 1, May, pp. 55-61.

52. Wang, Z. G., Zu, X. T., Feng, X. D., Lin, L. B., Zhu, S., You, L.P. and Wang, L.M., 2003. "Design of TiNi alloy two-way shape memory coil extension spring", *Mater. Sci. Eng. A Struct.: Mater. Prop. Microstruct. Proc.*, vol. 345, no. 1-2, pp. 249-254.

53. Wayman, C. M. and Duerig, T. W., 1990. "Engineering Aspects of Shape Memory Alloys", *Butterworth-Heineman,* Nov., pp.3-20.

54. Zhang, Y., Wang, J. and Xu, Y., 2002 "A dual neural network for bi-criteria kinematic control of redundant manipulators", *IEEE Trans. on Robotics and Automation,* vol. 18, no. 6, Dec., pp. 923-931.

Appendices

APPENDIX A – ACTUATOR TYPE COMPARISON

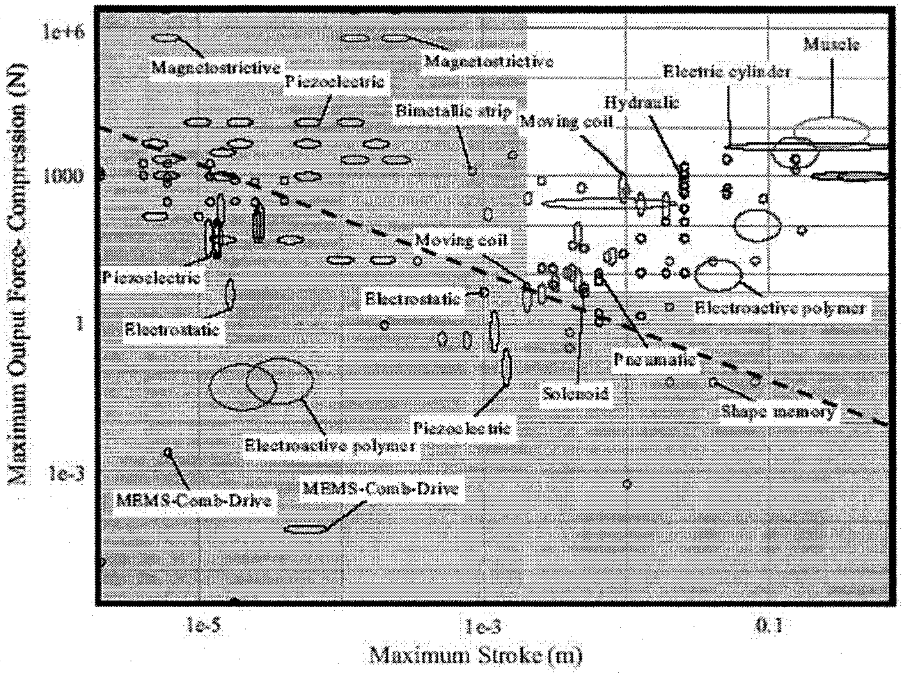

Figure A-1: Actuator output force versus displacement [1]

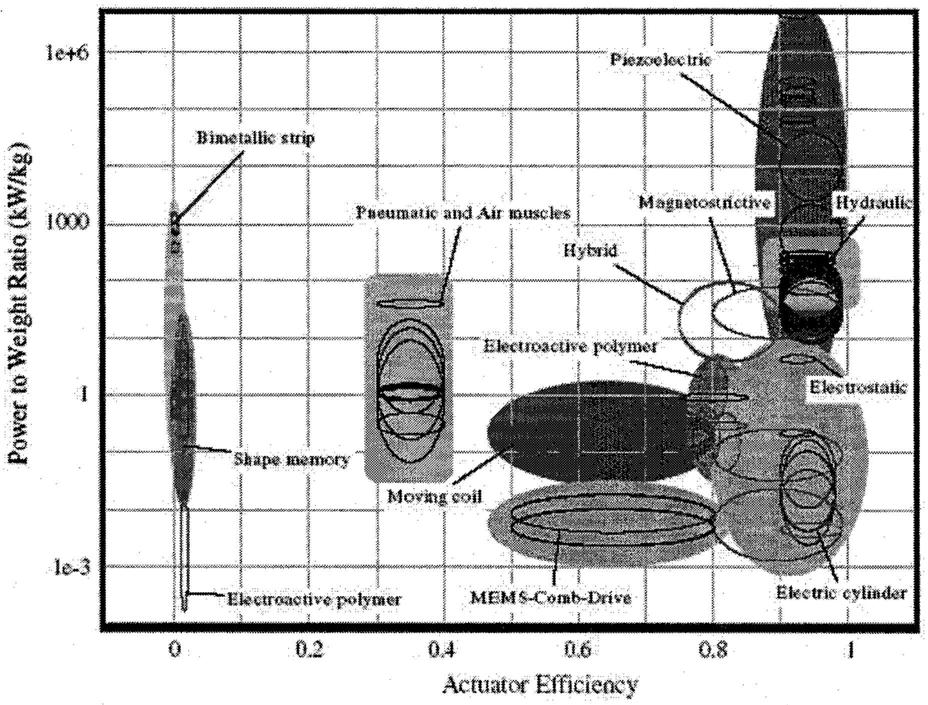

Figure A-2: Power to weight ratio versus efficiency [1]

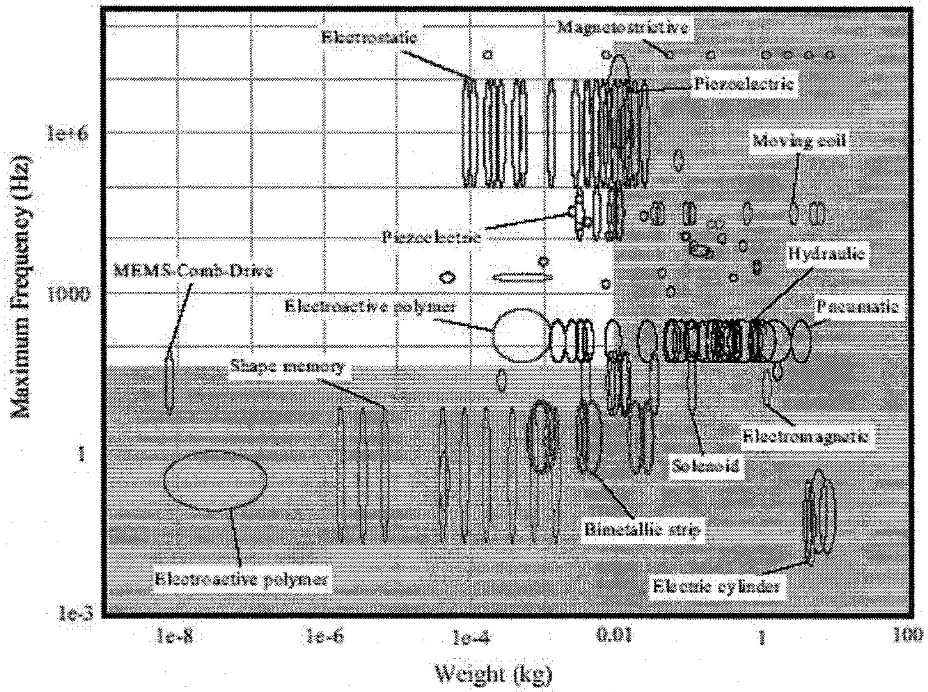

Figure A-3: Maximum frequency versus actuator mass [1]

APPENDIX B – EXPERIMENTAL DETERMINATION OF THE MATERIAL PARAMETERS

The material parameters can be separated into three groups: parameters of martensite, of austenite and those related the forward and reverse martensitic transformation [37]. The parameters related to the martensite and austenite case can be identified with an elastoplastic deformation test. For the martensite phase the parameters G_m (or E_m), Poisson's ratio v_m, C_r and a_r can be found by maintaining the temperature below the martensite finish temperature. The parameters G_a and v_a for austenite are determined by keeping the temperature sufficiently high such that no martensitic transformation can occur and the SMA is completely composed of austenite. To determine if there are any temperature effects on these parameters, the tests may be repeated several times at slightly different temperatures.

The martensite and austenite start and finish temperatures (M_S, M_F, A_S and A_F) are usually provided by the manufacturer but can easily be determined using a simple resistivity test. Pseudoelastic and SME tests can be used to identify the rest of the parameters. A_M and B_M are determined in the loading process involving stress induced martensitic transformation, A_A and B_A are determined in the unloading process involving stress induced reverse martensitic transformation and k_t is determined with SME [37].

In the original martensite volume fraction expression developed by Tanaka [46], the parameters A_M and A_A can also be determined arithmetically using the following relations.

$$A_M = \frac{\ln(0.01)}{M_S - M_F}, \quad A_A = \frac{\ln(0.01)}{A_S - A_F} \qquad \textbf{(A-1)}$$

APPENDIX C – TWO-PHASE CONSTITUTIVE MODEL MATLAB CODE

The code for the actuator constitutive model illustrated in Figure 4-2 is composed of several sub-functions imbedded in two loops. Each sub-function represents one or several internal variables. The internal loop computes the stress output for a unit thickness for the complete strain cycle and the main loop repeats the procedure for each unit thickness. The stress matrix is then used to compute the output moment and force.

Code 1: Main Program

```
function SMAmodel

clear all;
clear global;
clear variables;

%State all global variables, material constants and actuator dimensions
global e eP eT S Sa Sm V Va Vm dVa dVm sig Q1 Q2 Q3 dz dsigdT T dt dphi
D dz2 B stressA stressM A D Ekk dEkk E Et Seq SeqAvr dSeq de deP deT
dSm dSa dQ1 dQ2 dQ3 dsig dT ;
global Ga Gm Ea Em Ka Km C a Aa Am Ba Bm kT alphaA alphaM T0 As Ms Af
Mf P;
global L theta0 R thick width r dtheta dSmAvr;

%Initialize variables, material and geometric constraints
InitializeMaterial;
InitializeVariables;
InitializeGeometrics;
InitializeControl;

%Obtain strain distribution
Edistribution; %eq 5: E(r,t) x-section strain distribution

%Complete simulation per unit cross-section-------------------Main loop
for i=1:length(r)
```

```
%Simulation per unit time for one section of radii-------------Sub Loop
    for t=1:length(T)

        Deviatoric(i,t);%eq 41: e(t+1) de(t+1) Ekk(t+1) dEkk(t+1)
        Xi(t);          %eq 31: sig(t+1) dsig(t+1) T(t+1) dT(t+1)
dSeq(t) sig(t)
        DeTFUNC(t);     %eq 24: eT(t+1) deT(t+1) eT(t) eP(t)
dsigdT(t+1) dT(t+1)
        DphiFUNC(t);    %eq 38: dphi(t+1) de(t+1) deT(t+1) D(t) Sm(t)
dsig(t+1)
        DzFUNC(t);      %eq 39: dz(t+1) B(t) dphi(t+1) sig(t+1)
        DQFUNC(t);      %eq 21, eq 22: dQ(t+1) Q(t+1) B(t+1) D(t+1)
eP(t) Q(t)
        DStress(i,t);   %eq 17, eq 35, eq 37: Sa(t+1) S(t+1) Seq(t+1)
dSeq(t+1) stress(t+1)
        VStress(i,t);   %eq 19: V Vm Va(t)

    end %---------------------------------------------------Sub Loop #1

end%----------------------------------------------------------Main Loop

moment = ActuatorMoment;
force = ActuatorForce(moment);

plot(Et,force);
ylim([0 .2])
xlim([0 3])
xlabel('Actuator Total Strain [100%]')
ylabel('Force [N]')
```

Code 2: Initialization Functions

```
function InitializeMaterial;

global Ga Gm Ea Em Ka Km C a Aa Am Ba Bm kT alphaA alphaM T0 As Ms Af
Mf P;
```

```
Ga = 31.0;
Gm = 13.0;
Ka = 81;
Km =34;
C = [550 15 1.3];
a = [28000 750 80];

kT = 3.2;
alphaA = 11.0e-6;                 %(mm/mm) / C
alphaM = 6.6e-6;                  %(mm/mm) / C
T0 = 300;                         %kelvin
As = 345;                         %kelvin
Af = 358;                         %kelvin
Ms = 331;                         %kelvin
Mf = 273+30;                      %kelvin



function InitializeVariables;

global eP eT de deT deP dSmAvr Q1 Q2 Q3 dQ1 dQ2 dQ3 S Sm Sa B Seq sig
dsig dsigdT V Va Vm stress D SeqAvr;

eP(:,:,1) = zeros(3);
eP(:,:,2) = zeros(3);
eT(:,:,1) = zeros(3);
eT(:,:,2) = zeros(3);
de(:,:,1) = zeros(3);
deT(:,:,1) = zeros(3);
deP(:,:,1) = zeros(3);
Q1(:,:,1) = zeros(3);
Q2(:,:,1) = zeros(3);
Q3(:,:,1) = zeros(3);
Q1(:,:,2) = zeros(3);
Q2(:,:,2) = zeros(3);
Q3(:,:,2) = zeros(3);
dQ1(:,:,1) = zeros(3);
dQ2(:,:,1) = zeros(3);
dQ3(:,:,1) = zeros(3);
```

```
S(:,:,1) = zeros(3);
Sm(:,:,1) = zeros(3);
dSmAvr(:,:,1) = zeros(3);
dSmAvr(:,:,2) = zeros(3);
dSmAvr(:,:,3) = zeros(3);
Sa(:,:,1) = zeros(3);
dSa(:,:,1) = zeros(3);
B(:,:,1) = zeros(3);
B(:,:,2) = zeros(3);
D(:,:,1) = zeros(3);
D(:,:,2) = zeros(3);
Seq(1)=0;
dSeq(1)=0;
dSeq(2)=0;
dSeq(3)=0;
dSeq(4)=0;
SeqAvr(1)=0;
SeqAvr(2)=0;
SeqAvr(3)=0;
SeqAvr(4)=0;
sig(1)=1;
dsig(1)=0;
V(1)=0;
Va(1)=0;
Vm(1)=0;
stress(1)=0;
dsigdT(1)=0;


function InitializeGeometrics;

global L theta0 R thick width MaxStrain dr r;

L = 2.86;
R = 0.32;    %internal radius: R<CG<R+thick
thick = 0.07;
width = 5.9;
```

```
function InitializeControl;

global T0 Af;
global T dT dt Et;
global R thick theta0 MaxStrain dr L r;

dT(1)=0;                     %temperature derivative
dt = 0.01;                   %seconds
simulationtime = 7;          %seconds
Tstartime = 2;               %used in first sinus based Temp control
theta0=pi/2;
MaxStrain = 0.03;
dr = thick/50;
r = R:dr:R+thick;            %thickness variable
dtheta = 0:0.01:pi/2;        %initial angle variable
T(1)=294;
Et(1)=0;

%----Obtain maximum deflection angle and total strain according to
actuator size---

Rcurv = thick/log((R+thick)/R);     %radius of curvature

for m = 1:length(dtheta)
    strain(:,m) = (Rcurv-r)./r/theta0*dtheta(m);
    if strain(1,m)<MaxStrain
        trunkstrain(:,m)=strain(:,m);
        trunkdtheta(m)=dtheta(m);
    else
        m = m-1;
        break;
    end
end
MaxAngle = trunkdtheta(m);

Y = theta0 - MaxAngle;         %internal variable
X = (R+thick/2)*theta0;        %internal variable
```

```
MaxTotStrain = ([L*cos(Y)-X/Y*(theta0*cos(Y)-sin(Y))]-
(R+thick/2))/(R+thick/2);%page42 1stBook

%------------------Et T and dT generation------------------
t = 0 : dt : simulationtime;

%Varying temperature and strain
%{
Et = MaxTotStrain*(-cos(t)+ 1)/2;
for h=1:length(t)
    if t(h)<Tstartime
        T(h) = T0;
    else
        T(h) = ((Af+30)-T0)*(-cos(t(h)-Tstartime))/2+ T0 + ((Af+30)-
T0)/2;
    end
end
%}

%Varying strain with full austenite temperature
%{
j=1;
for i=2:length(t)

    if T(i-1)<357    %357
        T(i)=T(i-1)+1;
        Et(i)=0;
        j=j+1;
    else
        T(i)=T(i-1);
        Et(i)=MaxTotStrain*(-cos((i-j)/100)+1)/2;
    end
end
%}

%Martensite temperature and triangular strain pattern
for i=2:length(t)
    T(i)=294;
```

```
end
i=2;
while Et(i-1)<MaxTotStrain
    Et(i)=Et(i-1)+0.005;
    i=i+1;
end
while Et(i-1)>2.42%63
    Et(i)=Et(i-1)-0.005;
    i=i+1;
end
while i<=length(t)
    Et(i)=Et(i-1);
    i=i+1;
end

%Definition of dT
for h=2:length(T)
    dT(h)=T(h)-T(h-1);
end
```

Code 3: Strain Distribution

```
function Edistribution;


global e Ekk E Et;
global L theta0 R thick width r dtheta;
global VAR1; %local variable

R0 = R + thick/2;

%------------------Vertical position WRT total strain-------------------
y = Et*R0 + R0;

%-------Obtain change in angle of circular arc of actuator section------
for i=1:length(y)
    VAR1=y(i);
    theta(i) = fzero(@yfunction,[0.8 2]);
```

```
end
dtheta = theta0 - theta;
%--------------Obtain strain distribution across thickness-------------
Rcurv = thick/log((R+thick)/R);
for i = 1:length(dtheta)                          %i is the universal time
    E(:,i) = (Rcurv-r)./r/theta0*dtheta(i);   %E(r,t) where R<r<R+thick
end



end %----------------------------end---------------------------

function [fun] = yfunction(Y)
global L theta0 R thick VAR1;
fun = L*cos(Y)-((R+thick/2)*theta0)*(theta0*cos(Y)-sin(Y))/Y - VAR1;
end
```

Code 4: Deviatoric Strain

```
function Deviatoric(i,t)

global e de Ekk dEkk E T;

v = 0.33;     %Poisson ratio
dEkk(1) = 0;

if t<length(T)
    Ekk(t+1)=E(i,t+1)*(1-2*v);
    e(:,:,t+1) = [(E(i,t+1)-Ekk(t+1)/3) 0 0;0 (-Ekk(t+1)/3) 0;0 0 (-
Ekk(t+1)/3)];
    de(:,:,t+1) = e(:,:,t+1) - e(:,:,t);
    dEkk(t+1) = Ekk(t+1) - Ekk(t);
end
```

Code 5: Martensite Volume Fraction

```
function Xi(t);
```

```
global T dT dSeq Seq dsig sig dsigdT de e dSm Sm SeqAvr;
global Aa Am Ba Bm As Ms Af;
BA=10;%10
BM=15;%13
Aa = 0.45;
Am = 0.25;
Ba = 60;
Bm = 30;

if t>1

    if Ms+Bm*SeqAvr(t-1)-T(t) <=0  &  sig(t-1)<0.01   %A->M
        sig(t)=0;
        dsig(t)=0;
    elseif T(t)-As-Ba*SeqAvr(t-1) <= 0  &  sig(t-1)>0.99   %M->A
        sig(t)=1;
        dsig(t)=0;
    else

        if dT(t)-Ba*dSeq(t-1)>=0                              %M->A
            dsig(t)= -Aa * sig(t-1) * (dT(t) - BA*dSeq(t-1));

            %negative strain criteria || positive strain criteria
            if Sm(1,1,t-1)<0.004 & dSeq(t-1)<0 & dSm(1,1,t-1)>0 &
e(1,1,t)<0 | Sm(1,1,t-1)>-0.004 & dSeq(t-1)<0 & dSm(1,1,t-1)<0 &
e(1,1,t)>0
                dsig(t)=0;
            end

        elseif -dT(t)+Bm*dSeq(t-1)>0                          %A->M +
            dsig(t)= Am * (1 - sig(t-1)) * (-dT(t) + BM*dSeq(t-1));
        else
            dsig(t)=0;
        end

        sig(t) = sig(t-1) + dsig(t);

        end
```

```
        if sig(t)<0
            sig(t)=0;
        elseif sig(t)>1
            sig(t)=1;
        end

    end

    if dT(t) ~= 0
        dsigdT(t) = dsig(t) / dT(t);
    else
        dsigdT(t)=0;
    end

end
```

Code 6: Phase Transformation Strain

```
function DeTFUNC(t);

global kT eP eT deT dsigdT dT T;

if t>1

    deT(:,:,t) = kT/2 * (eP(:,:,t) + eT(:,:,t)) * (dsigdT(t)*dT(t) -
abs(dsigdT(t)*dT(t)) );

    eT(:,:,t+1) = deT(:,:,t) + eT(:,:,t);

end
```

Code 7: Ψ

```
function DphiFUNC(t);

global de deT sig dsig dphi D Sm T;
global Gm;
```

```
if t>1
    if sig(t)>0.01
        VAR = 2*Gm*sig(t)*(de(:,:,t)-deT(:,:,t)) - (D(:,:,t) -
Sm(:,:,t-1)/sig(t))*dsig(t);
    else
        VAR = zeros(3);
    end

    if isempty(VAR)
        dphi(:,:,t)=zeros(3);
    else
        dphi(:,:,t)=VAR;
    end
end
```

Code 8: Generalized Time

```
function DzFUNC(t);

global dphi B sig dz dz2 P T;
global  Gm C;

if t>1
    A1=TensorContract2nd(B(:,:,t),B(:,:,t));
    A2=(sig(t)*sum(C) + 2*sig(t)*Gm)^2;
    A3=TensorContract2nd(B(:,:,t),dphi(:,:,t));
    A4=TensorContract2nd(dphi(:,:,t),dphi(:,:,t));

    vector = [A1-A2 -2*A3 A4];

    r = roots(vector);


    if isempty(r)
        dz(t)=0;
        dz2(t)=0;
    else
        if r(2)>=0
```

```
            dz(t)=r(2);     %r2 is smaller and more stable
            dz2(t)=2;
        elseif r(1)>=0
            dz(t)=r(1);
            dz2(t)=1;
        else
            dz(t)=0;
            dz2(t)=3;
        end
    end
end
```

Code 9: Generalized Force

```
function DQFUNC(t);

global Q1 Q2 Q3 dQ1 dQ2 dQ3 sig dsig e eP Sm dSm dSmAvr deP deT de dz T
B D dphi;
global C a Gm;

if t>1
    A=sig(t)*(sum(C));

    if sig(t)>0.001
        deP(:,:,t) = (-B(:,:,t)*dz(t) + dphi(:,:,t))/(A + 2*sig(t)*Gm);
        dQ1(:,:,t) = sig(t)*C(1)*deP(:,:,t) + (dsig(t)/sig(t) -
a(1)*dz(t))*Q1(:,:,t);
        dQ2(:,:,t) = sig(t)*C(2)*deP(:,:,t) + (dsig(t)/sig(t) -
a(2)*dz(t))*Q2(:,:,t);
        dQ3(:,:,t) = sig(t)*C(3)*deP(:,:,t) + (dsig(t)/sig(t) -
a(3)*dz(t))*Q3(:,:,t);
        %dSm(:,:,t) = A*deP(:,:,t) + B(:,:,t)*dz(t) + D(:,:,t)*dsig(t);
        dSm(:,:,t) = dQ1(:,:,t) + dQ2(:,:,t) + dQ3(:,:,t); %more stable
in the M->A transision
        eP(:,:,t+1) = deP(:,:,t) + eP(:,:,t);
        Q1(:,:,t+1) = dQ1(:,:,t) + Q1(:,:,t);
        Q2(:,:,t+1) = dQ2(:,:,t) + Q2(:,:,t);
        Q3(:,:,t+1) = dQ3(:,:,t) + Q3(:,:,t);
```

```
        Sm(:,:,t) = dSm(:,:,t) + Sm(:,:,t-1);

    else
        deP(:,:,t) = zeros(3);
        eP(:,:,t+1) = zeros(3);
        dSm(:,:,t) = zeros(3);
        Sm(:,:,t) = zeros(3);
        Q1(:,:,t+1) = zeros(3);
        Q2(:,:,t+1) = zeros(3);
        Q3(:,:,t+1) = zeros(3);
    end

    if t>3
        dSmAvr(:,:,t)=(dSm(:,:,t)+dSm(:,:,t-1)+dSm(:,:,t-2)+dSm(:,:,t-
3))/4;
    end

    B(:,:,t+1) = -(a(1)*Q1(:,:,t+1) + a(2)*Q2(:,:,t+1) +
a(3)*Q3(:,:,t+1));

    if sig(t)>0.01
        D(:,:,t+1) = 1/sig(t)*(Q1(:,:,t+1)+Q2(:,:,t+1)+Q3(:,:,t+1));
    else
        D(:,:,t+1) = zeros(3);
    end
end
```

Code 10: Volumetric Stress

```
function VStress(i,t);

global V Va Vm dVm dVa Ekk dEkk sig dsig T S Sm Sa dT stress;
global Ka Km alphaA alphaM T0;

T0a = 357;
%
Vm(t)= 3*sig(t)*Km*(Ekk(t) - 3*alphaM*(T(t)-T0));
Va(t)= 3*(1-sig(t))*Ka*(Ekk(t) - 3*alphaA*(T(t)-T0a));
```

```
V(t) = Va(t) + Vm(t);
stress(i,t) = Sa(1,1,t)+ Sm(1,1,t);
```

Code 11: Moment and Force

```
function moment=ActuatorMoment;

global T stress;
global thick R width r dr;

Rcurv = thick/log((R+thick)/R);


for i=1:length(T)

   moment(i) = width/1000 * sum(stress(:,i)*1e9.*((Rcurv-
r(:))/1000)*(dr/1000));

end



function force = ActuatorForce(moment);

global theta0 dtheta thick L R;

theta = theta0-dtheta;
R0 = thick/log((R+thick)/R);

%calculate x position wrt the angle change
Xe = R0*theta0./theta.*(1-cos(theta)) + (L-R0*theta0)*sin(theta);

%get force(t)
force = moment./(Xe/1000);
```

APPENDIX D – SMA RESPONSE FOR NEGATIVE STRAINS

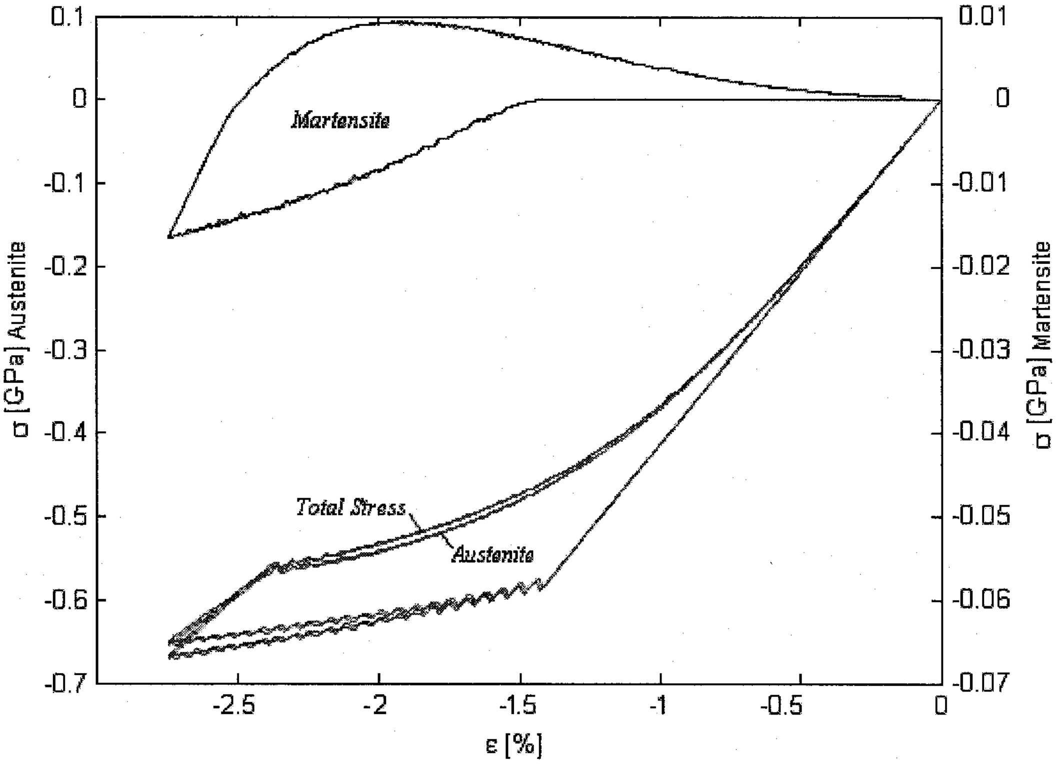

Figure A-4: Pseudoelasticity of NiTi at 84°C for negative strains

APPENDIX E – APPROXIMATE FORWARD KINEMATICS ALGORITHM

This function determines the homogeneous transformation matrices *A* for each module based on the actuator lengths computed from (5-3) to (5-6). This function is the starting point for the refined kinematics algorithm.

Code 12: Approximate Forward Kinematics

```
function [Ai,Aii,Aiii,Aiv,disp0,type]= Point_Cloud(R1,R2,L);

%lengths determined by static analysis
l1=18.99; h1=15.92; l123=13.59;

%rotations between anchor points
RzNeg = [cos(-2*pi/3) -sin(-2*pi/3) 0 0;sin(-2*pi/3) cos(-2*pi/3) 0 0;0
0 1 0;0 0 0 1];
RzPos = [cos(2*pi/3) -sin(2*pi/3) 0 0;sin(2*pi/3) cos(2*pi/3) 0 0;0 0 1
0;0 0 0 1];

%----------------------------One actuator case-------------------------

%theta is negative since l1<L produces negative X rotation
theta = atan((-L^2+2*l1*L+8*R2*R1+4*R1^2-
l1^2+4*R2^2)^(1/2)/(R2+R1)^2*(-l1+L)/(-4*R2*R1-2*R1^2-2*R2^2+l1^2-
2*l1*L+L^2)*(2*R2*R1+R1^2+R2^2));
%z is negative but calculated based on positive theta
z = L+L*((1-(R2*cos(-theta)-R2+R1*cos(-theta)-R1)^2/(-l1+L)^2)^(1/2)-
1)-R2*sin(-theta);
%y is positive but calculated based on positive theta
y = L/(l1-L)*(R2+R1)*(cos(-theta)-1)+R2*(cos(-theta)-1);
%x is zero
x = 0;

R = [1 0 0 0;0 cos(theta) -sin(theta) 0;0 sin(theta) cos(theta) 0;0 0 0
1];
D = [0 0 0 x;0 0 0 y;0 0 0 z;0 0 0 0];
```

```
%Position 100
A100 = R+D;
%Position 010
A010 = AxisAngle(-2*pi/3,theta)+RzNeg*D;
%Position 001
A001 = AxisAngle(2*pi/3,theta)+RzPos*D;

%----------------------------Two Actuator Case----------------------------

%theta is positive since h1<L produces positive X rotation
theta2 = -atan(2*(-L^2+2*L*h1+4*R2*R1+R1^2+4*R2^2-h1^2)^(1/2)*(L-
h1)/(2*L^2-4*L*h1+2*h1^2-4*R2^2-4*R2*R1-R1^2));
%z is positive and calculated based on positive theta
z2 = L+L*(1/2*sin(theta2)*(2*R2+R1)/(L-h1)-1)-sin(theta2)*R2;
%y is negative and calculated based on positive theta
y2 = -1/2*L*(4-sin(theta2)^2*(2*R2+R1)^2/(L-h1)^2)^(1/2)-
R2*(cos(theta2)-1);
%x is zero
x2 = 0;

R2 = [1 0 0 0;0 cos(theta2) -sin(theta2) 0;0 sin(theta2) cos(theta2)
0;0 0 0 1];
D2 = [0 0 0 x2;0 0 0 y2;0 0 0 z2;0 0 0 0];

%Position 011
A011 = R2+D2;
%Position 101
A101 = AxisAngle(-2*pi/3,theta2)+RzNeg*D2;
%Position 110
A110 = AxisAngle(2*pi/3,theta2)+RzPos*D2;

%---------------------------Three Actuator Case--------------------------

%R3 and R4 equal 0 therefore A is equal to D
A111 = [1 0 0 0;0 1 0 0;0 0 1 l123;0 0 0 1];
A000 = [1 0 0 0;0 1 0 0;0 0 1 L;0 0 0 1];
```

```
A(1:4,1:4,1)=A000;
A(1:4,1:4,2)=A100;
A(1:4,1:4,3)=A010;
A(1:4,1:4,4)=A001;
A(1:4,1:4,5)=A011;
A(1:4,1:4,6)=A101;
A(1:4,1:4,7)=A110;
A(1:4,1:4,8)=A111;

%-------------------------End-effector Coordinates----------------------
w=1;
for i=1:8
    for j=1:8
        for k=1:8
            for l=1:8
                Tmatrix=A(:,:,i)*A(:,:,j)*A(:,:,k)*A(:,:,l);
                disp0(w,1:3)=Tmatrix(1:3,4);
                Ai(1:4,1:5,w) = horzcat(A(:,:,i),[i;0;0;0]);
                Aii(1:4,1:5,w) = horzcat(A(:,:,j),[0;j;0;0]);
                Aiii(1:4,1:5,w) = horzcat(A(:,:,k),[0;0;k;0]);
                Aiv(1:4,1:5,w) = horzcat(A(:,:,l),[0;0;0;l]);
                type(w,1:4) = [i j k l];
                w=w+1;
            end
        end
    end
end

plot3(disp0(:,1),disp0(:,2),disp0(:,3),'k.')
```

APPENDIX F – REFINED FORWARD KINEMATICS STATE MODELS

F.1 First State Algorithm

The first state algorithm computes the change in actuator length from the induced moments of the upper stages. The actuator lengths are assumed to remain perpendicular to the support plates regardless of the induced module rotation, $\gamma = 90°$. From Figure 5-4, the maximum tensile force of the actuator in the martensite phase is $Fu^{max} = 0.35\text{N}$. The constitutive SMA model has shown that the actuator exhibits similar responses to compressive strains therefore $Fu^{min} = -0.35\text{N}$.

Prior to application of the bending moments, it is assumed that the actuators are exerting the maximum tensile force on the support plates and that they can compress to the minimum value of Fu^{min}. Larger moments would result in the buckling of the unit module. The analysis of the first state algorithm is divided into two cases: positive and negative x-axis moments. In the case of a positive moment in the x-axis, the free-body diagram of the unit module in the y-z plane is given by:

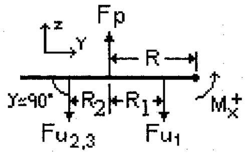

Figure A-5: Unit module free body diagram in y-z plane

The resulting moment balance equation is given by:

$$Fu_{2,3} = \frac{F_P R - F_{u1}(R - R_1) - M_X}{2R + R_2} \tag{A-2}$$

Although this relation is theoretically correct, numerically calculations have shown that the change in the un-actuated force, $\Delta Fu_{2,3}$, can be better approximated by (A-3). This relation assumes that induced moment Mx is sustained primarily by the change in force $\Delta Fu_{2,3}$ accompanied by the change in length $\Delta Lu_{2,3}$. The effects of ΔFu_1 are neglected due to the proximity of the actuator to the center of rotation.

$$\Delta Fu_{2,3} = \frac{-M_X}{2R + R_2} \tag{A-3}$$

And

$$Fu_{2,3}^{i} = Fu_{2,3}^{\max} + \Delta Fu_{2,3} \tag{A-4}$$

The actuator length is then given by:

$$Lu_{2,3}^{i} = \frac{Fu_{2,3}^{i}}{E_m} + L_{0m} \tag{A-5}$$

Actuators 2 and 3 also sustain the induced y-axis moment. In this frame, the center of rotation of the free-body diagram in the x-z plane is located at the center of the module.

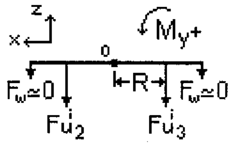

Figure A-6: Unit module free body diagram in x-z plane

From symmetry, the un-actuated forces, $Fu_{2,3}{}^{i}$, are eliminated from moment balance equation and the resulting relation is given by:

$$\Delta Fu_{2,3}^{ii} = \frac{M_Y}{2R} \tag{A-6}$$

If the moment in the y-axis is greater than in the x-axis, one of the final lengths, $Lu_2{}^{ii}$ *or* $Lu_3{}^{ii}$, may be greater the maximum actuator length of 30mm. In this case, one of the actuators is assumed to exert the maximum output force of 0.35N and the moment balance equation becomes:

$$\Delta Fu_{2,3}^{ii} = Fu_{2,3}^{i} - Fu^{\max} + {M_Y}/{R} \tag{A-7}$$

In the case of a negative *Mx* the center of rotation is located on the opposite side of the support plate. Again, it is assumed that the negative moment is sustained primarily by the change in force ΔFu_1.

$$\Delta Fu_1 = \frac{M_X}{R + R_a} \tag{A-8}$$

And

$$Fu_1^i = Fu_1^{\max} + \Delta Fu_1 \tag{A-9}$$

The actuator length is then given by:

$$Lu_1^i = \frac{Fu_1^i}{E_m} + L_{0m} \tag{A-10}$$

In this case, both actuators 2 and 3 are stretched to their maximum lengths therefore one of these actuators is exerting the maximum output force of 0.35N. The free-body diagram is similar to Figure A-6 and the moment balance equation becomes:

$$Fu_{2,3}^i = Fu^{\max} - M_Y/R \tag{A-11}$$

And

$$Lu_{2,3}^i = \frac{Fu_{2,3}^i}{E_m} + L_{0m} \tag{A-12}$$

The applied moments generate a rotation in the unit module according to the actuator lengths computed above. It is assume that, regardless of the magnitude of the moments, there is a location at which the bellows is fully extended. This location is represented by the vector *H* and is described by the angle theta in Figure A-7.

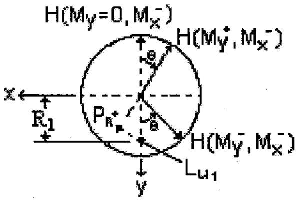

Figure A-7: Moment induced rotation change

For the basis of this study, theta is expressed by the ratio of the x and y-axis moments.

$$\theta = \tan^{-1}\left(\frac{M_Y}{M_X}\right) \qquad \textbf{(A-13)}$$

The shortest actuator length is used to determine the induced rotation of the unit module. In the first case this length is Lu_2^{ii} and in the second case is the shortest length between $Lu_{2,3}^{i}$ and Lu_1^{i}. The unit module inclination angle α was found by replacing R_1 in (5-2) with the projected length P_R, given by:

$$P_R = R_1 \cos\theta \qquad \textbf{(A-14)}$$

The rotation matrix within the homogeneous transformation matrix of the unit module is obtained using the rotational conversion presented above and the translation components are given as:

$$
\begin{aligned}
x^i &= D_h \sin\theta \\
y^i &= D_h \cos\theta \\
z^i &= L - D_z
\end{aligned}
\tag{A-15}
$$

F.2 Second State Algorithm

Several approximations were made to simplify the coding of the second state algorithm and all other state algorithms involving one or two actuated SMAs. The angle γ between the actuator lengths and the support plates is evaluated at the previous stage for both the single and double actuated cases. The gamma angles computed in the first iteration are used in the second iteration. For states 2, 3 and 4, $\gamma = 1.19$ radians and for states 5, 6 and 7, $\gamma = 0.89$ radians. Applying the local moments, the free body diagram of the unit module cross-section in the y-z plane is used to determine the actual length of the activated actuator.

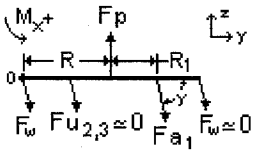

Figure A-8: Unit module free body diagram in y-z plane

It is assumed that at this stage the reaction forces of the un-actuated SMAs are negligible compared to the force of the actuated SMAs. It is also assumed that the force exerted by the bellows on the activated side of the module is negligible. With these assumptions, the moment balance is given by:

$$
Fa_1 = \frac{F_P R + M_X}{\cos\gamma (R + R_1)} \tag{A-16}
$$

Using the austenite elastic modulus derived in Figure 5-4 and the initial actuator length specified in chapter 5, the actuator length is obtained from:

$$La = Fa/E_A + L_{0A} \tag{A-17}$$

The effect of the y-axis moment is obtained from the free-body diagram of unit module cross-section in the x-z plane.

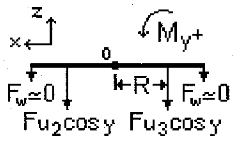

Figure A-9: Unit module free body diagram in x-z plane

Again the forces exerted by the bellows is assumed to be negligible and the applied moment, M_Y, is sustained entirely by the un-actuated SMAs. Since it is also assumed that the initial forces F_{u2} and F_{u3} are negligible, only the change in length is considered in the moment balance equation.

$$0 = M_Y + R(Fu_2 - E_M \Delta Lu_2)\cos\gamma - R(Fu_3 + E_M \Delta Lu_3)\cos\gamma \tag{A-18}$$

Assuming the change in length remains small, the following approximation can be made: $\Delta Lu_2 = \Delta Lu_3 = \Delta Lu$ and (A-18) is reduced to:

$$\Delta Lu = \frac{M_Y}{2E_M R\cos\gamma} \tag{A-19}$$

Applied moments will cause a shift in the rotation angle of the unit module. An analogy similar to that of the first state algorithm is used to determine the percentage of induced rotation. However, a sinusoidal function is used to model the location of the H vector based on the difference between the un-actuated and the actuated lengths.

$$\theta = \frac{\pi}{3}\sin\left[\frac{\pi}{2}\left(\frac{\Delta Lu}{La - Lu}\right)\right] \tag{A-20}$$

The rotation matrix and translation components for states 2 to 7 are obtained using the same methodology as in the first state algorithm.

F.3 Eighth State Algorithm

The eighth state algorithm computes the change in actuator length from the case of a fully actuated unit module. The initial actuator length is determined based the difference between the pressure force and the weight of the previous modules, F_w. Again, the actuator lengths are assumed to remain perpendicular to the support plates.

$$Fa_{1,2,3}^{i} = (F_P - F_W)/3 \tag{A-21}$$

As with the other states, the effects of M_x on the actuator length was determined then adjusted according to M_Y. The change in actuator length due to M_x is obtained from the free-body diagram Figure A-10. It was assumed that the forces exerted by the bellows wall were negligible.

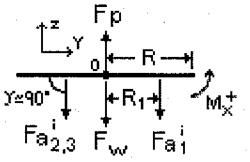

Figure A-10: Unit module free body diagram in y-z plane

The following relation is valid assuming the change in lengths remains small:

$$\Delta Lx_1^i = -2\Delta Lx_{2,3}^i \tag{A-22}$$

The initial actuator forces, $Fa_{1,2,3}{}^i$, are equal and can be eliminated from the moment balance equation resulting in a function of $\Delta Lx_{2,3}{}^i$.

$$\Delta Lx^{i}_{2,3} = \frac{M_X}{3E_A R_1} \tag{A-23}$$

The corresponding forces are given by:

$$\begin{aligned} Fa^{ii}_{2,3} &= Fa^{i}_{2,3} - \Delta Lx^{i}_{2,3} \\ Fa^{ii}_{1} &= Fa^{i}_{1} - \Delta Lx^{i}_{1} \end{aligned} \tag{A-24}$$

The effect of the local moment in the y-axis is obtained from the free-body diagram of unit module cross-section in the x-z plane.

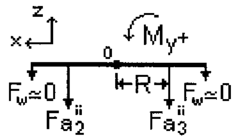

Figure A-11: Unit module free body diagram in x-z plane

The actuator forces of the first iteration, $Fa_{2,3}{}^{i}$, are also equal and can be eliminated from the moment balance equation. The resulting equation is simply a function of $\Delta Lx_{2,3}{}^{ii}$ and is given by:

$$\Delta Ly^{ii}_{2,3} = \frac{M_Y}{2E_A R} \tag{A-25}$$

As opposed to the other seven states, the bellows is compressed along the entire circumference of the vertebra. However, the same analogy is applied to obtain the modified homogeneous transformation matrix. The *H* vector is used to locate the highest or most stretch-out point of the bellows and is determined based on the ratio of the two moments.

$$\theta = \tan^{-1}\left(\frac{M_Y}{M_X}\right) \tag{A-26}$$

The H vector and the actuator location projections, P_L, for a negative x-direction moment and a positive y-direction moment are represented in Figure A-12.

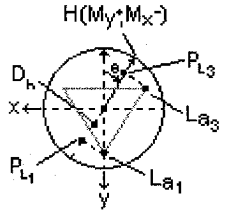

Figure A-12: Moment induced rotation change

The actuator location projections are obtained based on the angle theta and the actuator lengths are adjusted using the ΔLs computed above.

$$\begin{aligned} La_1^{ii} &= La_{1,2,3}^{i} + \Delta Lx_1^{i} \\ La_{2,3}^{iii} &= La_{1,2,3}^{i} - \Delta Lx_{2,3}^{i} - \Delta Ly_{2,3}^{ii} \end{aligned} \tag{A-27}$$

The rotation matrix and displacement terms are found using the same algorithm as the other seven cases.

APPENDIX G – REFINED FORWARD KINEMATICS ALGORITHM

Following the computation of all the manipulator configurations, the end-effector end-point positions are saved and stored (to be used by the inverse kinematics algorithm).

Code 13: Refined Forward Kinematics Main

```
function MainKinematics;

clear all;
clear variables;

W = 0.029; %N
LoA = 8.3; LoM = 25.5; L = 30; %mm
R1 = 6; R2 = 10; %mm
Ea = 0.34; Em = 0.356; %N/mm
Fp = 5.4; %N

[Ai,Aii,Aiii,Aiv,disp0,type] = Point_Cloud(R1,R2,L);

for i=1:2

    for w=1:4096

        type4 = Aiv(4,5,w);
        %----------------------- Unit module #3 ------------------------
        A4 =
Ai(1:4,1:4,w)*Aii(1:4,1:4,w)*Aiii(1:4,1:4,w)*Aiv(1:4,1:4,w);
        A3 = Ai(1:4,1:4,w)*Aii(1:4,1:4,w)*Aiii(1:4,1:4,w);

        Rot = A3(1:3,1:3);
        Fvert = inv(Rot)*[0;0;-W];
        dX = inv(Rot)*[(A4(1,4)-A3(1,4));(A4(2,4)-A3(2,4));(A4(3,4)-
A3(3,4))];
        Fw = Fvert(3);
        type3 = Aiii(3,5,w);
```

```
        Aiii(1:4,1:4,w) =
CaseSelector(dX,Fvert,Rot,Fp,Fw,LoM,LoA,L,R2,R1,Ea,Em,type3);

        %----------------------- Unit module #2 -----------------------
        A4 =
Ai(1:4,1:4,w)*Aii(1:4,1:4,w)*Aiii(1:4,1:4,w)*Aiv(1:4,1:4,w);
        A3 = Ai(1:4,1:4,w)*Aii(1:4,1:4,w)*Aiii(1:4,1:4,w);
        A2 = Ai(1:4,1:4,w)*Aii(1:4,1:4,w);

        Rot = A2(1:3,1:3);
        Fvert = inv(Rot)*[0;0;-W];
        dX = inv(Rot)*[(A4(1,4)+A3(1,4)-2*A2(1,4));(A4(2,4)+A3(2,4)-
2*A2(2,4));(A4(3,4)+A3(3,4)-2*A2(3,4))];
        Fw = 2*Fvert(3);
        type2 = Aii(2,5,w);

        Aii(1:4,1:4,w) =
CaseSelector(dX,Fvert,Rot,Fp,Fw,LoM,LoA,L,R2,R1,Ea,Em,type2);

        %----------------------- Unit module #1 -----------------------
        A4 =
Ai(1:4,1:4,w)*Aii(1:4,1:4,w)*Aiii(1:4,1:4,w)*Aiv(1:4,1:4,w);
        A3 = Ai(1:4,1:4,w)*Aii(1:4,1:4,w)*Aiii(1:4,1:4,w);
        A2 = Ai(1:4,1:4,w)*Aii(1:4,1:4,w);
        A1 = Ai(1:4,1:4,w);

        Rot = A1(1:3,1:3);
        Fvert = inv(Rot)*[0;0;-W];
        dX = inv(Rot)*[(A4(1,4)+A3(1,4)+A2(1,4)-
3*A1(1,4));(A2(2,4)+A3(2,4)+A4(2,4)-
3*A1(2,4));(A2(3,4)+A3(3,4)+A4(3,4)-3*A1(3,4))];
        Fw = 3*Fvert(3);
        type1 = Ai(1,5,w);

        Ai(1:4,1:4,w) =
CaseSelector(dX,Fvert,Rot,Fp,Fw,LoM,LoA,L,R2,R1,Ea,Em,type1);
```

```
        %------------------------ A matrix ---------------------------

        A4 =
Ai(1:4,1:4,w)*Aii(1:4,1:4,w)*Aiii(1:4,1:4,w)*Aiv(1:4,1:4,w);
        Amatrix(1:4,1:5,w) = horzcat(A4,[type1;type2;type3;type4]);
        disp(w,1:3)=Amatrix(1:3,4,w);
    end

    D(:,1:3,i)=disp(:,1:3);

end

D(:,1:3)=D(:,1:3,2);
for w=1:4096
    displacement(w,1:7) = horzcat(D(w,1:3),type(w,1:4));
end

save displacement;
plot3(D(:,1,1),D(:,2,1),D(:,3,1),'k.',D(:,1,2),D(:,2,2),D(:,3,2),'b.',d
isp0(:,1),disp0(:,2),disp0(:,3),'r.')
```

Code 14: Case Selector

```
function newA =
CaseSelector(dX,Fvert,Rot,Fp,Fw,LoM,LoA,L,R2,R1,Ea,Em,type);

if type==1
    newA=case000(dX,Fvert,Rot,Fp,Fw,LoM,L,R2,R1,Ea,Em);
elseif type==2
    newA=case100(dX,Fvert,Rot,Fp,Fw,LoA,L,R2,R1,Ea,Em);
elseif type==3
    newA=case010(dX,Fvert,Rot,Fp,Fw,LoA,L,R2,R1,Ea,Em);
elseif type==4
    newA=case001(dX,Fvert,Rot,Fp,Fw,LoA,L,R2,R1,Ea,Em);
elseif type==5
    newA=case011(dX,Fvert,Rot,Fp,Fw,LoA,L,R2,R1,Ea,Em);
elseif type==6
    newA=case101(dX,Fvert,Rot,Fp,Fw,LoA,L,R2,R1,Ea,Em);
```

```
elseif type==7
    newA=case110(dX,Fvert,Rot,Fp,Fw,LoA,L,R2,R1,Ea,Em);
elseif type==8
    newA=case111(dX,Fvert,Rot,Fp,Fw,LoA,L,R2,R1,Ea,Em);
else
    error('kicking ass is for the other guy');
end
```

Code 15: Length Computation for Each Unit-Module Configuration

```
function newA=case000(dX,Fvert,Rot,Fp,Fw,LoM,L,R2,R1,Ea,Em);

% 0) Constants Fmax: initial actuator force
Fmax = 1.602; %average maximum actuator force in martensite phase

% 1) Convert Mglobal to Mlocal ------ M = [Mx;My;0]
Mlocal = cross(dX,Fvert);

%------------------------------- Mx+ ----------------------------------
if Mlocal(1)>=0
% 2) Compute force of affected actuators due to Mx(reduced in length)
    dFun23 = -Mlocal(1)/(2*R2+R1);
    Lun23 = (dFun23+Fmax)/Em + LoM;

% 3) Compute change in length due to My
    dLy = abs(Mlocal(2))/(2*Em*R1*cos(pi/6));

    if (Lun23 + dLy) >= L
        dLy = (dFun23+Fmax - Fmax + abs(Mlocal(2))/R1/cos(pi/6))/Em;
    end
    Lmin = Lun23 - dLy;

% 4) Find moment induced rotation direction change and length
projection
    if Mlocal(1)~=0 & Mlocal(2)~=0
        theta = pi/2*Mlocal(2)/(abs(Mlocal(1))+abs(Mlocal(2)));
    else
        theta = 0;
```

```
    end
    P123 = R1*cos(pi/3-abs(theta));

    [alpha,Dh,Dz] = angle(Lmin,P123,L,R2,L);
    a = alpha;
    t = theta;
    X = Dh*sin(t);
    Y = -Dh*cos(t);

%-------------------------------- Mx- -------------------------------------
else
% 5) Compute force of affected actuators due to Mx(reduced in length)
    dFun1 = Mlocal(1)/(R2+R1);
    Lun1 = (Fmax+dFun1)/Em + LoM;

% 6) Compute forces due to My
    Fun23 = (Fmax*R1*cos(pi/6)-abs(Mlocal(2)))/(R1*cos(pi/6));
    Lun23 = Fun23/Em + LoM;

% 7) Find moment induced rotation along z
    if Mlocal(1)~=0 & Mlocal(2)~=0
        theta = pi/2*Mlocal(2)/(abs(Mlocal(1))+abs(Mlocal(2)));
    else
        theta = 0;
    end

% 8) Check to find smallest length
    if Lun1 <= Lun23
        Lmin = Lun1;
        Plmin = R1*cos(theta);
    else
        Lmin = Lun23;
        Plmin = R1*cos(2*pi/3-abs(theta));
    end

% 9) Find moment induced rotation direction change and length
projection
    [alpha,Dh,Dz] = angle(Lmin,Plmin,L,R2,L);
```

```
    a = -alpha;
    t = -theta;
    X = Dh*sin(t);
    Y = Dh*cos(t);

end
%--------------------------- Rotation Matrix --------------------------

R = AxisAngle(t,a);
Z = L-Dz;

newA = [R(1,1) R(1,2) R(1,3) X;R(2,1) R(2,2) R(2,3) Y;R(3,1) R(3,2)
R(3,3) Z;0 0 0 1];
%--------------------------------- end  -------------------------------



function newA = case001(dX,Fvert,Rot,Fp,Fw,Lo,L,R2,R1,Ea,Em);

% 0) Constants
Gamma = 0.38; %angle gamma between actuator and vertical axis
Mz = [cos(2*pi/3) -sin(2*pi/3) 0;sin(2*pi/3) cos(2*pi/3) 0;0 0 1];

% 1) Convert Mglobal to Mlocal ------ M = [Mx;My;0]
dXlocal = inv(Mz)*dX;
Fvert = inv(Mz)*Fvert;
Mlocal = cross(dXlocal,Fvert);


% 2) Find actuator#2 force and length
Fa = (Fp*R2 + Mlocal(1)) / (R1+R2) / cos(Gamma);
La = Fa/Ea + Lo;

% 3) Get unactuated length l1 and l2 from shape function
Da = R1;
Du = R1/2;
Lu = La + (Da+Du)*(L-La)/(R2+Da);

% 4) Compute change in length of unactuated side due to My
```

```
dLu = abs(Mlocal(2))/(Em*R1*cos(pi/6));

% 5) Find moment induced rotation direction change and length
projection
theta = pi/3*sin(pi/2*(dLu/(Lu-La)));
Pl3 = R1*cos(theta);

% 6) Get unit module rotation and displacement
[alpha,Dh,Dz] = angle(La,Pl3,L,R2,L);

a = -alpha;
if Mlocal(2)>=0
    t = theta;
else
    t = -theta;
end

R = AxisAngle(2*pi/3-t,a);
X = -Dh*cos(pi/6-t);
Y = -Dh*sin(pi/6-t);
Z = L-Dz;

newA = [R(1,1) R(1,2) R(1,3) X;R(2,1) R(2,2) R(2,3) Y;R(3,1) R(3,2)
R(3,3) Z;0 0 0 1];
%---------------------------------- end ---------------------------------


function newA=case010(dX,Fvert,Rot,Fp,Fw,Lo,L,R2,R1,Ea,Em);

% 0) Constants
Gamma = 0.38; %angle gamma between actuator and vertical axis
Mz = [cos(-2*pi/3) -sin(-2*pi/3) 0;sin(-2*pi/3) cos(-2*pi/3) 0;0 0 1];

% 1) Convert Mglobal to Mlocal ------ M = [Mx;My;0]
dXlocal = inv(Mz)*dX;
Fvert = inv(Mz)*Fvert;
Mlocal = cross(dXlocal,Fvert);
```

```
% 2) Find actuator#2 force and length
Fa = (Fp*R2 + Mlocal(1)) / (R1+R2) / cos(Gamma);
La = Fa/Ea + Lo;

% 3) Get unactuated length l1 and l3 from shape function
Da = R1;
Du = R1/2;
Lu = La + (Da+Du)*(L-La)/(R2+Da);

% 4) Compute change in length of unactuated side due to My
dLu = abs(Mlocal(2))/(Em*R1*cos(pi/6));

% 5) Find moment induced rotation direction change and length
projection
theta = pi/3*sin(pi/2*(dLu/(Lu-La)));
Pl3 = R1*cos(theta);

% 6) Get unit module rotation and displacement
[alpha,Dh,Dz] = angle(La,Pl3,L,R2,L);

a = -alpha;
if Mlocal(2)>=0
    t = theta;
else
    t = -theta;
end

R = AxisAngle(-2*pi/3-t,a);
X = Dh*cos(pi/6+t);
Y = -Dh*sin(pi/6+t);
Z = L-Dz;

newA = [R(1,1) R(1,2) R(1,3) X;R(2,1) R(2,2) R(2,3) Y;R(3,1) R(3,2)
R(3,3) Z;0 0 0 1];
%-------------------------------- end --------------------------------


function newA=case100(dX,Fvert,Rot,Fp,Fw,Lo,L,R2,R1,Ea,Em);
```

```
% 0) Constants
Gamma = 0.38; %angle gamma between actuator and vertical axis

% 1) Convert Mglobal to Mlocal ------ M = [Mx;My;0]
Mlocal = cross(dX,Fvert);



% 2) Find actuator#2 force and length
Fa = (Fp*R2 + Mlocal(1)) / (R1+R2) / cos(Gamma);
La = Fa/Ea + Lo;

% 3) Get unactuated length l1 and l3 from shape function
Da = R1;
Du = R1/2;
Lu = La + (Da+Du)*(L-La)/(R2+Da);

% 4) Compute change in length of unactuated side due to My
dLu = abs(Mlocal(2))/(Em*R1*cos(pi/6));

% 5) Find moment induced rotation direction change and length
projection
theta = pi/3*sin(pi/2*(dLu/(Lu-La)));
Pl3 = R1*cos(theta);

% 6) Get unit module rotation and displacement
[alpha,Dh,Dz] = angle(La,Pl3,L,R2,L);

a = -alpha;
if Mlocal(2)>=0
    t = theta;
else
    t = -theta;
end

R = AxisAngle(-t,a);
X = Dh*sin(t);
Y = Dh*cos(t);
```

```
Z = L-Dz;

newA = [R(1,1) R(1,2) R(1,3) X;R(2,1) R(2,2) R(2,3) Y;R(3,1) R(3,2)
R(3,3) Z;0 0 0 1];
%-------------------------------- end ---------------------------------


function newA=case110(dX,Fvert,Rot,Fp,Fw,Lo,L,R2,R1,Ea,Em);

% 0) Constants
Gamma = 0.64; %angle gamma between actuator and vertical axis
Mz = [cos(2*pi/3) -sin(2*pi/3) 0;sin(2*pi/3) cos(2*pi/3) 0;0 0 1];

% 1) Convert Mglobal to Mlocal ------ M = [Mx;My;0]
dXlocal = inv(Mz)*dX;
Fvert = inv(Mz)*Fvert;
Mlocal = cross(dXlocal,Fvert);

% 2) Find actuator#1 & #2 force and length
Fa = (Fp*R2 - Mlocal(1)) / (R1+2*R2) / cos(Gamma);
La = Fa/Ea + Lo;

% 3) Get unactuated length l3 from shape function
Da = R1/2;
Du = R1;
Lu = La + (Da+Du)*(L-La)/(R2+Da);

% 4) Compute change in length of actuated side due to My
dLa = abs(Mlocal(2))/(2*Ea*R1*cos(pi/6));

% 5) Find moment induced rotation direction change and length
projection
theta = pi/3*sin(pi/2*(dLa/(Lu-La)));
Pl = R1*cos(pi/3-theta);

% 6) Get unit module rotation and displacement
La = La - dLa;
[alpha,Dh,Dz] = angle(La,Pl,L,R2,L);
```

```
a = alpha;
if Mlocal(2)>=0
    t = theta;
else
    t = -theta;
end

R = AxisAngle(2*pi/3+t,a);
X = Dh*cos(pi/6+t);
Y = Dh*sin(pi/6+t);
Z = L-Dz;

newA = [R(1,1) R(1,2) R(1,3) X;R(2,1) R(2,2) R(2,3) Y;R(3,1) R(3,2)
R(3,3) Z;0 0 0 1];
%--------------------------------- end  --------------------------------



function newA=case101(dX,Fvert,Rot,Fp,Fw,Lo,L,R2,R1,Ea,Em);

% 0) Constants
Gamma = 0.64; %angle gamma between actuator and vertical axis
Mz = [cos(-2*pi/3) -sin(-2*pi/3) 0;sin(-2*pi/3) cos(-2*pi/3) 0;0 0 1];

% 1) Moment convertion to rotated axe
dXlocal = inv(Mz)*dX;
Fvert = inv(Mz)*Fvert;
Mlocal = cross(dXlocal,Fvert);

% 2) Find actuator#1 & #3 force and length
Fa = (Fp*R2 - Mlocal(1)) / (R1+2*R2) / cos(Gamma);
La = Fa/Ea + Lo;

% 3) Get unactuated length l2 from shape function
Da = R1/2;
Du = R1;
Lu = La + (Da+Du)*(L-La)/(R2+Da);
```

```
% 4) Compute change in length of actuated side due to My
dLa = abs(Mlocal(2))/(2*Ea*R1*cos(pi/6));

% 5) Find moment induced rotation direction change and length
projection
theta = pi/3*sin(pi/2*(dLa/(Lu-La)));
Pl = R1*cos(pi/3-theta);

% 6) Get unit module rotation and displacement
La = La - dLa;
[alpha,Dh,Dz] = angle(La,Pl,L,R2,L);

a = alpha;
if Mlocal(2)>=0
    t = theta;
else
    t = -theta;
end

R = AxisAngle(-2*pi/3+t,a);
X = -Dh*cos(pi/6-t);
Y = Dh*sin(pi/6-t);
Z = L-Dz;

newA = [R(1,1) R(1,2) R(1,3) X;R(2,1) R(2,2) R(2,3) Y;R(3,1) R(3,2)
R(3,3) Z;0 0 0 1];
%--------------------------------- end --------------------------------


function newA=case011(dX,Fvert,Rot,Fp,Fw,Lo,L,R2,R1,Ea,Em);

% 0) Constants
Gamma = 0.64; %angle gamma between actuator and vertical axis

% 1) Convert Mglobal to Mlocal ------ M = [Mx;My;0]
Mlocal = cross(dX,Fvert);

% 2) Find actuator#2 & #3 force and length
```

```
Fa = (Fp*R2 - Mlocal(1)) / (R1+2*R2) / cos(Gamma);
La = Fa/Ea + Lo;

% 3) Get unactuated length l1 from shape function
Da = R1/2;
Du = R1;
Lu = La + (Da+Du)*(L-La)/(R2+Da);

% 4) Compute change in length of actuated side due to My
dLa = abs(Mlocal(2))/(2*Ea*R1*cos(pi/6));

% 5) Find moment induced rotation direction change and length
projection
theta = pi/3*sin(pi/2*(dLa/(Lu-La)));
Pl = R1*cos(pi/3-theta);

% 6) Get unit module rotation and displacement
La = La - dLa;
[alpha,Dh,Dz] = angle(La,Pl,L,R2,L);

a = alpha;
if Mlocal(2)>=0
    t = theta;
else
    t = -theta;
end

R = AxisAngle(t,a);
X = Dh*sin(t);
Y = -Dh*cos(t);
Z = L-Dz;

newA = [R(1,1) R(1,2) R(1,3) X;R(2,1) R(2,2) R(2,3) Y;R(3,1) R(3,2)
R(3,3) Z;0 0 0 1];
%--------------------------------- end ---------------------------------


function newA=case111(dX,Fvert,Rot,Fp,Fw,LoA,L,R2,R1,Ea,Em);
```

```
% 0) Get initial actuation forces
Fa = (Fp - Fw)/3;
La = Fa/Ea + LoA;

% 1) Get local moment
Mlocal = cross(dX,Fvert);

% 2) Compute change in length due to Mx
dLx23 = abs(Mlocal(1))/(3*Ea*R1);
dLx1 = 2*dLx23;

% 3) Compute change in length due to My
dLy = abs(Mlocal(2))/(2*Ea*R1*cos(pi/6));

% 5) Find moment induced rotation direction change and length
projection
if Mlocal(1)>0
    theta = atan(Mlocal(2)/abs(Mlocal(1)));
else
    theta=0;
end
Pl1 = R1*cos(theta);
Pl23 = R1*cos(pi/6-abs(theta));

% 6) Get unit module rotation and displacement
if Mlocal(1)>=0
    l1 = La + dLx1;
    l23 = La - dLx23 - dLy;
    [alpha,Dh,Dz] = angle(l23,Pl23,l1,Pl1,L);
    a = alpha;
    t = theta;
    X = Dh*sin(t);
    Y = -Dh*cos(t);
else
    l1 = La - dLx1;
    l23 = La + dLx23 + dLy;
    [alpha,Dh,Dz] = angle(l1,Pl1,l23,Pl23,L);
```

```
    a = -alpha;
    t = -theta;
    X = Dh*sin(-t);
    Y = Dh*cos(-t);
end

R = AxisAngle(t,a);
Z = L-Dz;

newA = [R(1,1) R(1,2) R(1,3) X;R(2,1) R(2,2) R(2,3) Y;R(3,1) R(3,2)
R(3,3) Z;0 0 0 1];
%-------------------------------- end --------------------------------
```

Code 16: Inclination Angle Computation

```
function [alpha,Dh,Dz] = angle(L2,D2,L1,D1,L)

alpha = -atan((-L1^2+2*L1*L2-
L2^2+4*D1^2+8*D1*D2+4*D2^2)^(1/2)/(D1+D2)^2*(L1-L2)/(-2*D2^2-2*D1^2-
4*D1*D2+L1^2-2*L1*L2+L2^2)*(D1^2+2*D1*D2+D2^2));

if L2~=L1
    gamma = acos((D2+D1)/(L2-L1)*(cos(alpha)-1));
else
    gamma = pi/2;
end

Dh = L1*cos(gamma) + D1*(cos(alpha)-1);

Dz = L - L1*sin(gamma) + D1*sin(alpha);
```

APPENDIX H – INVERSE KINEMATICS ALGORITHM

The inverse kinematics algorithm is simply composed of a sort and search program, which arranges the 4096 manipulator configurations in ascending z-axis order and stores the values in *Zdisplacement.* The Program outputs the closest point(s) along with the respective state of each unit-module. The Matlab controller then uses this information to send to the SMA drivers.

Code 17: Inverse Kinematics Main

```
function [OutputType,error] = InverseKinematics

load Zdisplacement;

k = menu('Select a Displacement Type','Point','Line');

if k==1
    Dpoint = input('Select a point [-50<X<50 -50<Y<50 -30<Z<120]= ')';
    simulationtime = input('Select the simulation time period = ');
    [Mpoints,errormin]=SimpleSearch(Zdisplacement,Dpoint);
    error = errormin;

    for i=1:simulationtime
        OutputType(i,1:5) = [i-1 Zdisplacement(Mpoints(1),4)
Zdisplacement(Mpoints(1),5) Zdisplacement(Mpoints(1),6)
Zdisplacement(Mpoints(1),7)];
    end
    OutputType(i+1,1:5) = [i 1 1 1 1];
end

if k==2
    StartP = input('Select a start point [-50<X<50 -50<Y<50 -30<Z<120]
= ');
    EndP = input('Select an end point [-50<X<50 -50<Y<50 -30<Z<120] =
');
```

```
    Npoints = input('Select the number of points on the line (min 2) =
');
    simulationstep = input('Select the actuator switch time period =
');

    A = [(EndP(1)-StartP(1)) (EndP(2)-StartP(2)) (EndP(3)-StartP(3))];

    j0=1;
    for i=1:Npoints
        Dpoint(i,1:3)= A*(i-1)/(Npoints-1)+StartP;
        [Mpoints,errormin]=SimpleSearch(Zdisplacement,Dpoint(i,1:3));
        error(i)=errormin;

        for j=j0:(simulationstep+j0-1)
            OutputType(j,1:5) = [j-1 Zdisplacement(Mpoints(1),4)
Zdisplacement(Mpoints(1),5) Zdisplacement(Mpoints(1),6)
Zdisplacement(Mpoints(1),7)];
        end
        j0=j+1;
    end
    OutputType(j0,1:5) = [j0-1 1 1 1 1];
end
```

Code 18: Search Algorithm

```
function [points,errormin] = SimpleSearch(Z,D)

Zdisplacement = sortrows(displacement,[3 2 1]);

mincounter = 1;
samecounter = 0;
X=[];

errormin = sqrt((Z(1,1)-D(1))^2+(Z(1,2)-D(2))^2+(Z(1,3)-D(3))^2);

for i=2:4096
    error = sqrt((Z(i,1)-D(1))^2+(Z(i,2)-D(2))^2+(Z(i,3)-D(3))^2);
    if error==errormin
        samecounter = samecounter + 1;
```

```
        X(samecounter,1:2)=[i mincounter];
    end
    if error<errormin
        errormin = error;
        mincounter = i;
    end
end

j=1;
points(j)=mincounter;
if isempty(X)~=1
    while X(samecounter,2)== mincounter
        j=j+1;
        points(j)=X(samecounter,1);
        samecounter = samecounter-1;
    end
end
```

APPENDIX I – ACTUATOR CONTROLLER BLOCK DIAGRAMS

The type to actuator sub-model uses the manipulator configuration information to determine the state of each actuator (*on* or *off*).

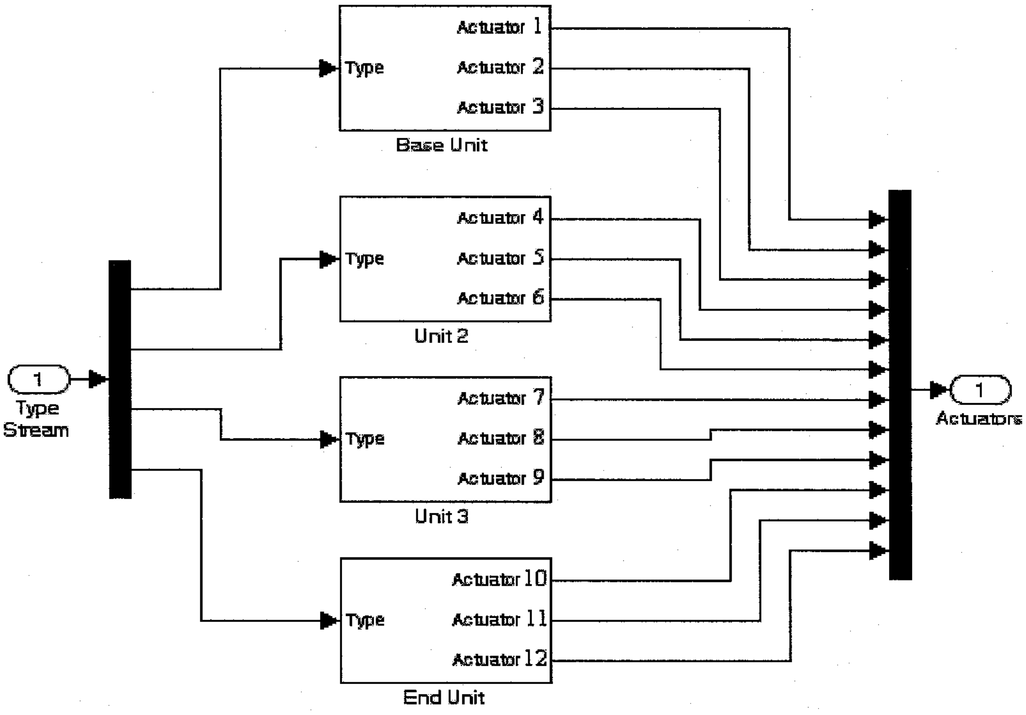

Figure A-13: Manipulator configuration to actuator converter

The actuator to matrix sub-model piggybacks the actuator states onto phase-delayed pulses to be sent to the Q8 analog outputs.

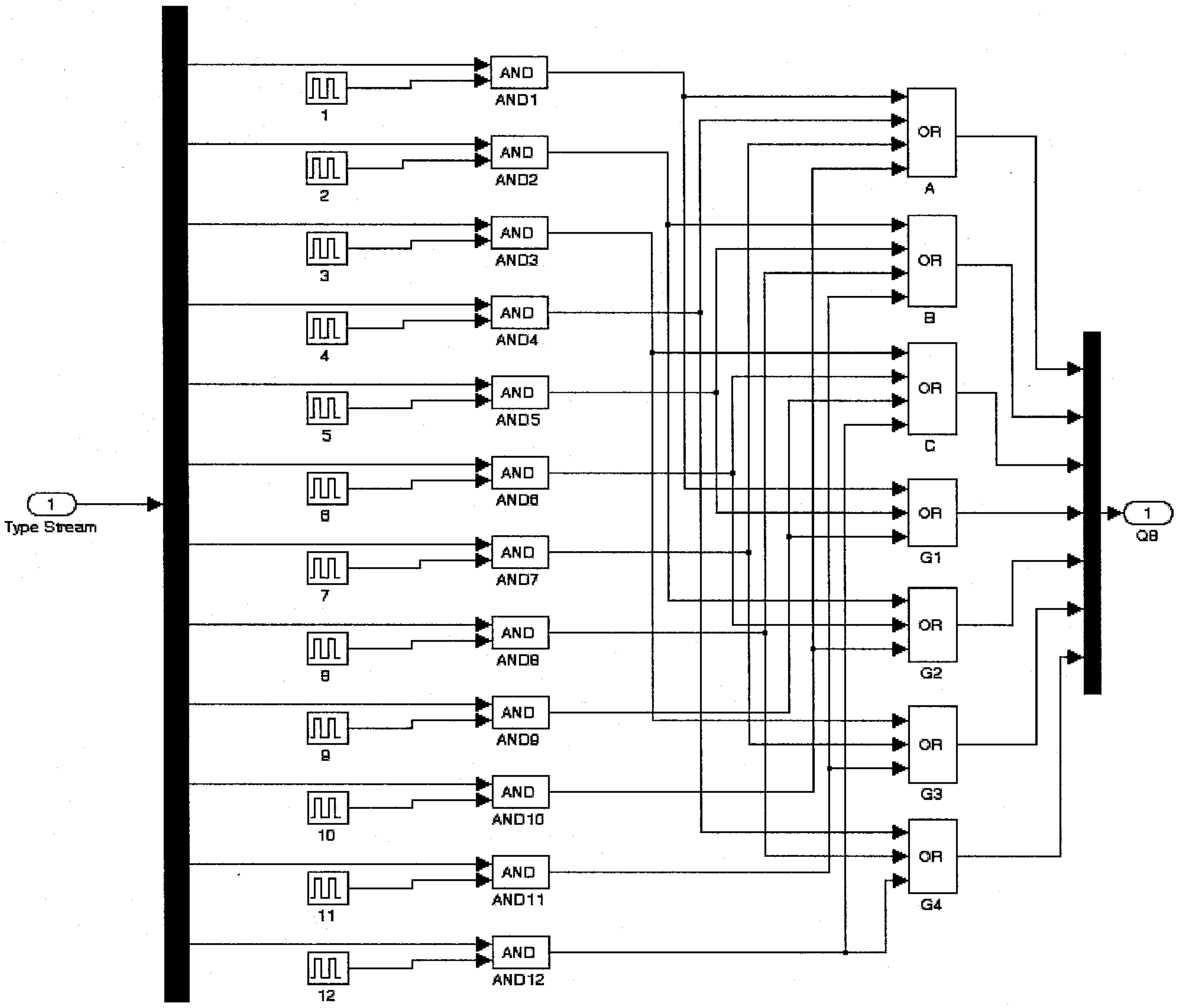

Figure A-14: Actuator to matrix converter

APPENDIX J – ACTUATOR HEAT TRANSFER COEFFICIENT APPROXIMATION

The convective heat transfer coefficient for the proposed actuator is estimated based on the vertical flat plate model cited in reference [19]. The average heat transfer coefficient is based on several dimensionless groups, namely the Prandtl, Grashof and Nusselt numbers. The Prandtl number *Pr* is the ratio between the kinematic viscosity υ and the thermal diffusivity α of air at the ambient temperature of 27°C.

$$\Pr = \upsilon/\alpha = \frac{15.69e^{-6}\ m^2/s}{0.2216e^{-4}\ m^2/s} = 0.708 \tag{A-28}$$

The Grashof number Gr_x is dependant on the length of the vertical plate. This length is assumed to be equal to the total length of all the circular sections in the actuator since these sections have a considerably larger resistance than the flat section therefore they will generate and dissipate the majority of the heat produced. Based on the CAD model of the actuator, the total length of all the circular sections is equal to 14.3mm. The Grashof number is given by:

$$Gr_{x=L} = \frac{g\beta(T_{actuator} - T_\infty)L^3}{\upsilon^2} = \frac{(9.81\,m/s^2)(3.03e^{-3}K^{-1})(360K - 300K)(0.0143m)^3}{(15.69e^{-6}\ m/s^2)^2} = 2.11e^{-5} \tag{A-29}$$

Where *g* is the gravitational acceleration and *β* is the volume coefficient of expansion at the ambient temperature and is given by:

$$\beta = 1/T_{film}\ , \qquad T_{film} = \frac{(T_{actuator} + T_\infty)}{2} \tag{A-30}$$

The dimensionless number for the heat transfer coefficient is given by the Nusselt number Nu_x.

$$Nu_{x=L} = 0.508\Pr^{1/2}(0.952 + \Pr)^{-1/4}Gr_{x=L}^{1/2} = 54.7 \tag{A-31}$$

The heat transfer coefficient at x = L is related to the Nusselt number and the thermal conductivity *k* of the ambient air through the following relation:

$$h_{x=L} = Nu_{x=L}\left(\frac{k}{L}\right) = 54.7\left(\frac{0.02624 W/mC}{0.0143 m}\right) = 100.5 W/m^2C \qquad \textbf{(A-32)}$$

And the average heat transfer coefficient is given by:

$$\bar{h} = 1.333 h_{x=L} = 134 W/m^2C \qquad \textbf{(A-33)}$$

APPENDIX K – ACTUATOR RESISTANCE COMPUTATION

The total resistance is a combination of the resistance of the circular and flat sections of the actuator. The resistance of the circular section R_c is given by:

$$R_c = \mathrm{Re}_{SMA}\left(\frac{L}{A}\right) = 100e^{-8}\Omega m\left(\frac{0.0143m}{4.13e^{-7}m^2}\right) = 0.0346\Omega \qquad \textbf{(A-34)}$$

Where Re_{SMA} is the resistivity of the SMA material given by the manufacturer, L is the total length of the circular sections and A is the cross-section of the actuator.

The resistance of the flat section R_f is a combination of the resistance of the SMA material and the film material. The film material is made of aluminum and is present on one side of the flat section only.

$$\frac{1}{R_f} = \frac{1}{R_{SMA}} + \frac{1}{R_{film}} = \frac{1}{\mathrm{Re}_{SMA}\left(\frac{L_f}{A}\right)} + \frac{1}{\mathrm{Re}_{Al}\left(\frac{L_f}{A}\right)} \qquad \textbf{(A-35)}$$

The total length of the flat section is equal to 38.9mm and the resistivity of aluminum is equal to $2.65e^{-8}\Omega$m. The resistance of the flat sections is computed as 0.0104Ω. The total resistance is the combination of the flat and circular resistances and is equal to 0.0450Ω.

APPENDIX L – DISCONTINUOUS HEATING CURRENT

The derivation of the discontinuous heating current is based on the work done by R. Mukherjee [33]. During the heating cycle, the temperature of the actuator behaves according to (6-1). The temperature as a function of time is obtained by integrating this relation.

$$(T - T_\infty) = \frac{i^2 R}{hA} + C_1 \exp(-\Lambda t/\tau), \quad \Lambda \propto \frac{hA\tau}{mc_P}, \; 0 \le t \le \tau \qquad \textbf{(A-36)}$$

By applying the two boundary conditions: $T = T_2$ at $t = 0$ and $T = T_1$ at $t = \tau$ the constant of integration C_1 can be defined.

$$\begin{gathered} C_1 = (T_2 - T_1)[1 - \exp(-\Lambda)]^{-1} \\ (T_1 - T_\infty) = (T_2 - T_\infty)\exp(-\Lambda) + \frac{i^2 R}{hA}[1 - \exp(-\Lambda)] \end{gathered} \qquad \textbf{(A-37)}$$

During the cooling cycle, the temperature of the actuator is governed by the following equation:

$$mc_P\left(\frac{dT}{dt}\right) = -hA(T - T_\infty) \qquad \textbf{(A-38)}$$

The temperature as a function of time during the cooling cycle is again obtained through integration. Integrating (A-38) gives:

$$(T - T_\infty) = C_2 \exp(-\Lambda t/\tau), \qquad 0 \le t \le (n-1)\tau \qquad \textbf{(A-39)}$$

The boundary conditions at this stage are: $T = T_1$ at $t = 0$, and $T = T_2$ at $t = (n\text{-}1)\tau$. The constant of integration C_2 is then defined as:

$$\begin{gathered} C_2 = (T_1 - T_2)\{1 - \exp[-\Lambda(n-1)]\}^{-1} \\ (T_2 - T_\infty) = (T_1 - T_\infty)\exp[-\Lambda(n-1)] \end{gathered} \qquad \textbf{(A-40)}$$

Substituting (A-40) into (A-37) results in (6-3) found in section 6.1.2.

APPENDIX M – ELECTRICAL WIRE RESISTANCE APPROXIMATION

The conduit wire within the manipulator is coiled around the actuator structure such the wire is located between the actuators and the outer shell. This arrangement facilitates the construction of the prototype and limits the influence of the wire on the mechanical properties of the manipulator. The approximate size of the loops is shown in the figure below.

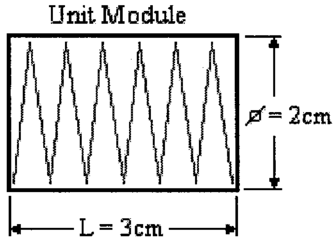

Figure A-15: Lead and ground wire arrangement

In one unit module, a conduit wire will do six loops. With the configuration above, the approximate length of one wire through one unit module is equal to 38cm. To limit the amount of wiring, the positive and ground terminals are arranged as follows.

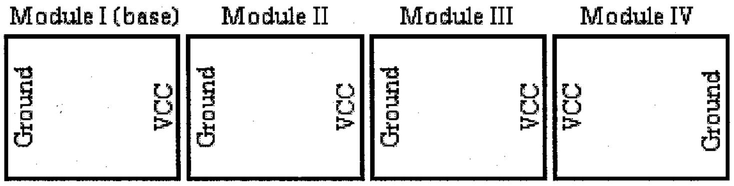

Figure A-16: Ground and VCC arrangement

During the construction of the prototype it is assumed that an extra centimeter of wiring will be required to complete the connections at the terminals (one at ground and one at VCC) and an extra five centimeters from the base to the exterior of the manipulator. To reduce the stiffness of the manipulator, the conduit wire with the smallest diameter is chosen based on the maximum fusing current. A copper magnet wire with a gauge of 28AWG and a resistivity of $2.73e^{-3}\Omega$/cm could sustain the 14Amp pulse current and has an equivalent resistance per unit length to the flat sections of the actuator. The following table lists the lengths of wiring required for each section and the total resistance of the conduit wire for each set of three actuators.

Module	**VCC**	**VCC wire length [cm]**	**Ground**	**Ground wire length [cm]**	**Extra wiring [cm]**	**Total wire length [cm]**	**Resistance [Ω]**
I	1	38	0	0	7	45	0.12
II	2	76	1	38	7	121	0.33
III	3	114	2	76	7	197	0.54
IV	3	114	4	152	7	273	0.75

Table A-1: Total resistance of each unit module

APPENDIX N – L298 VOLTAGE DROP APPROXIMATION

The L298 dual full bridge driver exhibits a saturation voltage across its input output terminals. This saturation voltage lowers the projected output current and needs to be taken into account to properly select the current limiting resistor. Figure A-17 shows the current output of one channel for different driver configuration using a source voltage of $V_S = 12.15V$.

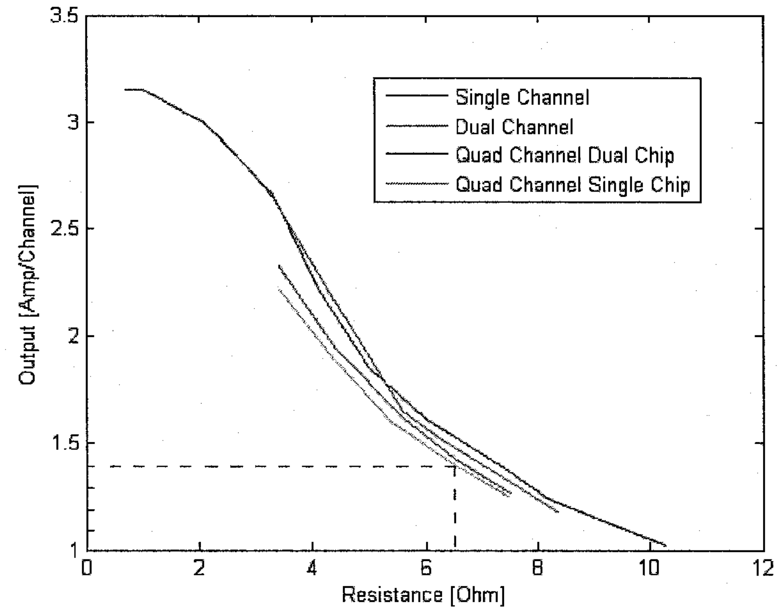

Figure A-17: Output current of one channel for different driver configurations

From this figure the voltage drop can be determined from the following equation:

$$V_s - V_{sat} = R \times i_{out} \tag{A-41}$$

For simplicity, the single chip quad channel configuration is used in the prototype construction. For a total output current of approximately 14Amps, the current output per channel is under 1.2Amps. Using (A-42) and the results above the saturation voltage is approximately equal to 4.25Volts. The unusually high saturation voltage is due to the low source voltage and high operating currents.

APPENDIX O – CURRENT LIMITER RESISTANCE

The block diagram for one actuator circuit is shown below. The current limiter resistors are located at the ground drivers since each unit module has a different wire resistance.

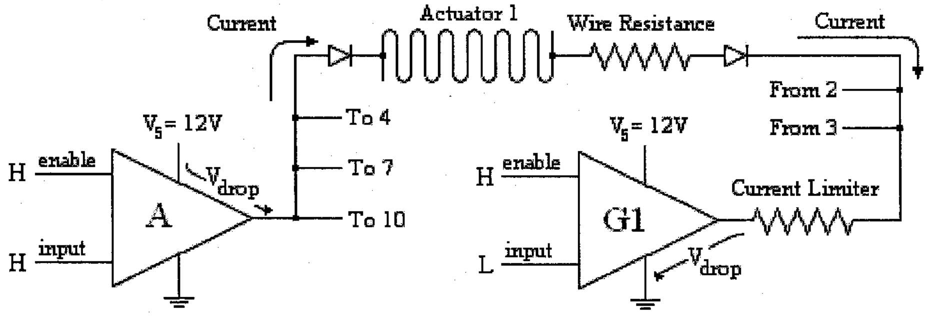

Figure A-18: Complete circuit block diagram for one actuator

Using the resistance values for the actuator and the conduit wire as well as the saturation voltage on both L298 bridge drivers, the required resistance of the current limiter can be obtained from the following equation:

$$V_s - 2V_{sat} = \left(R_{actuator} + R_{wire} + R_{\lim itor}\right) \times i_{out} \tag{A-42}$$

The source voltage is equal to 12.15Volts, the saturation voltage is equal to 4.25Volts, the actuator resistance is given a 0.045Ω and the expected output current per channel is 1.2Amps. The estimated conduit wire resistances computed in Appendix M. The current limiter resistance is calculated for each unit module and the results are given in Table A-2.

Table A-2: Current limiter theoretical resistance

Module	Calculated current limiter resistance [Ω]
I	2.88
II	2.67
III	2.46
IV	2.25

As a comparison, the experimental current output of the complete circuit of Figure A-18 using four channels (one L298 chip) per VCC and per ground driver is given for different resistance values (the actual total resistance is equal to 2.96Ω).

Table A-3: Experimental output current of parallel drivers

Experimental test module	**Current limiter resistance [Ω]**	**Load resistance (wires and actuator) [Ω]**	**Experimental output current [Amp]**	**Current per channel [Amp]**
IV	2.3	1.2	4.83-4.90	≈1.22

APPENDIX P – ACTUATOR TENSILE TEST RESULTS

P.1 R=0.36mm, l_l=3mm, L_o=13.2mm, W=5.9mm, Heat-treated at 600°C

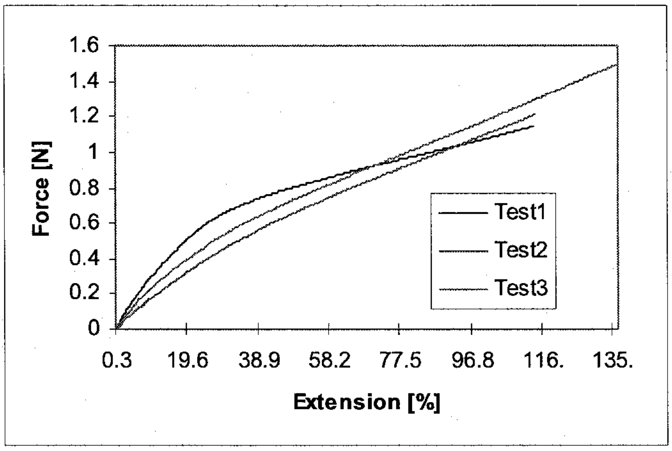

Figure A-19: Martensite response

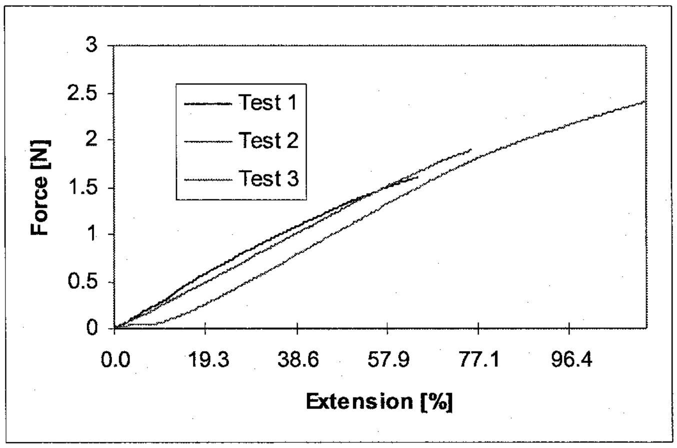

Figure A-20: Austenite response

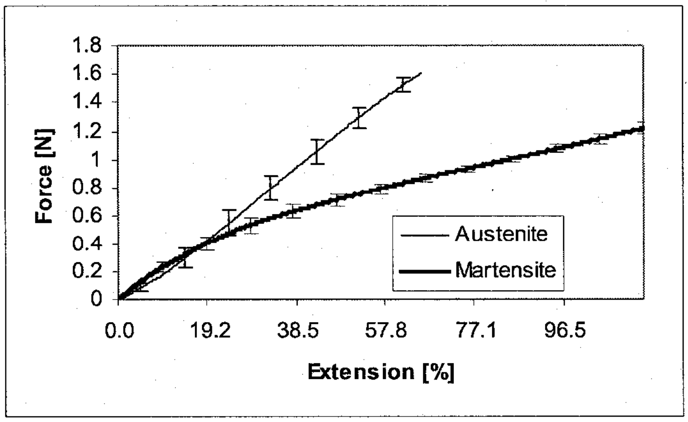

Figure A-21: Average data [R = 0.36mm, l_l = 3mm, W = 5.9mm, 600°C]

P.2 R=0.36mm, l_l=3mm, L_o=12mm, W=5.9mm, Heat-treated at 500°C

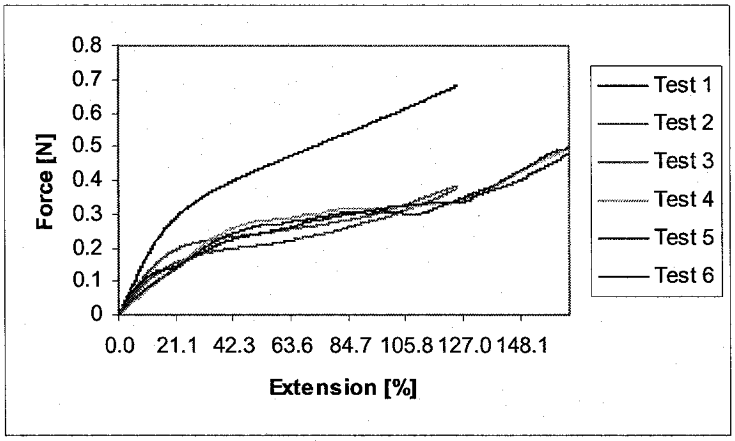

Figure A-22: Martensite response

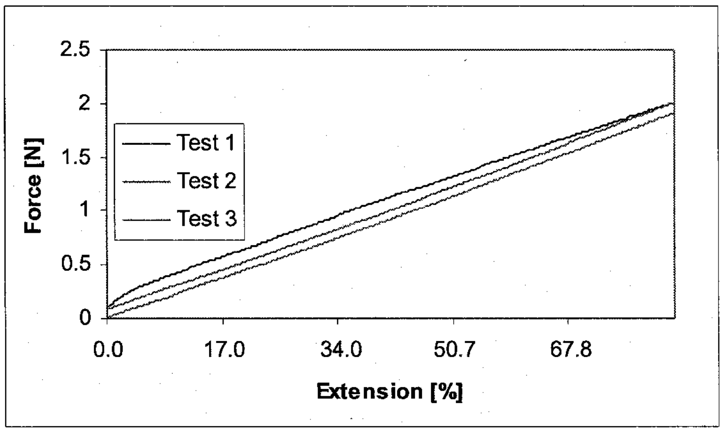

Figure A-23: Austenite response

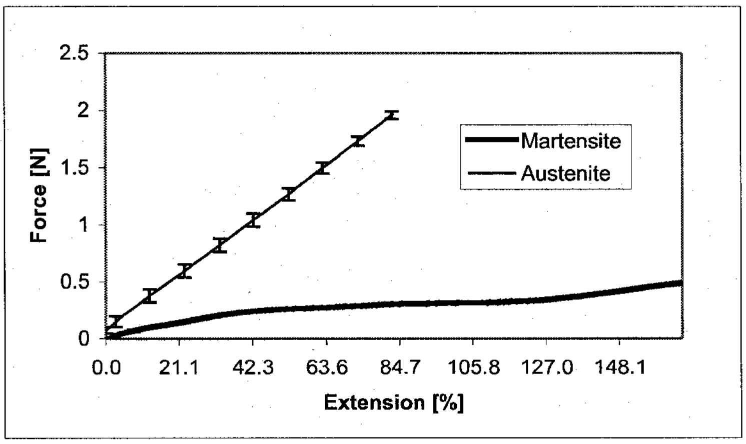

Figure A-24: Average data [R = 0.36mm, l_l = 3mm, W = 5.9mm, 500°C]

P.3 R=0.36mm, l_l=3mm, L_o=12mm, W=7.0mm, Heat-treated at 500°C

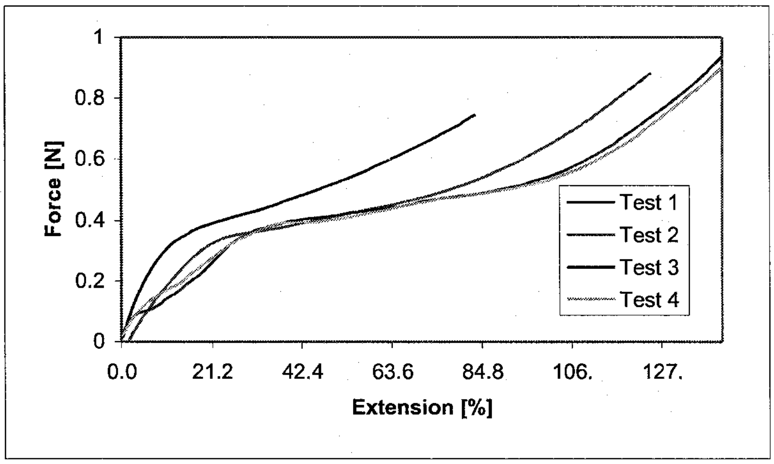

Figure A-25: Martensite response

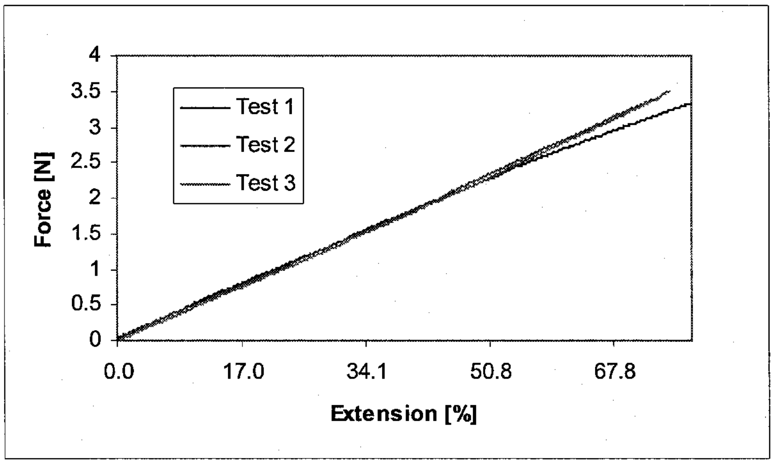

Figure A-26: Austenite response

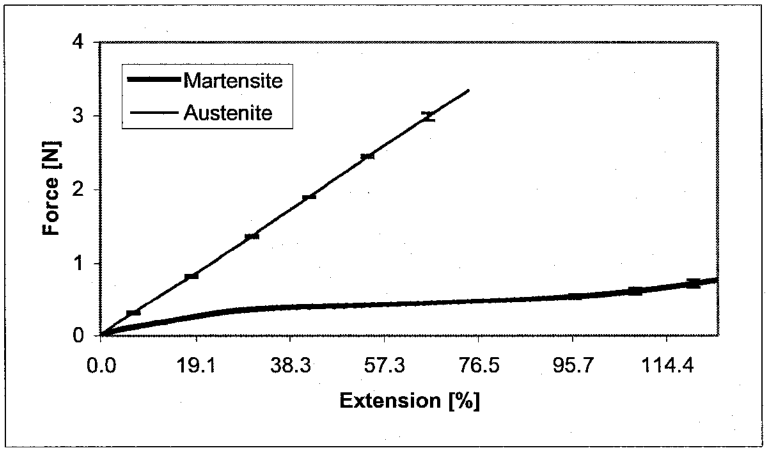

Figure A-27: Average data [R = 0.36mm, l_l = 3mm, W = 7.0mm, 500°C]

P.4 R=0.36mm, l_l=3mm, L_o=12mm, W=7.0mm, Heat-treated at 500°C, Bare

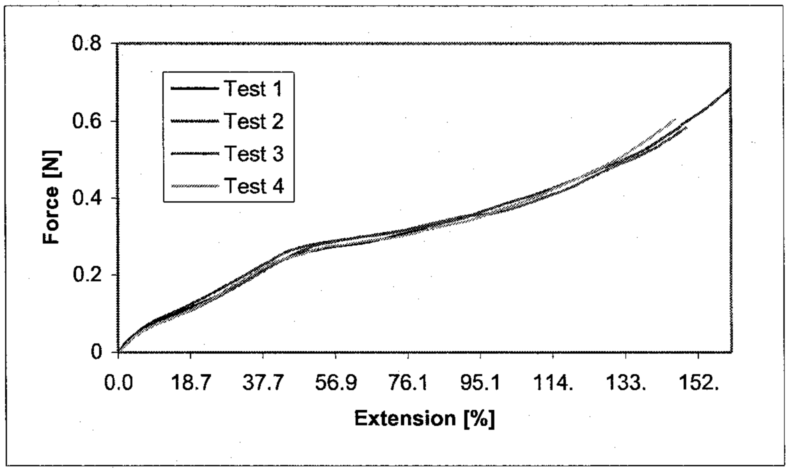

Figure A-28: Martensite response

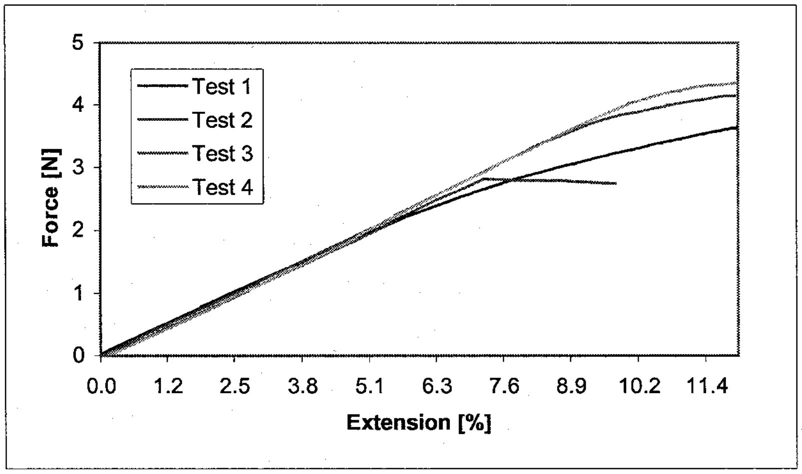

Figure A-29: Austenite response

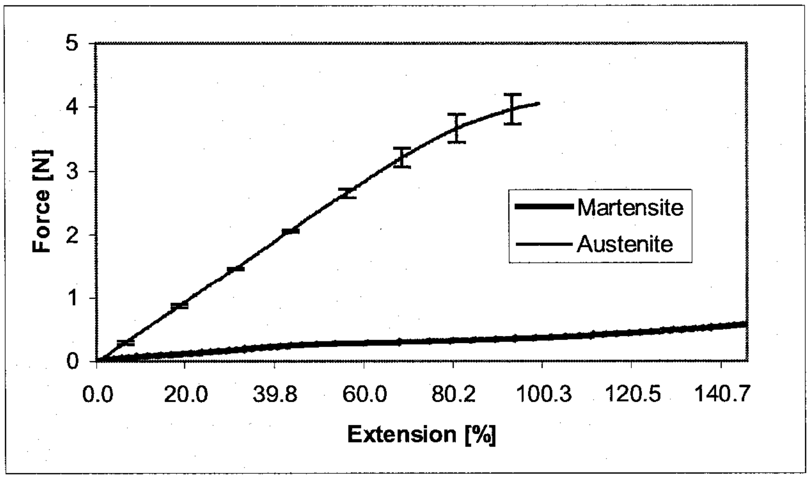

Figure A-30: Average data [R = 0.36mm, l_l = 3mm, W = 7.0mm, 500°C, Bare]

P.5 R=0.46mm, l_l=3mm, L_o=16.8mm, W=5.9mm, Heat-treated at 600°C

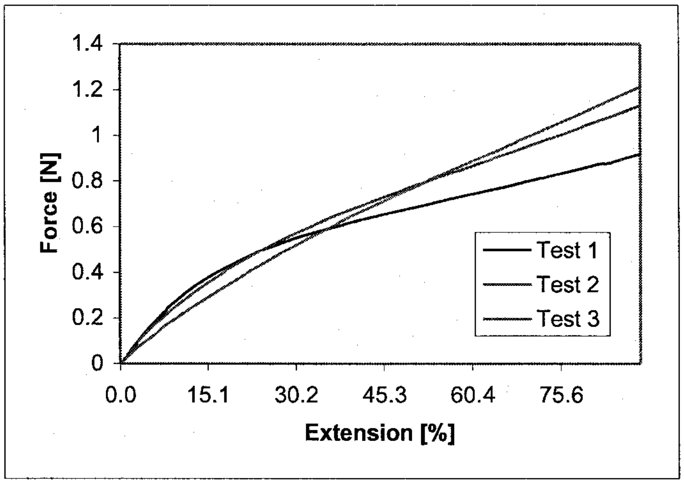

Figure A-31: Martensite response

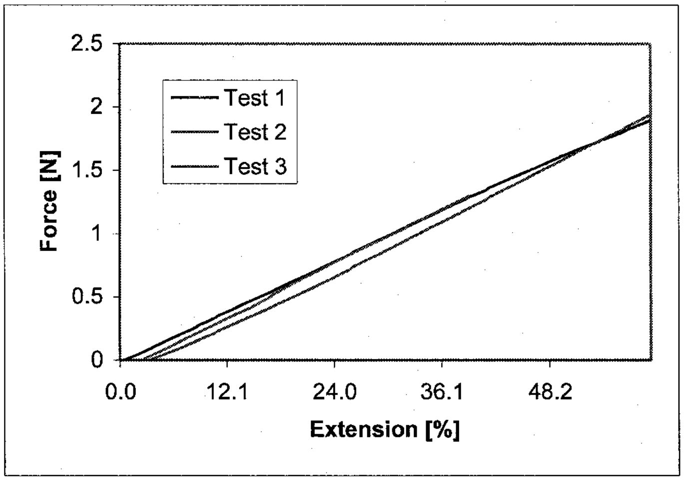

Figure A-32: Austenite response

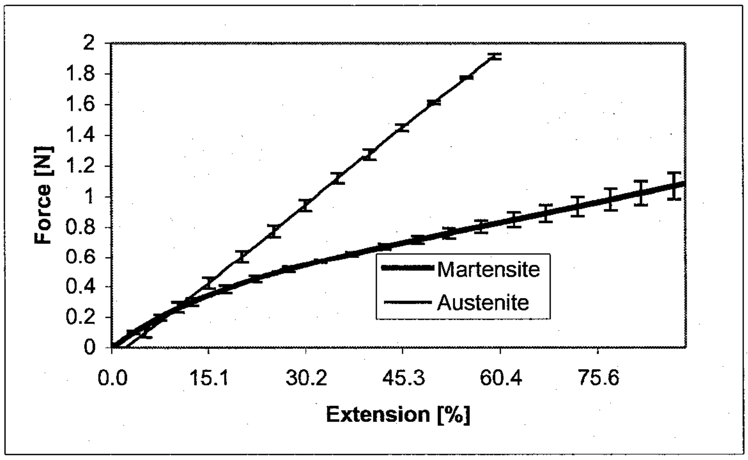

Figure A-33: Average data [R = 0.46mm, l_l = 3mm, W = 5.9mm, 600°C]

P.6 R=0.46mm, l_l=3mm, L_o=13.5mm, W=5.9mm, Heat-treated at 500°C

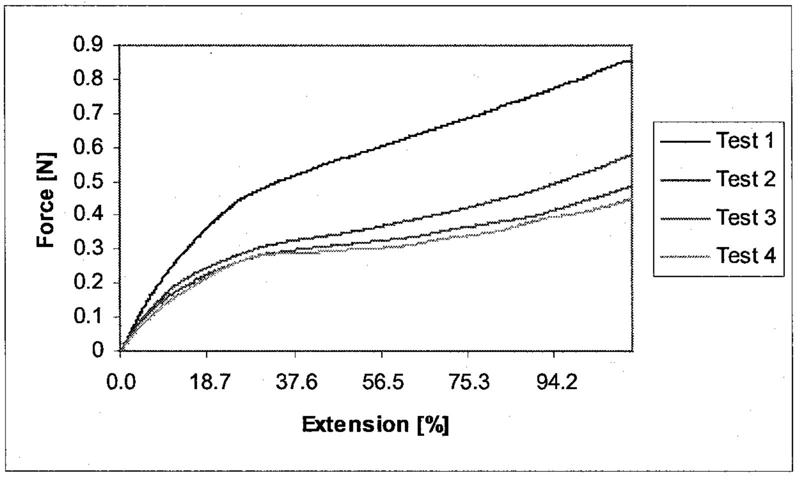

Figure A-34: Martensite response

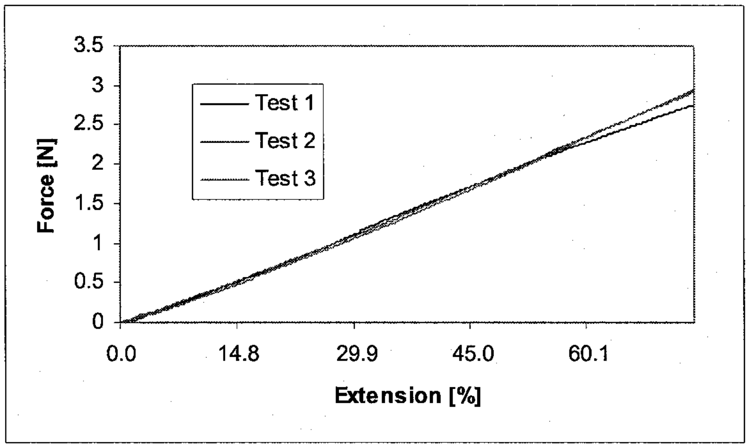

Figure A-35: Austenite response

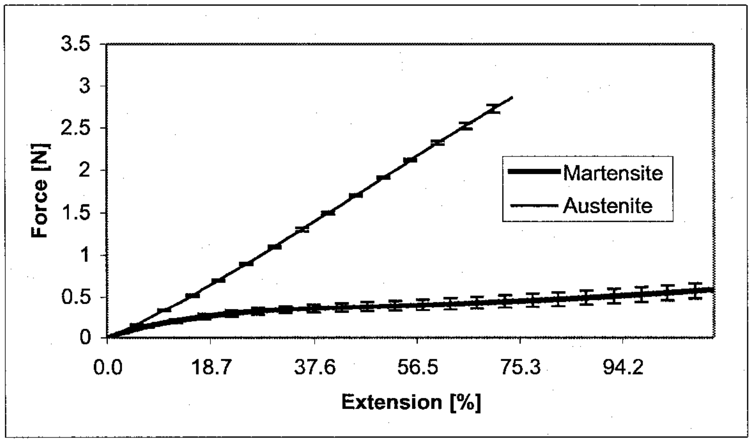

Figure A-36: Average data [R = 0.46mm, l_l = 3mm, W = 5.9mm, 500°C]

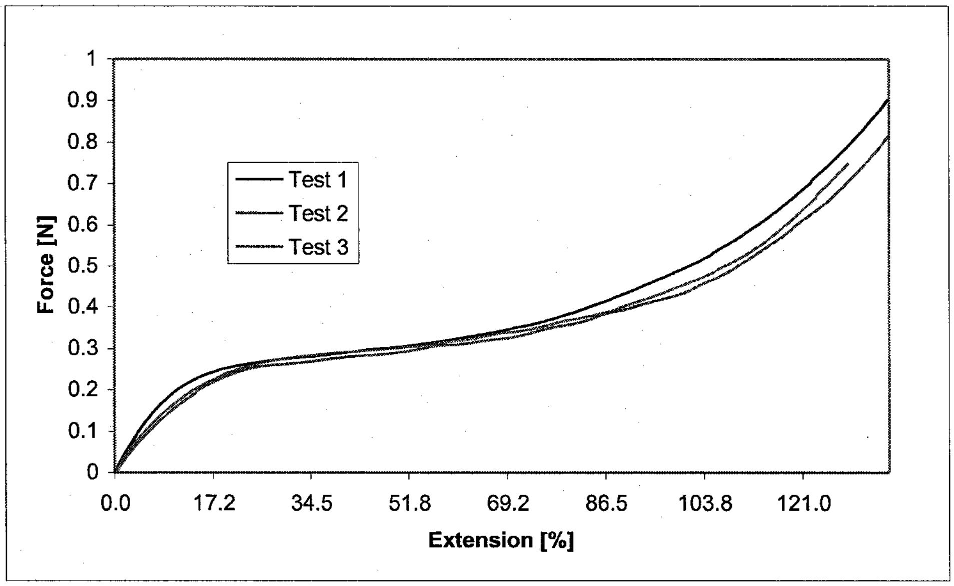

Figure A-37: Martensite response Test #2

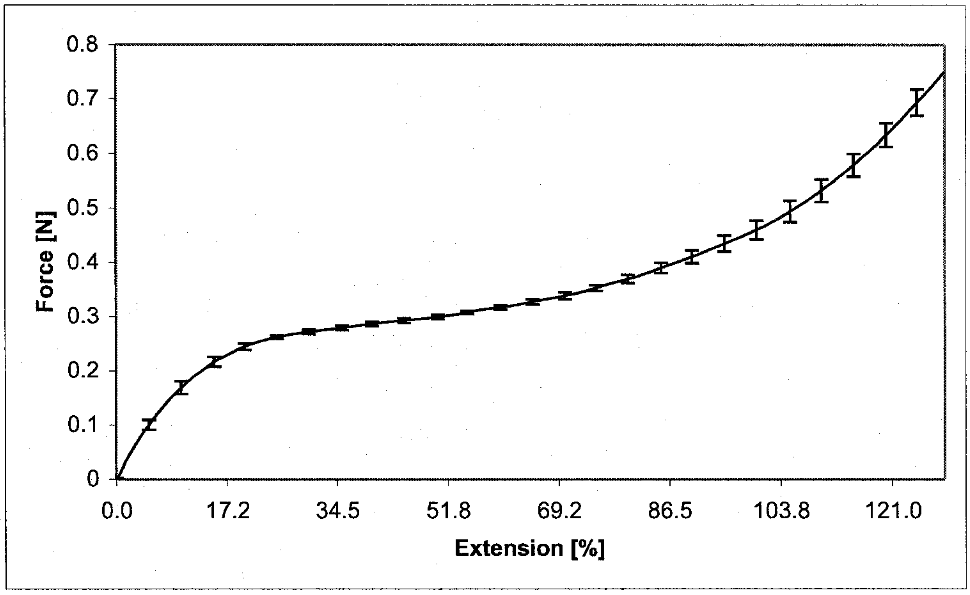

Figure A-38: Average Martensite response Test #2

P.7 R=0.46mm, l_l=3mm, L_o=24mm, W = 5.9mm, Heat-treated at 400°C

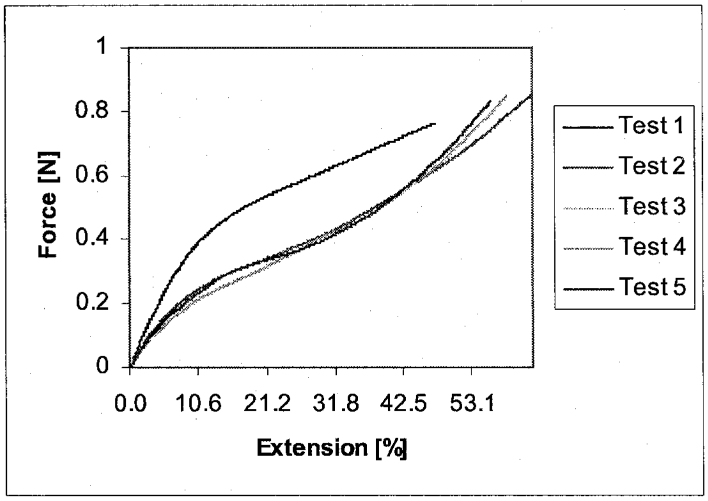

Figure A-39: Martensite response

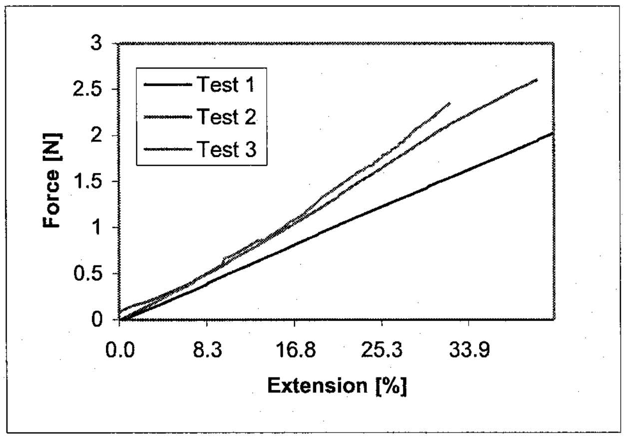

Figure A-40: Austenite response

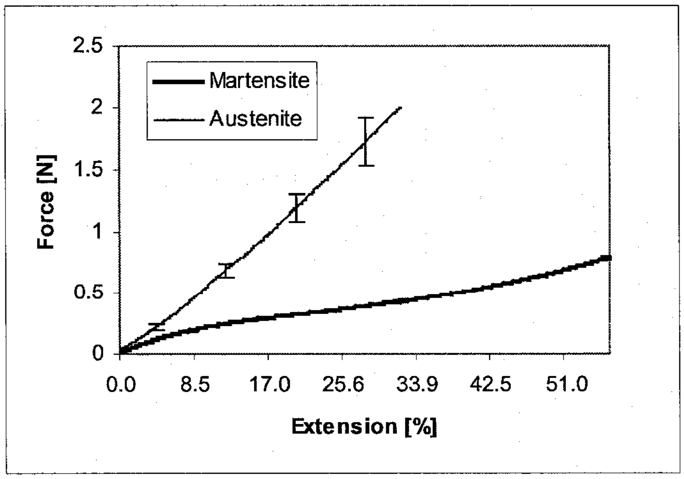

Figure A-41: Average data [R = 0.46mm, l_l = 3mm, W = 5.9mm, 400°C]

P.8 R=0.46mm, l_l=4mm, L_o=14mm, W=5.9mm, Heat-treated at 600°C

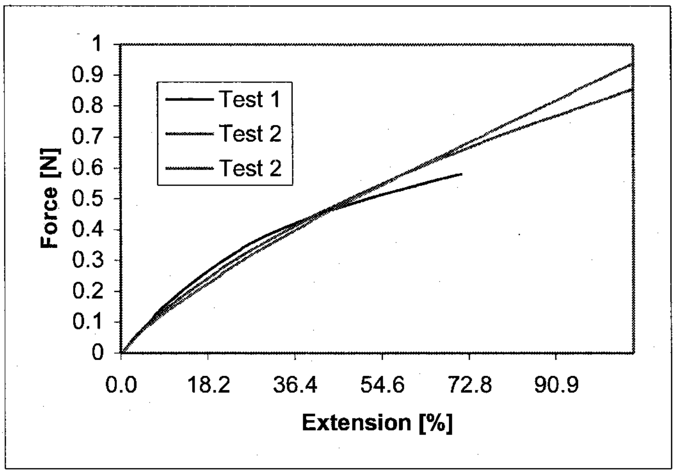

Figure A-42: Martensite response

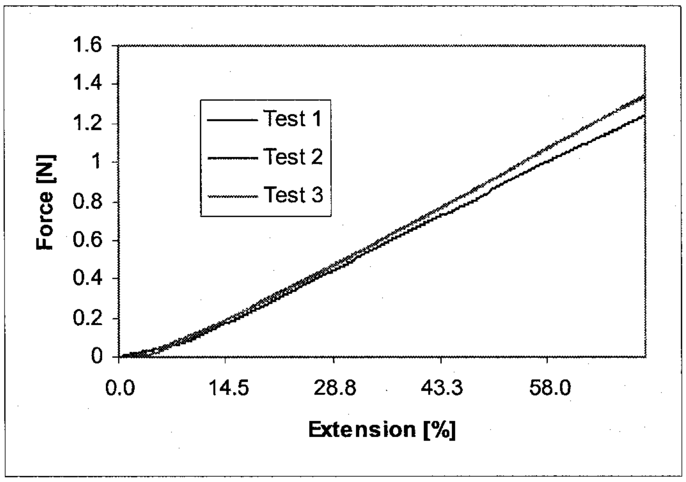

Figure A-43: Austenite response

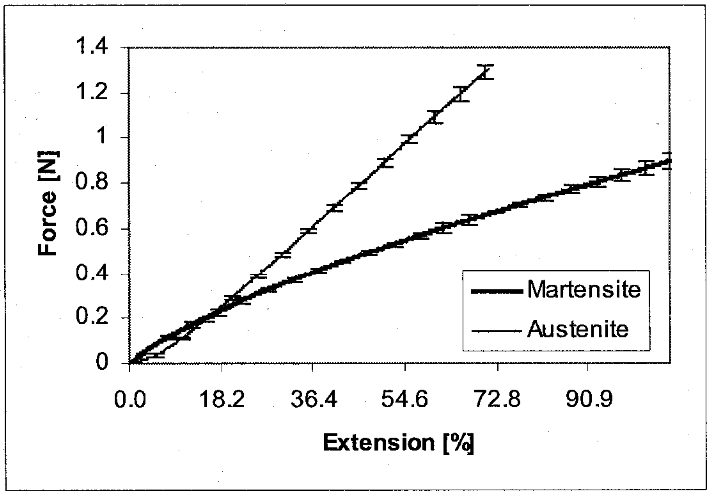

Figure A-44: Average data [R = 0.46mm, l_l = 4mm, W = 5.9mm, 600°C]

P.9 R=0.72 mm, l_l=3mm, L_o=17mm, W=5.9mm, Heat-treated at 600°C

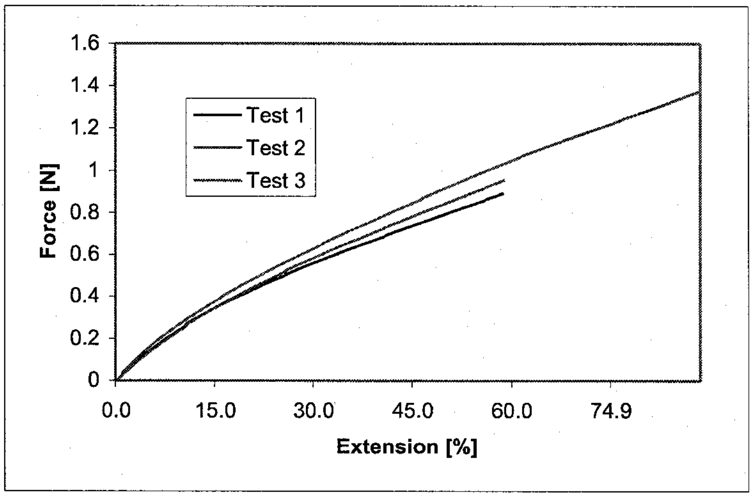

Figure A-45: Martensite response

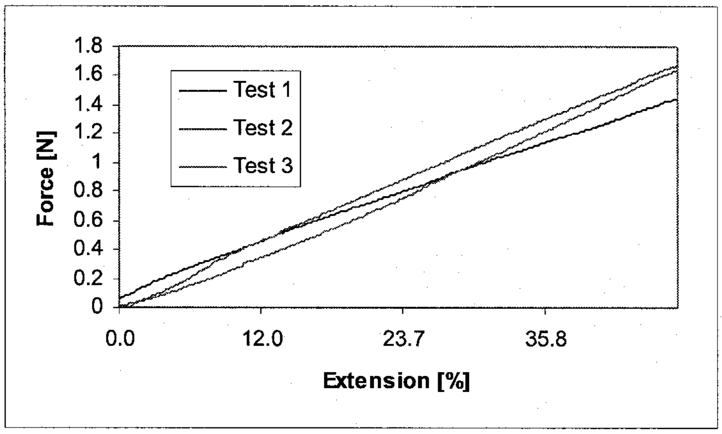

Figure A-46: Austenite response

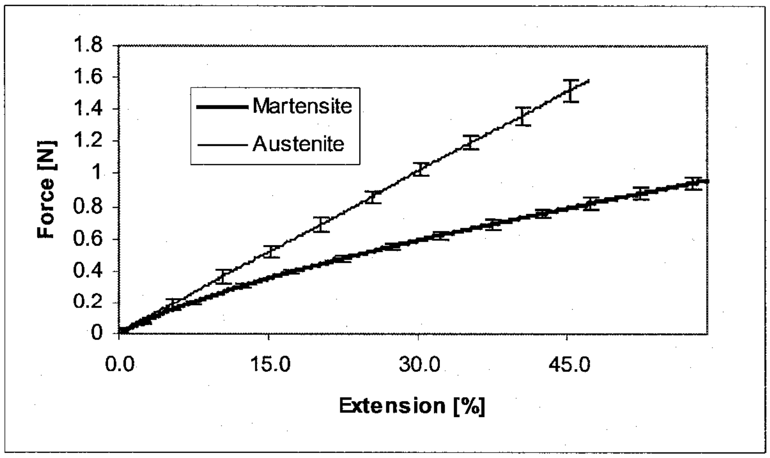

Figure A-47: Average data [R = 0.72 mm, l_l = 3mm, W = 5.9mm, 600°C]

P.10 R=0.72 mm, l_l=3mm, L_o=16.5mm, W=5.9mm, Heat-treated at 500°C

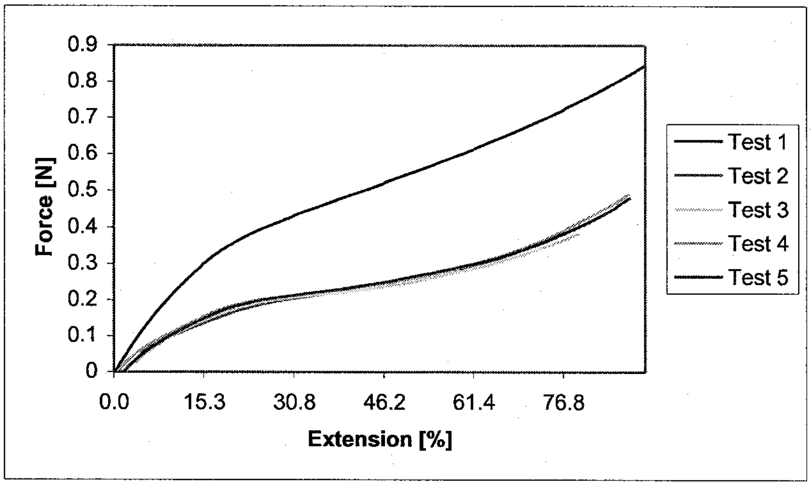

Figure A-48: Martensite response

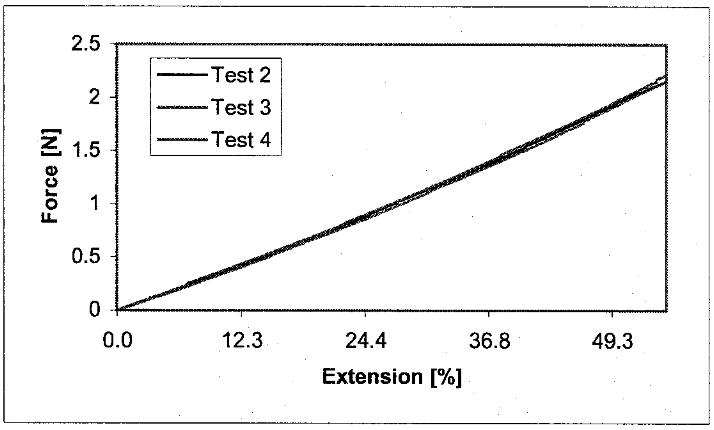

Figure A-49: Austenite response

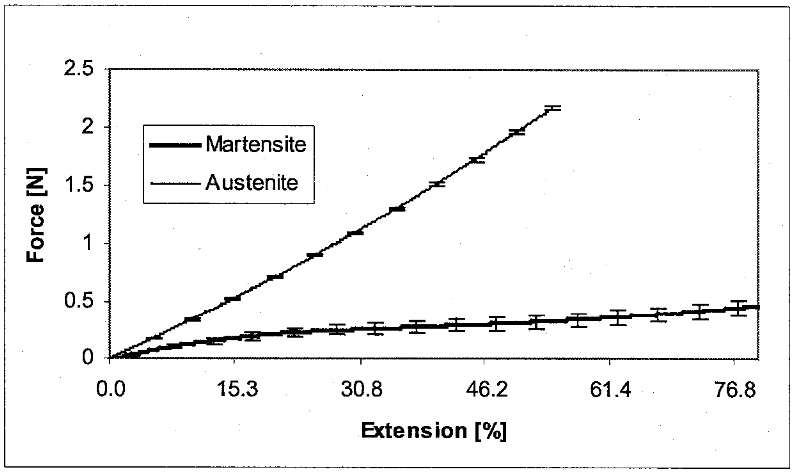

Figure A-50: Average data [R = 0.72 mm, l_l = 3mm, W = 5.9mm, 500°C]

APPENDIX Q – SMA MATERIAL TENSILE TEST RESULTS

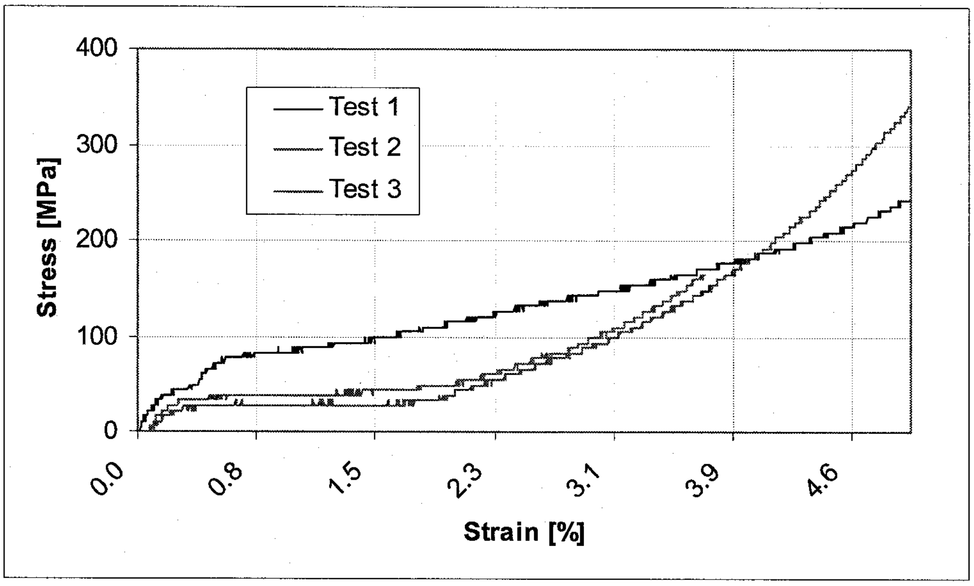

Figure A-51: SMA strip martensite response

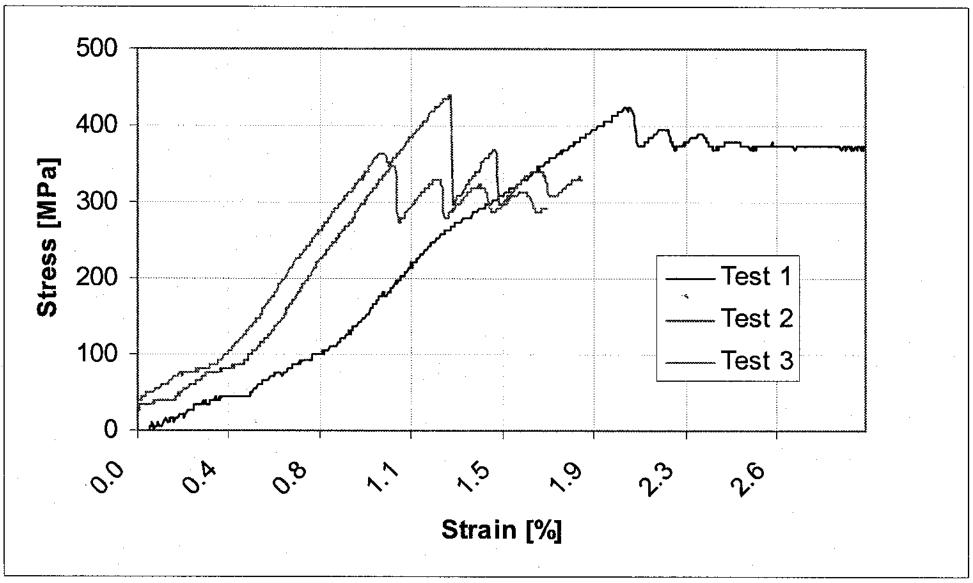

Figure A-52: SMA strip austenite response